Spring 2011

A Three Dimensional Green's Function Solution Technique for the Transport of Heavy Ions in Laboratory and Space

Candice Rockell Gerstner
Old Dominion University

A THREE DIMENSIONAL GREEN'S FUNCTION SOLUTION TECHNIQUE FOR THE TRANSPORT OF HEAVY IONS IN LABORATORY AND SPACE

by

Candice Rockell Gerstner
B.S. May 2006, St. John Fisher College
M.S. December 2008, Old Dominion University

A Dissertation Submitted to the Faculty of
Old Dominion University in Partial Fulfillment of the
Requirements for the Degree of

DOCTOR OF PHILOSOPHY

COMPUTATIONAL AND APPLIED MATHEMATICS

OLD DOMINION UNIVERSITY
May 2011

Approved by:

John Tweed (Director)

Gordon Melrose (Member)

John Adam (Member)

Francis Badavi (Member)

Steve Blattnig (Member)

ABSTRACT

A THREE DIMENSIONAL GREEN'S FUNCTION SOLUTION TECHNIQUE FOR THE TRANSPORT OF HEAVY IONS IN LABORATORY AND SPACE

Candice Rockell Gerstner
Old Dominion University, 2011
Director: Dr. John Tweed

In the future, astronauts will be sent into space for longer durations of time compared to previous missions. The increased risk of exposure to ionizing radiation, such as Galactic Cosmic Rays and Solar Particle Events, is of great concern. Consequently, steps must be taken to ensure astronaut safety by providing adequate shielding. The shielding and exposure of space travelers is controlled by the transport properties of the radiation through the spacecraft, its onboard systems and the bodies of the individuals themselves. Meeting the challenge of future space programs will therefore require accurate and efficient methods for performing radiation transport calculations to analyze and predict shielding requirements. One such method, which is developed in this dissertation, is based on a three dimensional Green's function solution technique for the transport of heavy ions in both laboratory and space.

ACKNOWLEDGMENTS

I would like to thank Dr. Tweed for giving me the opportunity to work on this project and for spending so much time with me in order to help me understand the mathematics and physics behind this problem. Additionally, I would like to thank Dr. Francis Badavi for his support while I was writing my dissertation and as I was preparing for graduation. I would also like to thank the NASA Graduate Student Researchers Program (NASA NNX09AJ06H), and the Virginia Space Grant Consortium for the financial support of my research endeavors. My family has been extremely supportive in my goals and I would like to thank each and every one of my family and extended family members for helping me live out my dream. My professors at St. John Fisher College have also been a great influence on me and have taught me the background that I needed to accomplish what I have thus far. Last but not least, I would like to thank my husband, Ray, for being patient with me.

NOMENCLATURE

MeV	Megaelectron volt
GeV	Gigaelectron volt
SPE	Solar Particle Event
GCR	Galactic Cosmic Ray
A_j	Atomic mass of a type j ion, amu
E	Ion kinetic energy, MeV/amu
$H(x)$	Heaviside function
$\mathbf{n}(\mathbf{x}')$	Outward directed unit normal at $\mathbf{x}'$ on the boundary ∂V
$P_j(E)$	Total survival probability
$R_j(E)$	Continuous slowing down range of a type j ion of energy E
$\tilde{S}_j(E)$	Stopping power per atomic mass unit, MeV/(cm-amu)
ρ	Projection of $\mathbf{x}$ onto $\mathbf{\Omega}$, cm
$\sigma_j(E)$	Macroscopic absorption cross section
$\sigma_{jk}(\mathbf{\Omega}, \mathbf{\Omega}', E, E')$	Double differential production cross section, (cm-sr-MeV/amu)$^{-1}$
$\sigma_{jk}(E)$	Total cross section, cm^{-1}
$f_E(E, E')$	Energy Distribution, (MeV/amu)$^{-1}$
$f_{\mathbf{\Omega}}(\mathbf{\Omega}, \mathbf{\Omega}', E')$	Angular Distribution, sr^{-1}
$\phi_k(\mathbf{x}, \mathbf{\Omega}', E')$	Flux of type k ions
m_p	Rest mass of a proton
$\gamma_{_L}$	Fragment Lorentz factor
$\beta_{_L}$	Fragment beta factor
γ_k	Projectile Lorentz factor
β_k	Projectile beta factor
$\sigma_{\parallel}$	Fragment momentum width
E_s	Energy downshift
$\mathbf{\Phi}$	Flux column vector
$\mathbf{\Omega}$	Direction of propagation
$\mathbf{Q}$	Quadrature operator
$\mathbf{L}$	Linear Transport operator
$\mathbf{\Xi}$	Fragmentation or collision operator

TABLE OF CONTENTS

LIST OF TABLES

LIST OF FIGURES

CHAPTER I

INTRODUCTION

I.1 NASA SPACE EXPLORATION

The vast unknowns of deep space have always fascinated the human race. Ever since humans began to document their daily activities, drawings detailing space and the alignment of the planets have been discovered. One specific civilization that was entranced by astronomy and cosmology was that of the Maya. Their calendars and how they conducted their daily lives were based on their observations of the movement of the planets. As time progressed, history continued to reveal that humans continued to wonder about the discoveries that could be made about Earth and our universe through the exploration of space. During the Cold War, this fascination became a reality with the first human space missions. The first of which was conducted by the Soviet Union in 1961 when Yuri Gagarin orbited the Earth. The United States then followed when Alan Shepard conducted the first suborbital flight by an American in 1961. Many more orbital flights followed after this point. The 1960s brought a change of reality regarding the limits of human travel in space. In 1969, as part of the Apollo space mission, Neil Armstrong became the first person to walk on the moon. This was and is the farthest distance that a human has travelled away from Earth, approximately a quarter million miles. In total, there have been twelve men to reach the Moon's surface during the Apollo missions [1].

After the 1960s, the numbers of manned flights to space dropped off dramatically. So far, the longest single manned spaceflight was conducted by Valeriy Polyakov in 1994 in which he spend 803 days, 9 hours, and 39 seconds (approximately 2.2 years) in space. Recently, since President Bush's address to the country regarding sending humans "to the moon and beyond", there has been another push for space exploration.

With this exploration, scientists at NASA are now beginning to look seriously at the health risks to humans that will travel in the upcoming missions, which are proposed to be of a much longer duration than previous missions. In his speech, President Bush considered the idea of setting up a space base on the surface of the

This dissertation follows the style of *Nuclear Instruments and Methods in Physics Research B: Beam Interactions with Materials and Atoms*

moon by 2020 and also sending a crew to Mars. The round-trip duration of the trip to Mars alone would take about three years. Many scientists have been concerned with the health effects of these long term flights. According to one article, scientists have "...identified 55 threats, from radiation-induced cancers to depression" [2]. The threat that is the topic of discussion in this dissertation is that of ionizing radiation-induced cancer. NASA is currently running experiments and setting up models to predict the amount of radiation exposure to the astronauts using a variety of different materials for shielding purposes. "The effectiveness of shielding is extremely sensitive to an understanding of the biological mechanisms by which radiation affects human health and performance" [3]. I will first discuss the types of radiation that these space travelers will be exposed to, and then I will outline the history of the transport codes that emerged in order to model the transport of this radiation through materials.

I.2 COSMIC RAYS

Data from satellites have enabled scientists to categorize the types of radiation that will be encountered in space. The collection of penetrating particles from space are defined as cosmic rays. There are three main categories of cosmic rays that are of concern for human exposure. The three are galactic cosmic rays (GCR), solar particle events (SPE), and the radiation inside Earth's geomagnetic radiation belts. A majority of space radiation consists of energetic electrons, protons, and alpha particles. Within the Earth's radiation belts, protons are the most abundant in the low altitudes and electrons in the higher altitudes. Therefore, the electrons are subjected to variations induced by the space weather changes (solar plasma). A more detailed discussion of the exact composition will follow.

Cosmic rays have been studied for more than a century now. One of the first people to come up with a theory related to cosmic rays was Major General Edward Sabine in 1852 when he hypothesized a connection between magnetic storms and sunspots [4]. Later on, in 1903, S.P. Thompson suggested that charged particles originating on the Sun arrive to the Earth as highly penetrating radiation. Following this, the first experimental observation about these theories came in 1912 when Victor Hess conducted a balloon experiment to discover that the electroscope discharged faster the higher the balloon went in the atmosphere [4]. Specifically, he found that the electric presence was four times greater at 16,000 feet than at sea level. Upon conducting this experiment, Hess explained his results by claiming that this was

evidence that "a radiation of very high penetrating power enters the atmosphere from above" [4]. His experiment led many other people to explore the intensity of the radiation and to develop conjectures on where it was coming from. However, measurements at high altitudes could not be obtained in those early years, so Robert Millikan proposed an interesting idea as an alternative to measure the ionization that takes place in the atmosphere. In 1928, he hypothesized that cosmic rays were created during the synthesis of heavy elements from hydrogen. He was able to improve the detection technology and began to take measurements of the ionization with instruments that were lowered in mountain lakes at different depths. He wanted to reveal the origin of cosmic rays by looking at the energy of the rays. It was hypothesized that since the total thickness of the atmosphere corresponds to only about ten meters of water, that his measurements in water would determine the absorption length of the cosmic radiation [4]. However, it turns out that cosmic rays have different absorption lengths in the atmosphere than in water.

At this point, classical electrodynamics and electromagnetic cascade theory were gaining the interest and attention of the physics community. In 1929, Dimitry Skobelzyn discovered cosmic ray induced showers by using cloud chambers. He observed that an incoming particle ionized the material in the chamber and made the particle track visible. This led to the discovery of many new subatomic particles. Also, in the same year, American rocket pioneer, Robert Goddard installed instruments for detecting space radiation in rockets. These two individuals, among others, began a great era of charged particle detection.

The next detection instrument was the Geiger-Müller (G-M) counter, which gave a pulse after a charged particle would pass through it. These counters led to the implication that cosmic rays were composed of energetic, charged particles. This observation was made by Werner Kolhrster and Walther Bothe in 1930 when they used two G-M counters with a gold brick that was 4.1 cm thick and only found a 24 percent decrease in the particles that were entering versus those that were leaving [4, 5].

During the 1950s and 1960s, the design of particle accelerators and detectors improved greatly. In fact, in 1958, the United States launched their first satellite. Inside this satellite, the Explorer 1, was a G-M tube. The data that was obtained from this satellite allowed James Van Allen to conclude that the Earth was surrounded by intense belts of trapped radiation [4, 5].

The improvements in detectors and accelerators were followed by the development of models of the cosmic rays acceleration mechanism. A combination of all the results up to this led to the creation of the *standard model of cosmic rays* [5].

I.3 COMPOSITION OF COSMIC RAYS

Cosmic rays are composed of 85 percent protons, 13 percent alpha particles, and about 2 percent of electrons and nuclei of lithium, boron, carbon, oxygen, all the way up to tin [6]. The most abundant particles, such as H, He, C, O, and Fe are known as primary (naturally abundant) particles. Primary cosmic rays are particles that are accelerated (generated) at astrophysical sources [6]. Other particles such as Li, Be, B, and Sc are known as secondary particles and are less abundant [5]. Secondary particles are produced in the interaction of the primary particles with interstellar gas [6].

Collectively these charged particles are called galactic cosmic rays (GCR). GCR is always present in interstellar space, and the intensity of the GCR is modulated by the solar cycle, during which the Sun's magnetic field varies approximately every eleven years. This type of radiation originates from unknown parts of the galaxy and contains energetic charged particles ranging from hydrogen to tin. These particles can penetrate many of the materials that are now being used to make a spacecraft. They produce fragments that can penetrate even deeper into most materials, and could pose a threat to the health and safety of astronauts. This fact makes shielding against GCR a challenging problem.

SPEs consist of high-intensity ionizing radiation from the Sun, which also varies with the solar cycle. They occur most frequently during periods of intense sunspot activity. They consist of mainly energetic protons and to a lesser degree alpha particles. In most cases, SPEs are short lived, but are temporally unpredictable. Therefore, the problem that SPEs pose is not only the penetration of the types of shielding used to construct the spacecrafts or the thickness of these shields, but knowing when an SPE will occur so that astronauts can ensure that they will be inside the spacecraft at the time of occurrence.

The particles that are radiated by the Sun travel through the solar wind (as depicted by figure 1, courtesy of [7]) and reach close to Earth with velocities of 300 to 1000 km/s. The corresponding flux of these particles is approximately 1.2×10^8 $cm^{-2}s^{-1}$. SPE that arrive at the Earth are made up of 98 percent protons

with energies between 1-100 MeV, but for an energetic SPE these particles can have energies of approximately 1 GeV or greater. These particles are blocked from entering the Earth by the ionosphere and subsequent layers of the atmosphere.

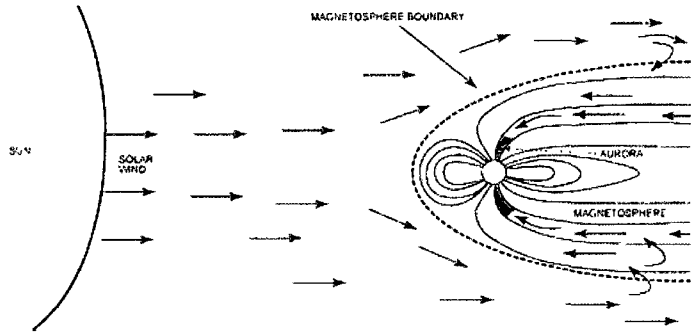

FIGURE 1: Interplanetary Magnetic Field

Solar particles can originate from two processes: a solar flare site on the Sun becoming energized or by shock waves associated with Coronal Mass Ejections (ejection of material from the solar corona). The latter only accounts for about one percent of strong solar particles. However, these are the ones that are of primary interest due to the release of massive quantities of matter (mostly protons) above the Sun's surface, with proton energies often up to 1 GeV, following a broad spectral distribution of proton ejection density in the range of 10^6 to 10^{12} particles/(MeV-cm^2-event). There are also two accelerating mechanisms for these particles. These are diffuse shock acceleration (Fermi acceleration) and shock-drift mechanism, in which particles gain energy by drifting in the induced field along the shock surface. These accelerated particles can penetrate the Earth's magnetic field. In fact, due to extreme energies of strong solar flare events, protons can penetrate through the Earth's magnetosphere and upper atmosphere layer, the ionosphere. These energetic protons are guided to where the magnetic field lines enter and exit where they collide with the atmosphere and release energy through ionization. These types of events can cause disruption to electrical grids, radio communications, and can cause an increase in the neutron count on ground level neutron detectors.

On the subject of cosmic rays, it is worth noting that particles that are created and accelerated in deep space by supernovas may eventually reach the solar system. On the way, the cosmic ray protons will be scattered in the magnetic fields that they

cross and will slowly diffuse. Protons will produce gamma rays through the decay of neutral pions generated in inelastic interactions of cosmic rays with interstellar matter. Gamma rays are also produced by electrons in bremsstrahlung (stopping radiation), in which charged particles interact with the electromagnetic field of the atomic nuclei and generate photons. The electrons will also interact with the magnetic fields, the rest of the radiation fields, and matter.

One model that demonstrates the particle diffusion in the galaxy is called the leaky box approximation. This approximation assumes that the galaxy is uniformly filled with energetic particles that have been trapped for a long time and the particles that escape from the galaxy are classified by how much they leak or diffuse out of the 'box'. Through this diffusion, is it assumed that the particles interact with galactic matter and radiation fields to produce gamma rays [5].

Once inside the solar system, the particles will be modulated by the solar wind. Solar wind is defined to be the expanding plasma that is generated in the solar corona, which has a temperature of about 10^6 Kelvin. It decelerates the incoming particles, which keeps the lower energy GCR from reaching the inner parts of the solar system. The solar magnetic field is stationary and is forced outward from the Sun. Since the field is attached to the Sun and the Sun rotates, the movement leads to the rotation of the magnetic field, which creates an Archimedian spiral as depicted in figure 2 (courtesy of [8]). This geometry, as well as the solar activity level, has a great influence on the flux of GCR.

FIGURE 2: Archimedian Spiral generated by the solar wind

The Earth is protected from cosmic rays by the different layers of atmosphere, namely the ionosphere, heliosphere, and the geomagnetic field. When primary cosmic rays interact with the atmosphere or other materials, they produce fluxes of secondary, tertiary, and higher generation particles.

I.4 RADIATION TRANSPORT

During the last fifty years, the transport of ions through various materials has been studied in depth by many scientists both within and outside of NASA. Specifically, the topic of radiation physics encompasses a wide range of particles from electrons and photons to heavy ions like iron. Its implications traverse across many disciplines such as medical and engineering. Of particular interest to NASA is the transport of heavy ions.

The exposure of space travelers to ionizing radiation is determined by the transport properties of the radiation throughout the spacecraft, such as its onboard systems and the bodies of the individuals themselves. Meeting the challenge of future space programs will therefore require accurate and efficient methods for performing radiation transport calculations to determine and verify shielding requirements. According to a recent National Research Council Report [3], predictions derived from radiation transport calculations need to be tested using a common code for laboratory and space measurements that have been validated with accelerator results.

Beginning in the 1950s, as computational tools began to become more efficient, high energy transport codes began to emerge. The first of which was developed by Oak Ridge National Lab in 1962 and was called HETC (High Energy Transport Code) [9]. This Monte Carlo (statistical) code combined nuclear elastic and inelastic interactions, as well as the decay and interactions of atomic particles. It evaluated the transport of particles with atomic mass of one (protons and neutrons). Following this other codes emerged such as MARS, which is also a Monte Carlo code for the inclusive and exclusive simulation of three-dimensional hadronic and electromagnetic cascades, muons, heavy-ion and low-energy neutron transport in accelerators, detectors, spacecraft, and shielding components. MARS was released in October of 1974 and was primarily used for calculations in particle accelerators [10]. Other Monte Carlo codes that have been developed include FLUKA [9] and MCNPX [9]. In contrast to Monte Carlo codes, there is a class of deterministic codes of which the most well known is the HZETRN [11]. HZETRN is a deterministic high charge and energy (HZE) transport code that was developed at NASA Langley. It solves the one-dimensional Boltzmann transport equation for charged and neutral particles by employing the straight-ahead and continuous slowing down approximations (CSDA) for charged particles.

The transport codes discussed above have a number of advantages and disadvantages. No one code meets the needs of everyone. Monte Carlo codes tend to be computationally inefficient and can require a lot of time even when evaluating relatively simple problems. In addition, it has been noted in [12] that traditional numerical solution methods for the Boltzmann transport equation are best suited for space radiations where the energy spectra are smooth over large energy intervals, and less suited for the simulation of laboratory beams, which exhibit large spectral variation over a very limited energy domain and large energy derivative. As a result, codes based on these methods are not readily validated by comparison with laboratory experiments.

Based on these studies, Wilson and colleagues [12, 13] identified the Green's function technique as the likely means of generating efficient high charge and energy (HZE) shielding codes that are suitable for space engineering analysis and are also capable of being validated in laboratory experiments. In consequence, a laboratory code designed to simulate the transport of heavy ions through a single layer of material was developed [12, 14]. It was based on a Green's function model as a perturbation series with non-perturbative corrections. The code was validated for single layer targets and then extended to handle multi-layer targets [15, 16, 17]. This early code used a scale factor to equate range-energy relations of one material thickness into an equivalent amount of another material, and proceeded to perform the transport calculations in the new material [18]. While this method has proven to be acceptable using low-resolution detectors [16, 19], it is not an accurate reflection of different material properties and is unsuited for high-resolution measurements. Lacking from the prior solutions were range and energy straggling, multiple Coulomb scattering, and energy downshift and dispersion associated with nuclear events. In recent publications [20, 21], it has been shown how these effects can be incorporated into the multiple fragmentation perturbation series leading to the development of a new Green's function code GRNTRN (a GReeN's function code for ion beam TRaNsport). GRNTRN has proven to be accurate in modeling ion beams for a single layer of material [19, 22, 23], and has been extended to handle multiple layers [23]. Unlike the earlier Green's function code, the multi-layer GRNTRN code does not make use of range scaling, but instead transports ions through the target layer by layer. It however does not account for the angular dispersion of the projectile or target. This implies that the code is purely one dimensional since it is based on a solution of the

Boltzmann transport equation that makes use of the straight-ahead approximation. In order to remove the one dimensional limitation, it will be necessary to develop a fully three dimensional GRNTRN code. This dissertation describes the development of such a code.

I.5 OBJECTIVE OF THIS DISSERTATION

In this dissertation, the accuracy and effectiveness of the first step toward a three dimensional radiation transport model using the Green's function technique for heavy ions will be demonstrated. For heavy ions, the energy and angular spread is very narrow and therefore, this model demonstrates a three dimensional correction to the one dimensional Green's function model. Before the introduction to the formulation of the problem and solution, the input parameter of the cross section will be discussed. In chapter II, the formalism for how to obtain a suitable expression for the fragmentation cross sections will be detailed.

Chapter III will go through the formulation of the problem, which includes the Green's function technique for solving the Boltzmann equation, the Neumann series expansion, and the analysis of various environments. The solution of the Boltzmann equation ultimately leads to a Neumann series expansion, which indicates the terms that will need to be calculated, beginning with the zero order Green's function. Then, the influence of several environments on the magnitude of the incoming radiation will be discussed throughout the text.

In chapters III-VII, the discussion of the transport theory, derivations of analytic approximations for the first three terms in the series, and a representation for the remainder of the Neumann series using a nonperturbative technique will be introduced. Within these chapters, several environments will be discussed, including a laboratory and a space environment. To illustrate the effect of the radiation in each environment, several simple geometries will be used as the target material.

The three environments which are discussed in detail will be a laboratory, a uniform isotropic, and a galactic cosmic ray environment. The laboratory environment refers to an incoming flux from a narrow beam that has a Gaussian profile in both angle and energy, and that enters the material at points that are distributed in a Gaussian manner about the mean point of entry. The uniform isotropic environment refers to a radiation environment with a uniform beam of type m particles with a mean energy that are isotropic in direction and have a Gaussian energy profile.

Lastly, for the galactic cosmic ray environment, data from the 1977 solar minimum [11] will be used to represent the incoming broad energy spectra. During a solar minimum, GCR intensities are magnified. This is a consequence of the decreased volume of plasma from the Sun and the reduced interplanetary magnetic fields carried by the solar wind. The 1977 solar minimum is of particular interest because during this time, the GCR fluxes were higher than the previous solar minimum period in 1965 and subsequently higher than most which followed. In addition, these fluxes spanned a broad range of energies. This spectra also has a broad abundance of particles in which all naturally occurring elements are present. However, the six most abundant elements are protons, helium, carbon, oxygen, silicon, and iron as depicted in figure 3. These are the elements which will be discussed in this dissertation.

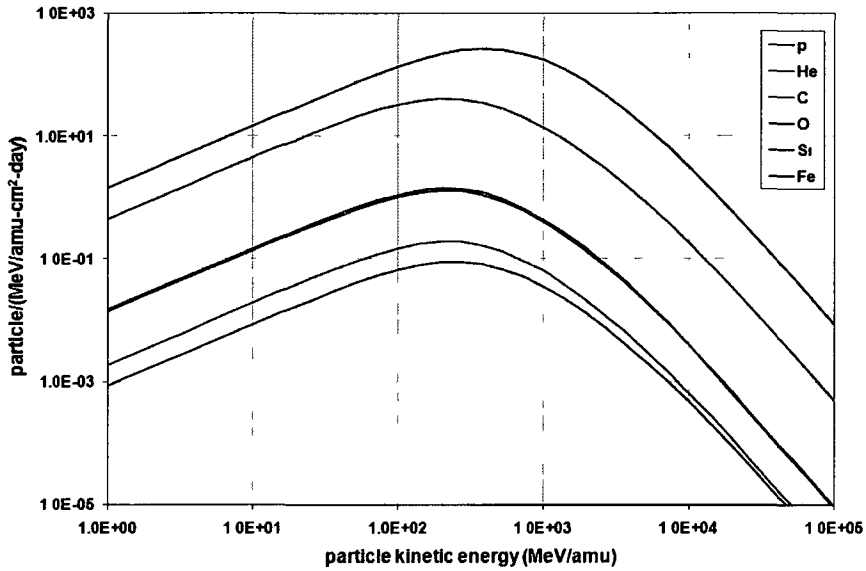

FIGURE 3: The 1977 GCR spectrum.

In Chapter VIII, the Green's function solution of the Boltzmann equation is shown to provide an accurate representation for both laboratory as well as space boundary conditions by showing a qualitative and quantitative comparison with the results obtained by the one dimensional Green's function solution as well as the data obtained by HZETRN. These two comparisons will verify and validate the formulation of the three dimensional Green's technique for the transport of heavy ions in laboratory and space.

CHAPTER II

DOUBLE DIFFERENTIAL CROSS SECTION

II.1 FRAGMENTATION MOMENTUM DEPENDANCE

Before the equations governing the transport of ions through a target material can be formulated and solved, it will be necessary to obtain a suitable expression for the fragmentation cross sections. This will be addressed in the current chapter, where the units of mass will be expressed in amu, and the units of energy in MeV/amu. Unless otherwise stated, all energies are kinetic.

Consideration is given to projectiles of mass A_k and lab frame energy E_k that strike a stationary target with mass A_t and produce fragments with mass A_j and energy E. The total energy is denoted by $\tilde{E} = E + m_p$, where $m_p = 938.272$ MeV is the proton rest mass.

The nuclear fragmentation cross section can be broken up into the total cross section and the fragment momentum distribution as follows

$$\frac{d^3\sigma}{dp^3} = \sigma_{jk}(E_k) f_{jk}(\mathbf{p}). \tag{1}$$

Additionally, experiments have shown that when fragments are produced, they may be projectile-like or target-like. These are fragments that have small momenta in the projectile rest frame or target rest frame respectively. It has also been determined that the fragment's momentum distributions can be approximated by Gaussians in reference frames close to their respective rest frames [24]. Here, it is assumed that in the frame where the average fragment momentum is zero, the distributions are Gaussian.

A * will be used to denote quantities that are evaluated in a frame where the particles have zero average momentum. Those quantities without a * will be evaluated in the laboratory frame. Assuming azimuthal symmetry around the beam axis, the momentum distribution can be approximated as

$$f^*_{jk}(\mathbf{p}^*) \approx N \exp\left(-\frac{p^{*2}_{\parallel}}{2\sigma^2_{\parallel}} - \frac{p^{*2}_{\perp}}{2\sigma^2_{\perp}}\right), \tag{2}$$

where $p^*_{\parallel}$ is the magnitude of the vector $\mathbf{p}^*_{\parallel}$, which is the fragment's momentum

parallel to the beam. Also, $p_{\perp}^{*}$ is the magnitude of the vector $\mathbf{p}_{\perp}^{*}$, which is the fragment's momentum transverse to the beam, and N is a normalization constant, which is chosen so that

$$\int f_{jk}(\mathbf{p}^{*})d^{3}p^{*} = 1. \tag{3}$$

In order to show the correct choice for N, choose the x_3^*-axis of a Cartesian reference frame for the beam direction. Then, since $\mathbf{p}^{*} = \mathbf{p}_{\perp}^{*} + \mathbf{p}_{\parallel}^{*} = (p_1^{*}\mathbf{e}_1^{*} + p_2^{*}\mathbf{e}_2^{*}) + p_3^{*}\mathbf{e}_3^{*}$, we have $p_{\perp}^{*2} = p_1^{*2} + p_2^{*2}$ and $p_{\parallel}^{*2} = p_3^{*2}$ showing that

$$\begin{aligned}\int f_{jk}(\mathbf{p}^{*})d^{3}p^{*} &\approx N\int_{\Re^3}\exp\left(-\frac{p_3^{*2}}{2\sigma_{\parallel}^{2}} - \frac{p_1^{*2}+p_2^{*2}}{2\sigma_{\perp}^{2}}\right)d^{3}p^{*} \\ &= N(2\pi)^{\frac{3}{2}}\sigma_{\parallel}\sigma_{\perp}^{2}.\end{aligned} \tag{4}$$

It thus follows that

$$N \approx (2\pi)^{-\frac{3}{2}}\sigma_{\parallel}^{-1}\sigma_{\perp}^{-2}. \tag{5}$$

The lab frame momentum distribution $f_{jk}(\mathbf{p})$ can be deduced from equation (2) by making use of the Lorentz transformations between the * frame and the lab frame. As is customary in particle physics, the speed of light is chosen as the unit of velocity, $c = 1$. On transforming to the lab frame, while keeping in mind the f_{jk} transforms like $\frac{1}{dp^3}$ and that $\frac{\tilde{E}}{dp^3}$ is Lorentz invariant, it is found that

$$f_{jk}(\mathbf{p}) \approx \frac{\tilde{E}^{*}}{\tilde{E}}N\exp\left(-\frac{p_{\parallel}^{*2}}{2\sigma_{\parallel}^{2}} - \frac{p_{\perp}^{2}}{2\sigma_{\perp}^{2}}\right), \tag{6}$$

where $\tilde{E}^{*}$ is the total energy in the * frame and $\tilde{E}$ is the total energy in the lab frame. Additionally,

$$\tilde{E}^{*} = \gamma_{L}(\tilde{E} - \beta_{L}p_{\parallel}), \tag{7}$$

$$p_{\parallel}^{*} = \gamma_{L}(p_{\parallel} - \beta_{L}\tilde{E}), \tag{8}$$

$$p_{\perp}^{*} = p_{\perp} \tag{9}$$

where $p_{\perp} = p\sin\theta$, $p_{\parallel} = p\cos\theta$, and $p = p(\tilde{E}) = \sqrt{\tilde{E}^2 - m_p^2}$, and θ is the lab frame scattering angle. β_{L} and γ_{L} are the Lorentz factors and are given by $\beta_{L} = \sqrt{1-\gamma_{L}^{-2}}$ where γ_{L} is seen to be related to the lab frame energy downshift E_s by $\gamma_{L} = \frac{E_s}{m_p}$ for target-like fragments and by $\gamma_{L} = \frac{\tilde{E}_k - E_s}{m_p}$ for projectile-like fragments.

It is now clear that the fragmentation momentum distribution, $f_{jk}(\mathbf{p})$, is completely determined once the parameters $\sigma_{\parallel}$, $\sigma_{\perp}$, and E_s are known. An approximation that will be made at this point is to assume that the fragmentation is isotropic in the * frame. In which case, $\sigma_{\perp} = \sigma_{\parallel}$. One experiment has shown to verify this approximation to within about 10 percent [24].

According to Tripathi et al. [25], $\sigma_{\parallel}$ and the momentum downshift p_s^*, both measured in MeV/c/amu, can be approximated as

$$\sigma_{\parallel} = \frac{1}{A_j}\sqrt{\frac{m_p}{3}\left(\frac{45}{A_k^{1/3}} - \frac{25}{A_k^{2/3}}\right)\left(\frac{A_j(A_k - A_j)}{A_j - 1}\right)}, \tag{10}$$

and

$$p_s^* = \frac{1}{A_j}\left[3.64\left(9 + \frac{A_j}{A_k}\right)\sqrt{\frac{9}{A_k^{1/3}} - \frac{5}{A_k^{2/3}}} - 28\right]. \tag{11}$$

Before the collision, the projectiles have the total energy $\tilde{E}_k^* = m_p$ and momentum, $p_k^* = 0$. As a result of the collision, fragments are produced with momentum p_s^* and corresponding total energy $\tilde{E}_s^* = \sqrt{(p_s^*)^2 + m_p^2}$. The change in energy is therefore given by $E_s^* = \tilde{E}_s^* - m_p = \sqrt{(p_s^*)^2 + m_p^2} - m_p$.

On transforming to the lab frame, it is found by means of the Lorentz Transformations that the laboratory frame collision energy downshift is given by

$$E_s = \gamma_k[E_s^* + \beta_k p_s^*] = \gamma_k\left[\sqrt{p_s^{*2} + m_p^2} - m_p + \beta_k p_s^*\right], \tag{12}$$

where γ_k is the projectile Lorentz factor and is given by $\gamma_k = \tilde{E}_k/m_p$, and β_k is the projectile Beta factor and is given by $\beta_k = \sqrt{1 - \gamma_k^{-2}}$.

Let $\theta = \cos^{-1}(\mathbf{\Omega} \cdot \mathbf{\Omega_k})$ be the lab scattering angle and let (p, θ, ϕ) be the spherical polar coordinates in momentum space with polar axis in the incident beam direction, $\mathbf{\Omega_k}$. Since there is axial symmetry,

$$\begin{aligned}\int f_{jk}(\mathbf{p})d^3p &= \int f_{jk}(\mathbf{p})p^2\sin\theta dpd\theta d\phi = \int 2\pi f_{jk}(\mathbf{p})p^2\sin\theta dpd\theta \\ &= \int 2\pi f_{jk}(\mathbf{p})p_{\perp}\tilde{E}d\tilde{E}d\theta = \int f(\theta, E, E_k)d\theta dE,\end{aligned} \tag{13}$$

where we have made use of the relations $\tilde{E}^2 = p^2 + m_p^2$ and $\tilde{E} = E + m_p$. Equation (13) implies that the energy angle distribution is given by $f(\theta, E, E_k) = 2\pi p_{\perp}\tilde{E}f_{jk}(\mathbf{p})$. It

thus follows that the angle and energy dependent macroscopic cross section is given by

$$\sigma_{jk}(\mathbf{\Omega}\cdot\mathbf{\Omega_k}, E, E_k) = \sigma_{jk}(\cos\theta, E, E_k) = \sigma_{jk}(E_k) f(\theta, E, E_k), \tag{14}$$

where $\sigma_{jk}(E_k)$ is the corresponding total cross section,

$$f(\theta, E, E_k) = \frac{p_\perp \tilde{E}^*}{\sqrt{2\pi}\sigma_\parallel \sigma_\perp^2} \exp\left(-\frac{p_\parallel^{*2}}{2\sigma_\parallel^2} - \frac{p_\perp^2}{2\sigma_\perp^2}\right), \tag{15}$$

and $\tilde{E}^* = \gamma_L\left(\tilde{E} - \beta_L\sqrt{\tilde{E}^2 - m_p^2}\cos\theta\right)$.

Finally, assuming an isotropic momentum distribution in the * frame, the momentum distribution can be represented as

$$\begin{aligned} f(\theta, E, E_k) &\approx \frac{1}{\sqrt{(2\pi)^3}\sigma_\parallel^3} \exp\left(-\frac{p^{*2}}{2\sigma_\parallel^2}\right) \\ &= \frac{1}{\sqrt{(2\pi)^3}\sigma_\parallel^3} \exp\left(\frac{m_p^2}{2\sigma_\parallel^2}\right) \exp\left(-\frac{\tilde{E}^{*2}}{2\sigma_\parallel^2}\right), \end{aligned} \tag{16}$$

and transforming to the lab frame yields (S. Blattnig, personal communication, Sept. 2009)

$$f(\theta, E, E_k) = \frac{p(\tilde{E})\tilde{E}^*[\tilde{E}, \theta]\sin\theta}{\sqrt{2\pi}\sigma_\parallel^3} \exp\left(-\frac{\tilde{E}^*[\tilde{E}, \theta]^2 - m_p^2}{2\sigma_\parallel^2}\right). \tag{17}$$

II.1.1 Energy Distribution

To determine the **energy distribution**, integrate over all relevant angles

$$\begin{aligned} f_E(E, E_k) &= \int_0^{\theta_{max}} f(\theta, E, E_k) d\theta \\ &= \frac{1}{\sqrt{2\pi}\sigma_\parallel^3} \int_0^{\theta_{max}} p(\tilde{E})\tilde{E}^*[\tilde{E}, \theta]\sin\theta \exp\left(-\frac{\tilde{E}^*[\tilde{E}, \theta]^2 - m_p^2}{2\sigma_\parallel^2}\right) d\theta. \end{aligned} \tag{18}$$

Using a substitution of $z = \frac{\tilde{E}^{*2}}{2\sigma_{\parallel}^2}$

$$\begin{aligned} f_E(E, E_k) &= \frac{1}{\sqrt{2\pi}\gamma_L\beta_L\sigma_{\parallel}} \exp\left(\frac{m_p^2}{2\sigma_{\parallel}^2}\right) \int_{z_0}^{z_{\theta max}} \exp(-z)dz \\ &= \frac{1}{\sqrt{2\pi}\gamma_L\beta_L\sigma_{\parallel}} \exp\left(\frac{m_p^2}{2\sigma_{\parallel}^2}\right) \left[-\exp\left(-\frac{\tilde{E}^{*2}}{2\sigma_{\parallel}^2}\right)\right]_{\theta=0}^{\theta=\theta_{max}} \\ &= \frac{1}{\sqrt{2\pi}\gamma_L\beta_L\sigma_{\parallel}} \exp\left(\frac{m_p^2}{2\sigma_{\parallel}^2}\right) \\ &\quad \cdot \left[\exp\left(-\frac{\tilde{E}^*(\tilde{E}, 0)^2}{2\sigma_{\parallel}^2}\right) - \exp\left(-\frac{\tilde{E}^*(\tilde{E}, \theta_{max})^2}{2\sigma_{\parallel}^2}\right)\right] \end{aligned} \tag{19}$$

(S. Blattnig, personal communication, Sept. 2009).

II.1.2 Angular Distribution

Similarly, the **angular distribution** is given by

$$\begin{aligned} f_\theta(\theta, E_k) &= \int_{E_{min}}^{E_{max}} f(\theta, E, E_k)dE \\ &= \int_{E_{min}}^{E_{max}} \frac{p(\tilde{E})\tilde{E}^*[\tilde{E}, \theta]\sin\theta}{\sqrt{2\pi}\sigma_{\parallel}^3} \exp\left(-\frac{\tilde{E}^*[\tilde{E}, \theta]^2 - m_p^2}{2\sigma_{\parallel}^2}\right) dE, \end{aligned} \tag{20}$$

and can be evaluated by numerical quadrature (S. Blattnig, personal communication, Sept. 2009).

II.2 GAUSSIAN APPROXIMATIONS

In this section, it will be shown that the previously obtained fragment momentum distribution can be approximated as a bi-variate Gaussian distribution. To this end, it may be recalled that the laboratory energy-angle distribution is given by

$$f(\theta, E, E_k) = \frac{p(\tilde{E})\tilde{E}^*[\tilde{E},\theta]\sin\theta}{\sqrt{2\pi}\sigma_{\parallel}^3}\exp\left(-\frac{\tilde{E}^*[\tilde{E},\theta]^2 - m_p^2}{2\sigma_{\parallel}^2}\right), \tag{21}$$

where $\tilde{E}^*$ is obtained through the Lorentz transformation $\tilde{E}^* = \gamma_{_L}\left[\tilde{E} - \beta_{_L} p\cos\theta\right]$. Additionally, since c has been chosen as the unit of velocity, the energy-momentum relation takes the form $\tilde{E}^2 = p^2 + m_p^2$, which shows that $\tilde{E}^*$ may be expressed in terms of $\tilde{E}$ and θ through the formula

$$\tilde{E}^* = \gamma_{_L}\left[\tilde{E} - \beta_{_L}\sqrt{\tilde{E}^2 - m_p^2}\cos\theta\right]. \tag{22}$$

Since the exponential function appearing in equation (21) achieves its maximum at the minimum value of $\tilde{E}^*[\tilde{E},\theta]^2 - m_p^2$, it will be useful to determine where this occurs. For a given $\theta \in [0, \pi/2]$, $\tilde{E}^*[\tilde{E},\theta]$ achieves its minimum when

$$\frac{\partial\tilde{E}^*}{\partial\tilde{E}} = \gamma_{_L}\left[1 - \beta_{_L}\frac{\tilde{E}}{\sqrt{\tilde{E}^2 - m_p^2}}\cos\theta\right] = 0, \tag{23}$$

or when $\tilde{E} = \frac{m_p}{\sqrt{1-\beta_{_L}^2\cos^2\theta}}$. However, if $\theta \in [\pi/2, \pi]$, then $\tilde{E}^*[\tilde{E},\theta]$ is a non-negative increasing function of $\tilde{E}$ and therefore its minimum value occurs when $\tilde{E} = m_p$. On combining these results, it is found that for a given $\theta \in [0, \pi]$, $\tilde{E}^*[\tilde{E},\theta]$ achieves its minimum when

$$\tilde{E} = \tilde{E}^0(\theta) = \begin{cases} \frac{m_p}{\sqrt{1-\beta_{_L}^2\cos^2\theta}} & (0 \le \theta \le \pi/2) \\ m_p & (\pi/2 \le \theta \le \pi). \end{cases} \tag{24}$$

It should now be observed that $\tilde{E}^*[\tilde{E},\theta]$ is an increasing function of $\theta \in [0, \pi]$, and therefore its global minimum occurs when $\theta = 0$ and $\tilde{E} = \tilde{E}^0(0) = \frac{m_p}{\sqrt{1-\beta_{_L}^2}} = \gamma_{_L} m_p$. For projectile fragments, it was determined that the Lorentz factor is $\gamma_{_L} = \frac{\tilde{E}_k - E_s}{m_p}$, so the global minimum occurs when $\theta = 0$ and $\tilde{E} = \tilde{E}_k - E_s$ and thus $E = E_k - E_s$.

For target fragments, the Lorentz factor is $\gamma_{_L} = \frac{E_s}{m_p}$, and the global minimum occurs when $\theta = 0$ and $\tilde{E} = E_s$ or $E = E_s$.

For small values of θ, $\mu = 1 - \cos\theta$ is also small. Therefore, on using the binomial theorem, $\tilde{E}^0(\theta)$ can be approximated as

$$\begin{aligned}
\tilde{E}^0(\theta) &= \frac{m_p}{\sqrt{1-\beta_{_L}^2\cos^2\theta}} = \frac{m_p}{\sqrt{1-\beta_{_L}^2(1-\mu)^2}} \\
&= \gamma_{_L} m_p[1+\gamma_{_L}^2\beta_{_L}^2(2\mu-\mu^2)]^{-\frac{1}{2}} = \gamma_{_L} m_p[1-\gamma_{_L}^2\beta_{_L}^2\mu + O(\mu^2)] \\
&\approx \gamma_{_L} m_p - \gamma_{_L}^3\beta_{_L}^2 m_p\mu = \gamma_{_L} m_p + \epsilon_0(\theta),
\end{aligned} \tag{25}$$

where

$$\epsilon_0(\theta) = -\gamma_{_L}^3\beta_{_L}^2 m_p\mu. \tag{26}$$

Observe that

$$p[\tilde{E}^0(\theta)] = \sqrt{\tilde{E}^0(\theta)^2 - m_p^2} = H[\pi/2-\theta]\beta_{_L} m_p\cos\theta(1-\beta_{_L}^2\cos^2\theta)^{-\frac{1}{2}}, \tag{27}$$

and

$$\begin{aligned}
\tilde{E}^*[\tilde{E}^0(\theta),\theta] &= \gamma_{_L}\left(\tilde{E}^0(\theta) - \beta_{_L} p[\tilde{E}^0(\theta)\cos\theta]\right) \\
&= \begin{cases} \gamma_{_L} m_p(1-\beta_{_L}^2\cos^2\theta)^{\frac{1}{2}} & (0 \le \theta \le \pi/2) \\ \gamma_{_L} m_p & (\pi/2 \le \theta \le \pi), \end{cases}
\end{aligned} \tag{28}$$

where $H[x]$ is the Heaviside function.

Combining these two results,

$$p[\tilde{E}^0(\theta)]\tilde{E}^*[\tilde{E}^0(\theta),\theta] = H[\pi/2-\theta]\gamma_{_L}\beta_{_L} m_p^2\cos\theta. \tag{29}$$

For small values of θ,

$$p[\tilde{E}^0(\theta)] = \tilde{E}^0(\theta)\beta_{_L}\cos\theta \approx [\gamma_{_L} m_p + \epsilon_0(\theta)]\beta_{_L}\cos\theta, \tag{30}$$

$$\begin{aligned}\tilde{E}^*[\tilde{E}^0(\theta),\theta] &= \gamma_{_L} m_p(1-\beta_{_L}^2\cos^2\theta)^{\frac{1}{2}} = \gamma_{_L} m_p(1-\beta_{_L}^2(1-\mu)^2)^{\frac{1}{2}} \\ &= m_p(1+\gamma_{_L}^2\beta_{_L}^2(2\mu-\mu^2))^{\frac{1}{2}} \\ &\approx \gamma_{_L}^{-1}(\gamma_{_L} m_p + \gamma_{_L}^3\beta_{_L}^2 m_p\mu) = \gamma_{_L}^{-1}(\gamma_{_L} m_p - \epsilon_0(\theta)), \end{aligned} \tag{31}$$

and

$$p[\tilde{E}^0(\theta)]\tilde{E}^*[\tilde{E}^0(\theta),\theta] = \gamma_{_L}\beta_{_L} m_p^2(1-\mu). \tag{32}$$

If these expressions are evaluated at $\theta = 0$, we have that

$$\begin{aligned} p[\tilde{E}^0(0)] &= \sqrt{\gamma_{_L}^2 m_p^2 - m_p^2} = \gamma_{_L}\beta_{_L} m_p, \\ \tilde{E}^*[\tilde{E}^0(0),0] &= m_p, \\ p[\tilde{E}^0(0)]\tilde{E}^*[\tilde{E}^0(0),0] &= \gamma_{_L}\beta_{_L} m_p^2. \end{aligned}$$

II.2.1 Small Parameter Expansions

Since $\tilde{E}^*[\tilde{E}^0(\theta),\theta]$ achieves its minimum when $\tilde{E} = \gamma_{_L} m_p$ and $\theta = 0$, a power series expansion can be constructed about this point in terms of the small parameters ϵ and μ, that are defined by $\tilde{E} = \gamma_{_L} m_p + \epsilon$ and $\mu = 1 - \cos\theta$. In the approach taken, expansions are first constructed for $p(\tilde{E})$, $\tilde{E}^*(\tilde{E},0)$, $\tilde{E}^*(\tilde{E},\theta)$, $\tilde{E}^*(\tilde{E},0)^2 - m_p^2$, and $\tilde{E}^*(\tilde{E},\theta)^2 - m_p^2$. The expansions are then combined to obtain the desired result.

The first to be considered is $p(\tilde{E})$.

$$\begin{aligned} p(\tilde{E}) &= p(\gamma_{_L} m_p + \epsilon) = \sqrt{(\gamma_{_L} m_p + \epsilon)^2 - m_p^2} = \gamma_{_L}\beta_{_L} m_p\left[1 + \frac{2\gamma_{_L} m_p\epsilon + \epsilon^2}{\gamma_{_L}^2\beta_{_L}^2 m_p^2}\right]^{1/2} \\ &= m_p\gamma_{_L}\beta_{_L} + \frac{1}{\beta_{_L}}\epsilon - \frac{1}{2m_p\gamma_{_L}^3\beta_{_L}^3}\epsilon^2 + O(\epsilon^3). \end{aligned} \tag{33}$$

The next to be considered is the expansion for $\tilde{E}^*(\tilde{E},0)$,

$$\begin{aligned}
\tilde{E}^*(\gamma_{_L} m_p + \epsilon, 0) &= \gamma_{_L}\left[(\gamma_{_L} m_p + \epsilon) - \beta_{_L} p(\gamma_{_L} m_p + \epsilon)\right] \\
&= \gamma_{_L}\left[\gamma_{_L} m_p - \beta_{_L}\left\{m_p \gamma_{_L}\beta_{_L} + \frac{1}{\beta_{_L}}\epsilon - \frac{1}{2m_p\gamma_{_L}^3\beta_{_L}^3}\epsilon^2 + O(\epsilon^3)\right\}\right] \\
&= \gamma_{_L}^2(1-\beta_{_L}^2)m_p^2 + 0\epsilon + \frac{\epsilon^2}{2\gamma_{_L}^3\beta_{_L}^2 m_p} + O(\epsilon^3) \\
&= m_p + \frac{\epsilon^2}{2\gamma_{_L}^2\beta_{_L}^2 m_p} + O(\epsilon^3). \qquad (34)
\end{aligned}$$

The next expansion can be derived by using the two previous expansions.

$$\begin{aligned}
\tilde{E}^*(\tilde{E}, \theta) &= \gamma_{_L}[\tilde{E} - \beta_{_L} p(\tilde{E})\cos\theta] \\
&= \tilde{E}^*(\tilde{E}, 0) + \gamma_{_L}\beta_{_L} p(\tilde{E})\mu \\
&= m_p + \frac{\epsilon^2}{2\gamma_{_L}^2\beta_{_L}^2 m_p} + O(\epsilon^3) \\
&\quad + \gamma_{_L}\beta_{_L}\left[m_p\gamma_{_L}\beta_{_L} + \frac{1}{\beta_{_L}}\epsilon - \frac{1}{2m_p\gamma_{_L}^3\beta_{_L}^3}\epsilon^2 + O(\epsilon^3)\right]\mu \\
&= m_p + \frac{1}{2\gamma_{_L}^2\beta_{_L}^2 m_p}\epsilon^2 + (\gamma_{_L}^2\beta_{_L}^2 m_p + \gamma\epsilon)\mu + O(\epsilon^3). \qquad (35)
\end{aligned}$$

Then, the expansion of $\tilde{E}^*(\tilde{E}, 0)^2 - m_p^2$ follows naturally from the results above

$$\begin{aligned}
\tilde{E}^*(\tilde{E}, 0)^2 - m_p^2 &= \tilde{E}^*(\gamma_{_L} m_p + \epsilon, 0)^2 - m_p^2 \\
&= \left[m_p + \frac{1}{2\gamma_{_L}^2\beta_{_L}^2 m_p}\epsilon^2 + O(\epsilon^3)\right]^2 - m_p^2 \\
&= \frac{\epsilon^2}{\gamma_{_L}^2\beta_{_L}^2} + O(\epsilon^4). \qquad (36)
\end{aligned}$$

And, finally the expansion for $\tilde{E}^*(\tilde{E}, \theta)^2 - m_p^2$ can also be constructed,

$$\begin{aligned}
\tilde{E}^*(\tilde{E},\theta)^2 - m_p^2 &= \left[\tilde{E}^*(\tilde{E},0) + \gamma_{_L}\beta_{_L}p(\tilde{E})\mu\right]^2 - m_p^2 \\
&= \tilde{E}^*(\tilde{E},0)^2 - m_p^2 + 2\gamma_{_L}\beta_{_L}p(\tilde{E})\tilde{E}^*(\tilde{E},0)\mu + \gamma_{_L}^2\beta_{_L}^2p(\tilde{E})^2\mu^2 \\
&= \frac{\epsilon^2}{\gamma_{_L}^2\beta_{_L}^2} + O(\epsilon^4) + 2\gamma_{_L}\beta_{_L}(m_p\gamma_{_L}\beta_{_L} + \frac{1}{\beta_{_L}}\epsilon - \frac{1}{2m_p\gamma_{_L}^3\beta_{_L}^3}\epsilon^2 + O(\epsilon^3)) \\
&\quad \cdot(m_p + \frac{\epsilon^2}{2\gamma_{_L}^2\beta_{_L}^2m_p} + O(\epsilon^3))\mu + \gamma_{_L}^2\beta_{_L}^2(m_p\gamma_{_L}\beta_{_L} \\
&\quad + \frac{1}{\beta_{_L}}\epsilon - \frac{1}{2m_p\gamma_{_L}^3\beta_{_L}^3}\epsilon^2 + O(\epsilon^3))^2\mu^2 \\
&= \frac{1}{(\gamma_{_L}\beta_{_L})^2}\epsilon^2 + (\gamma_{_L}^2\beta_{_L}^2m_p)^2\mu^2 + 2\gamma_{_L}m_p\mu\epsilon + 2(\gamma_{_L}\beta_{_L}m_p)^2\mu + O(\epsilon^3) \\
&= \frac{1}{\gamma_{_L}^2\beta_{_L}^2}(\epsilon + \gamma_{_L}^3\beta_{_L}^2m_p\mu)^2 + \gamma_{_L}^2\beta_{_L}^2m_p^2(2\mu - \mu^2) + O(\epsilon^3). \qquad (37)
\end{aligned}$$

Thus

$$\tilde{E}^*(\tilde{E},\theta)^2 - m_p^2 = \frac{(\epsilon - \epsilon_0(\theta))^2}{(\gamma_{_L}\beta_{_L})^2} + \gamma_{_L}^2\beta_{_L}^2m_p^2\sin^2\theta + O(\epsilon^3), \qquad (38)$$

where $\epsilon_0(\theta)$ is given by (26).

II.2.2 Approximate Energy Distribution

Now, apply the expansion of $\tilde{E}^*(\tilde{E},0)$ to the energy distribution exponential in equation (19). Recall that the energy distribution was given by,

$$\begin{aligned}
f_{_E}(E,E_k) &= \int_0^{\theta_{max}} f(\theta,E,E_k)d\theta \\
&= \frac{1}{\sqrt{2\pi}\sigma_{_\parallel}\gamma_{_L}\beta_{_L}}\exp\left(\frac{m_p^2}{2\sigma_{_\parallel}^2}\right)\left[\exp\left(-\frac{\tilde{E}^*[\tilde{E},0]^2}{2\sigma_{_\parallel}^2}\right)\right. \\
&- \left.\exp\left(-\frac{\tilde{E}^*[\tilde{E},\theta_{max}]^2}{2\sigma_{_\parallel}^2}\right)\right], \qquad (39)
\end{aligned}$$

and when use has been made of the $\tilde{E}^*[\tilde{E},0]$ expansion, equation (34), the energy distribution can be approximated as

$$\begin{aligned} f_E(E,E_k) &\approx \frac{1}{\sqrt{2\pi}\sigma_{\parallel}\gamma_L\beta_L}\left[\exp\left(-\frac{\tilde{E}^{*2}[\tilde{E},0]-m_p^2}{2\sigma_{\parallel}}\right)\right] \\ &\approx \frac{1}{\sqrt{2\pi}(\sigma_{\parallel}\gamma_L\beta_L)}\exp\left\{-\frac{\epsilon^2}{2(\sigma_{\parallel}\gamma_L\beta_L)^2}\right\} \\ &\approx \frac{1}{\sqrt{2\pi}(\sigma_{\parallel}\gamma_L\beta_L)}\exp\left\{-\frac{[\tilde{E}_k-E_s-\tilde{E}]^2}{2(\sigma_{\parallel}\gamma_L\beta_L)^2}\right\}. \end{aligned} \tag{40}$$

II.2.3 Approximate Angular Distribution

The angular distribution can be calculated by quadrature, as previously noted, but for computational efficiency a closed form approximation is desired.

Recall that the angular distribution is given by

$$\begin{aligned} f_\theta(\theta,E_k) &= \int_{E_{min}}^{E_{max}} f(\theta,E,E_k)dE \\ &= \int_{E_{min}}^{E_{max}} \frac{p(\tilde{E})\tilde{E}^*[\tilde{E},\theta]\sin\theta}{\sqrt{2\pi}\sigma_{\parallel}^3}\exp\left(-\frac{\tilde{E}^*[\tilde{E},\theta]^2-m_p^2}{2\sigma_{\parallel}^2}\right)dE, \end{aligned} \tag{41}$$

and that $\tilde{E}=E+m_p=\gamma_L m_p+\epsilon$.

Then, by use of equation (38), it is found that

$$\begin{aligned} f_\theta(\theta,E_k) &\approx \int_{\Re}\frac{p(\tilde{E})\tilde{E}^*[\tilde{E},\theta]\sin\theta}{\sqrt{2\pi}\sigma_{\parallel}^3}\exp\left(-\frac{\frac{(\epsilon-\epsilon_0(\theta))^2}{(\gamma_L\beta_L)^2}+\gamma_L^2\beta_L^2m_p^2\sin^2\theta+\ldots}{2\sigma_{\parallel}^2}\right)d\epsilon \\ &\approx \frac{\gamma_L\beta_L\sin\theta}{\sigma_{\parallel}^2}\exp\left(-\frac{\gamma_L^2\beta_L^2m_p^2\sin^2\theta}{2\sigma_{\parallel}^2}\right) \\ &\quad\cdot\int_{\Re}\frac{p(\tilde{E})\tilde{E}^*[\tilde{E},\theta]}{\sqrt{2\pi}\sigma_{\parallel}\gamma_L\beta_L}\exp\left(-\frac{(\epsilon-\epsilon_0(\theta))^2}{2\sigma_{\parallel}^2\gamma_L^2\beta_L^2}\right)d\epsilon. \end{aligned} \tag{42}$$

In order to approximate this integral, it is first noted that the exponential term achieves its maximum when $\epsilon=\epsilon_0(\theta)$, where

$$\tilde{E}=\tilde{E}^0=\gamma_L m_p+\epsilon_0(\theta). \tag{43}$$

Also, since $p(\tilde{E})\tilde{E}^*[\tilde{E},\theta]$ is a slowly varying function of $\tilde{E}$ and

$$p(\tilde{E}^0(\theta))\tilde{E}^*[\tilde{E}^0(\theta),\theta] = H[\pi/2-\theta]\gamma_{_L}\beta_{_L}m_p^2\cos\theta, \tag{44}$$

use of the mean value theorem yields the approximation,

$$f_\theta(\theta,E_k) \approx H[\pi/2-\theta]\frac{\gamma_{_L}^2\beta_{_L}^2m_p^2\sin\theta\cos\theta}{\sigma_{_\parallel}^2}\exp\left(-\frac{\gamma_{_L}^2\beta_{_L}^2m_p^2\sin^2\theta}{2\sigma_{_\parallel}^2}\right). \tag{45}$$

II.2.4 Approximate Energy-Angle Distribution

Combining the energy-angle distribution given by equation (21) and the result given in equation (38), the distribution can be approximated as

$$\begin{aligned} f(\theta,E,E_k) &\approx \frac{p(\tilde{E})\tilde{E}^*[\tilde{E},\theta]\sin\theta}{\sqrt{2\pi}\sigma_{_\parallel}^3}\exp\left(-\frac{(\epsilon-\epsilon_0(\theta))^2}{2\sigma_{_\parallel}^2\gamma_{_L}^2\beta_{_L}^2}\right) \\ &\quad\cdot\exp\left(-\frac{\gamma_{_L}^2\beta_{_L}^2m_p^2\sin^2\theta}{2\sigma_{_\parallel}^2}\right), \end{aligned} \tag{46}$$

where $\tilde{E}=\gamma_{_L}m_p+\epsilon$, $\mu=1-\cos\theta$, and $\epsilon_0(\theta)=-\gamma_{_L}^3\beta_{_L}^2m_p\mu$.

Since $\tilde{E}=\gamma_{_L}m_p+\epsilon_0(\theta)+[\epsilon-\epsilon_0(\theta)]=\tilde{E}^0(\theta)+[\epsilon-\epsilon_0(\theta)]$, a further approximation yields

$$\begin{aligned} f(\theta,E,E_k) &\approx \frac{p(\tilde{E}^0(\theta))\tilde{E}^*[\tilde{E}^0(\theta),\theta]\sin\theta}{\sqrt{2\pi}\sigma_{_\parallel}^3}\exp\left(-\frac{(\epsilon-\epsilon_0(\theta))^2}{2\sigma_{_\parallel}^2\gamma_{_L}^2\beta_{_L}^2}\right) \\ &\quad\cdot\exp\left(-\frac{\gamma_{_L}^2\beta_{_L}^2m_p^2\sin^2\theta}{2\sigma_{_\parallel}^2}\right) \\ &\approx \frac{H[\pi/2-\theta]\gamma_{_L}\beta_{_L}m_p^2\cos\theta\sin\theta}{\sqrt{2\pi}\sigma_{_\parallel}^3}\exp\left(-\frac{(\epsilon-\epsilon_0(\theta))^2}{2\sigma_{_\parallel}^2\gamma_{_L}^2\beta_{_L}^2}\right) \\ &\quad\cdot\exp\left(-\frac{\gamma_{_L}^2\beta_{_L}^2m_p^2\sin^2\theta}{2\sigma_{_\parallel}^2}\right), \end{aligned} \tag{47}$$

where use has been made of equation (44). Lastly, since $\epsilon-\epsilon_0(\theta)=\epsilon+\gamma_{_L}^3\beta_{_L}^2m_p(1-\cos\theta)=\epsilon+O(\theta^2)$, a final approximation allows the energy-angle distribution to be

expressed in the form

$$f(\theta, E, E_k) \approx f_E(E, E_k) f_\theta(\theta, E_k), \tag{48}$$

where $f_E(E, E_k)$ is given by equation (40), and $f_\theta(\theta, E_k)$ is given by equation (45).

II.2.5 The Double Differential Cross Section

The calculation of the first and higher order Green's functions require an accurate representation for the double differential cross sections, which was derived in this chapter. Let $\sigma_{jk}(\mathbf{\Omega}, \mathbf{\Omega_k}, E, E_k)$ be the double differential cross section for the production of type j ions of energy E in the direction $\mathbf{\Omega}$ from type k ions of energy E_k in the direction $\mathbf{\Omega_k}$. Then

$$\begin{aligned} \sigma_{jk}(\mathbf{\Omega}, \mathbf{\Omega_k}, E, E_k) d\mathbf{\Omega} dE &= \sigma_{jk}(\mathbf{\Omega}, \mathbf{\Omega_k}, E, E_k) 2\pi \sin\theta d\theta dE \\ &= \sigma_{jk}(E_k) f(\theta, E, E_k) d\theta dE. \end{aligned} \tag{49}$$

Therefore,

$$\sigma_{jk}(\mathbf{\Omega}, \mathbf{\Omega_k}, E, E_k) = \frac{\sigma_{jk}(E_k) f(\theta, E, E_k)}{2\pi \sin\theta} = \sigma_{jk}(E_k) f_E(E, E_k) f_\Omega(\mathbf{\Omega}, \mathbf{\Omega_k}, E_k), \tag{50}$$

where

$$\begin{aligned} f_\Omega(\mathbf{\Omega}, \mathbf{\Omega_k}, E_k) &= \frac{f_\theta(\theta, E_k)}{2\pi \sin\theta} \\ &= H[\pi/2 - \theta] \frac{\gamma_L^2 \beta_L^2 m_p^2 \cos\theta}{2\pi\sigma_\parallel^2} \exp\left(-\frac{\gamma_L^2 \beta_L^2 m_p^2 \sin^2\theta}{2\sigma_\parallel^2} \right). \end{aligned} \tag{51}$$

The final expression for the double differential cross section as given by equation (50) will be utilized throughout the remainder of this dissertation.

II.2.6 Energy-Angle Distribution Results

A comparison can be done to show the accuracy of the approximation for the energy-angle distribution by comparing the expression for the energy-angle distribution as given by equation (17), and the derived approximate solution for the energy-angle distribution, equation (48). For this study, the projectile is taken to be an iron (^{56}Fe) beam with mean energy 1000 MeV/amu, and the target as aluminum (^{27}Al). The fragments considered are hydrogen (^{1}H), oxygen (^{16}O), calcium (^{40}Ca), and manganese (^{54}Mn). For each fragment shown, the figure on the left illustrates the profile of the solution as given by equation (17), and the figure on the right is the relative error plot, which compares the momentum distributions given by equations (17) and (48) respectively. In the figures to follow, there are a few observations that should be discussed. First, notice that the error between the two solutions achieves its minimum value close to the peak value of the momentum distribution. Also, notice that as the ions increase in mass, the percent error decreases. This indicates that the approximation is more accurate for heavier ions as expected. **Note that the magnitudes of the energy-angle distributions and relative percent error are not the same in the figures to follow.**

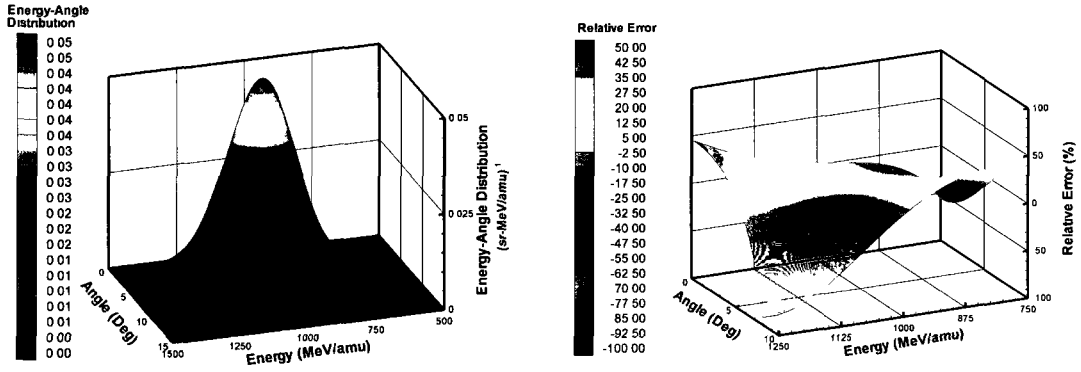

FIGURE 4: The energy-angle distribution and relative error for the ^{1}H fragment.

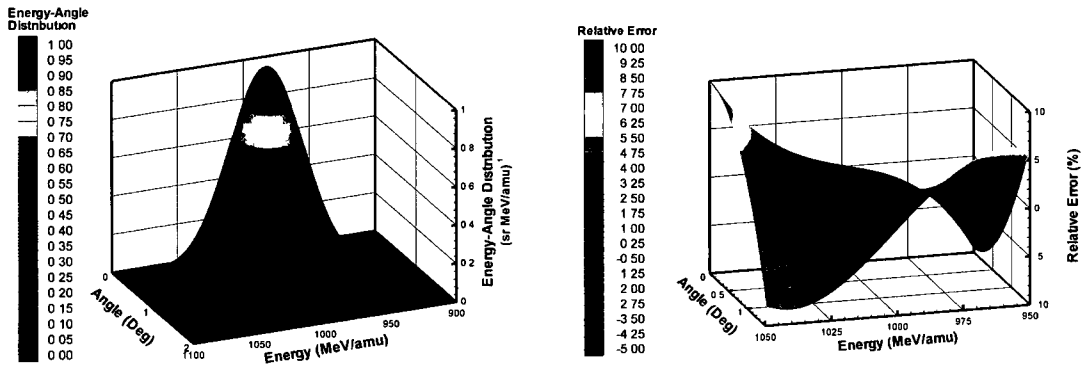

FIGURE 5: The energy-angle distribution and relative error for the ^{16}O fragment.

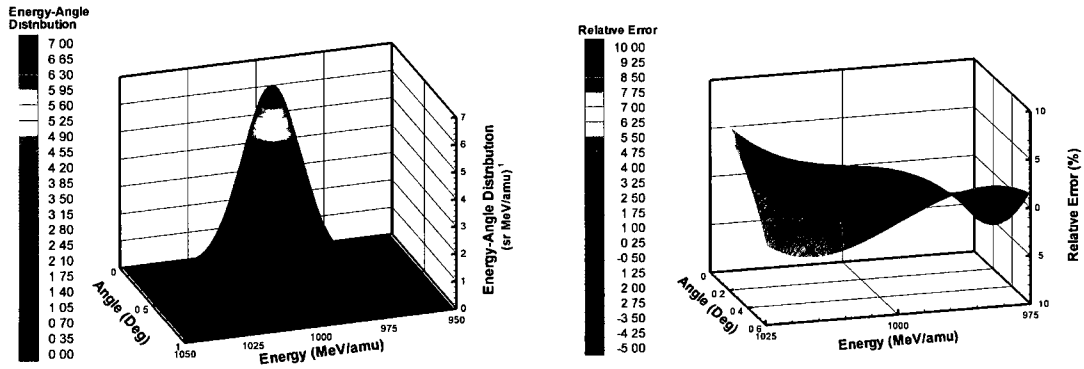

FIGURE 6: The energy-angle distribution and relative error for the ^{40}Ca fragment.

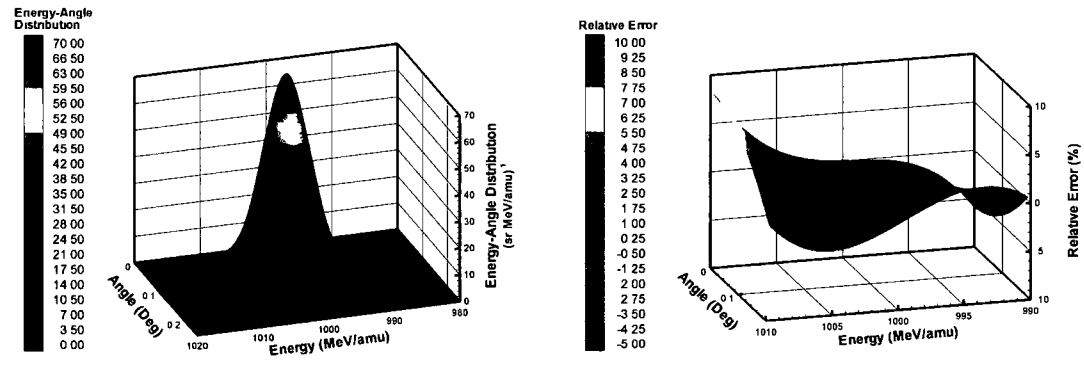

FIGURE 7: The energy-angle distribution and relative error for the ^{54}Mn fragment.

II.2.7 Angular Distribution Results

As shown by these few examples, the angular dispersion of most fragments is small. To investigate this further, integrate the energy-angle distribution over all energies. In doing so, a comparison of the profiles of the angular distribution given by quadrature and the approximate solution that was derived above and was given by equation (45) can be made. In the figures to follow, the projectile was chosen as iron (^{56}Fe), and the target aluminum (^{27}Al). The projectile energy was set to 100, 200, 500, and 1000 MeV/amu respectively. Below are a sample of angular distributions for various fragments. Within these figures, the quadrature solution is represented by a solid line and the approximate solution by circles. It is seen that the dependance on angle is almost negligible for heavy ions. Even for lighter ions such as lithium (^{7}Li), the angular dependance is still extremely small. Since the cross section model presented here was intended for use with heavy ions, the results for light ions are not as accurate. Therefore, the results will be broken up into two sections, light and heavy ions. For the light ions, hydrogen (^{1}H) and helium (^{4}He) will be the ions under investigation, and the heavy ions will range from oxygen (^{7}Li) to calcium (^{40}Ca).

Additionally, an l^2-norm analysis can be done which compares the angular distribution given by quadrature, in which a simple trapezoidal method was used, and the approximate solution that was derived above and was given by equation (45). In the table and plot of the l^2-norm to follow, the deviation is shown for within four standard deviations of the peak value of theta (Deg). Some global patterns are seen from looking at the comparison between the actual solution and the approximate solution. One such pattern is that the models agree close to this peak value, which is important since the mean value theorem will be used in the calculation of the Green's functions. Another is that the error between the solutions decrease with increased projectile energy and also with increased ion mass.

Light Ion Results

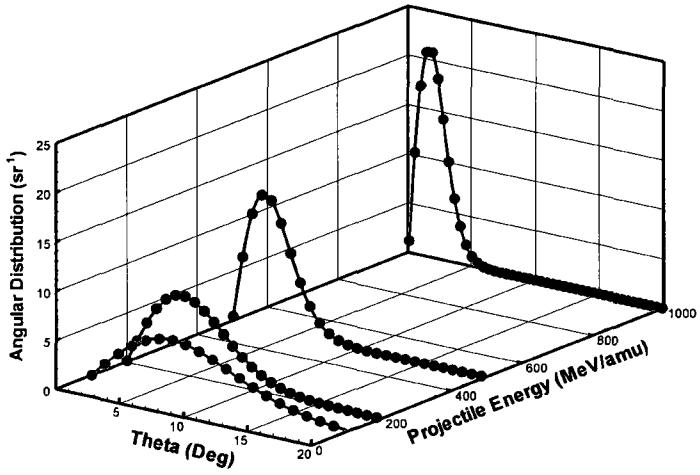

FIGURE 8: A comparison of the quadrature and approximate angular distributions for a ^{1}H fragment.

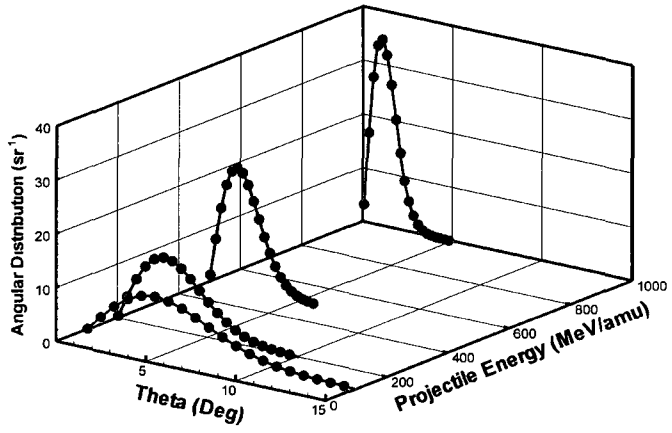

FIGURE 9: A comparison of the quadrature and approximate angular distributions for a ^{4}He fragment.

Heavy Ion Results

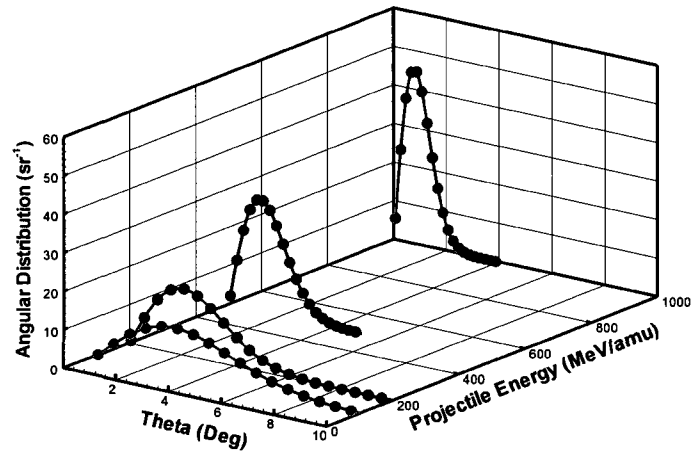

FIGURE 10: A comparison of the quadrature and approximate angular distributions for a ^{7}Li fragment.

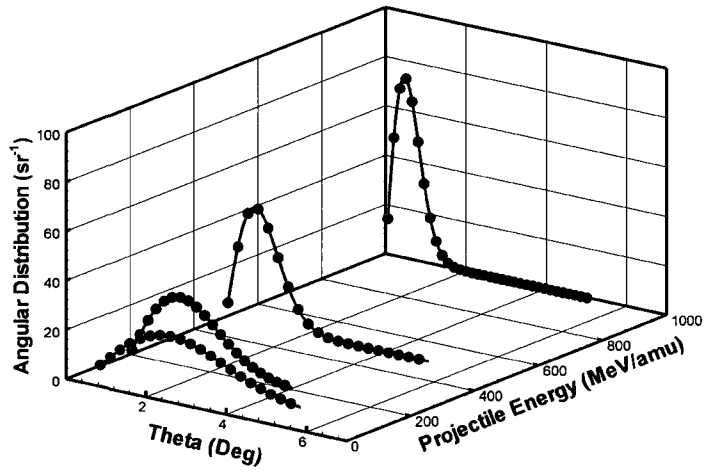

FIGURE 11: A comparison of the quadrature and approximate angular distributions for a ^{16}O fragment.

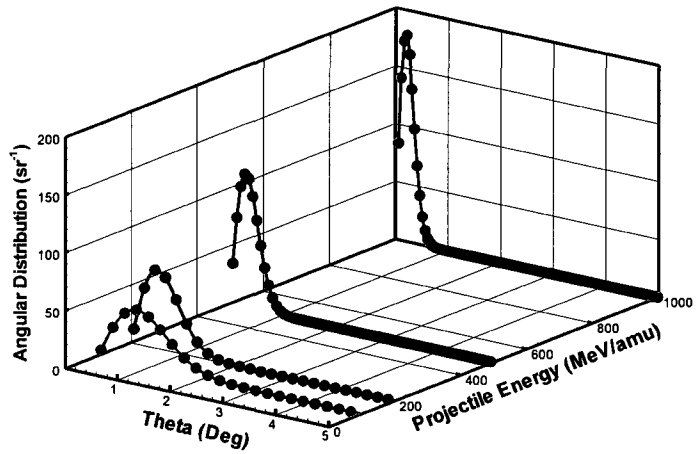

FIGURE 12: A comparison of the quadrature and approximate angular distributions for a ^{40}Ca fragment.

TABLE 1: l^2-norm for Angular Distribution within 4 standard deviations from the peak.

	100 MeV/amu	200 MeV/amu	500 MeV/amu	1000 MeV/amu
hydrogen	4.387101	3.352962	2.883836	2.680961
helium	2.093263	1.509884	1.376305	1.45613
lithium	1.396938	1.002645	0.9325769	1.053180
oxygen	0.6760730	0.4943160	0.4303575	0.5256240
calcium	0.2723932	0.1974676	0.5770772	0.3615175

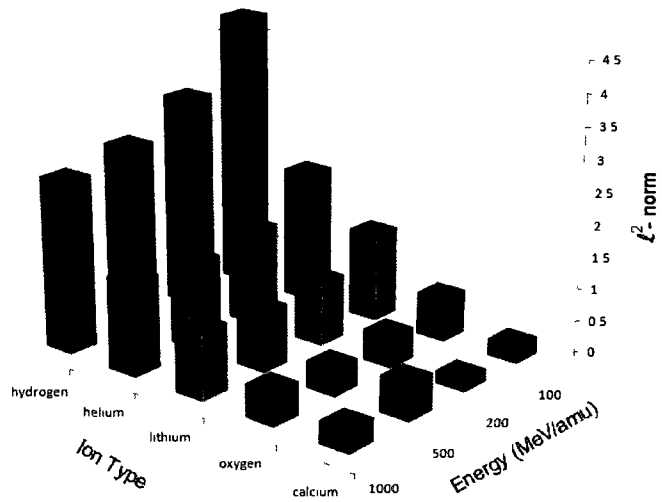

FIGURE 13: l^2-norm for angular distribution

II.2.8 Energy Distribution Results

Next, for the energy distribution a comparison is made between the **exact solution given by equation (19)** and the **approximate solution that was given by equation (45)**. Much like the angular distribution, the models agree close to the mean value of energy, which is important since the mean value theorem will be used in the calculation of the Green's functions.

Again, it is seen that the cross section model does much better for heavy ions than for light ions. This is to be expected since this model was designed to represent heavy ions. Therefore, the results will be broken up into two sections, light and heavy ions. For the light ions, hydrogen (^{1}H) and helium (^{4}He) will be the ions under investigation, and the heavy ions will range from lithium (^{7}Li) to manganese (^{40}Ca).

Light Ion Results

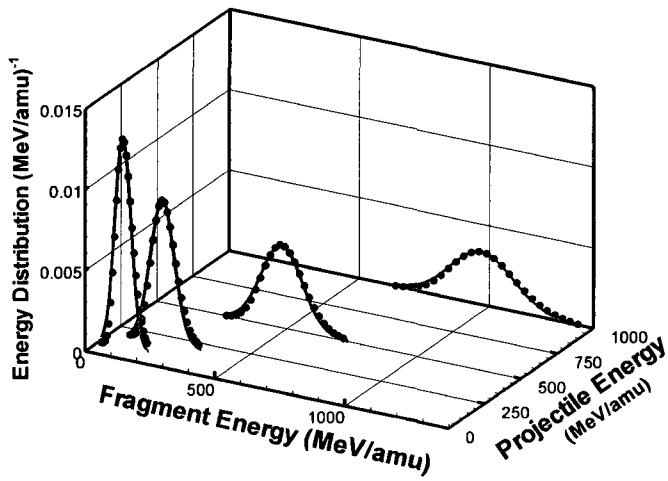

FIGURE 14: A comparison of the quadrature and approximate energy distributions for a ^{1}H fragment.

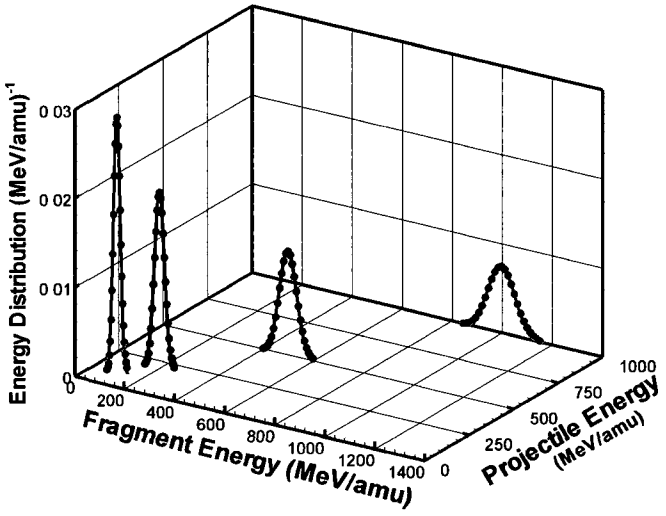

FIGURE 15: A comparison of the quadrature and approximate energy distributions for a ^{4}He projectile.

Heavy Ion Results

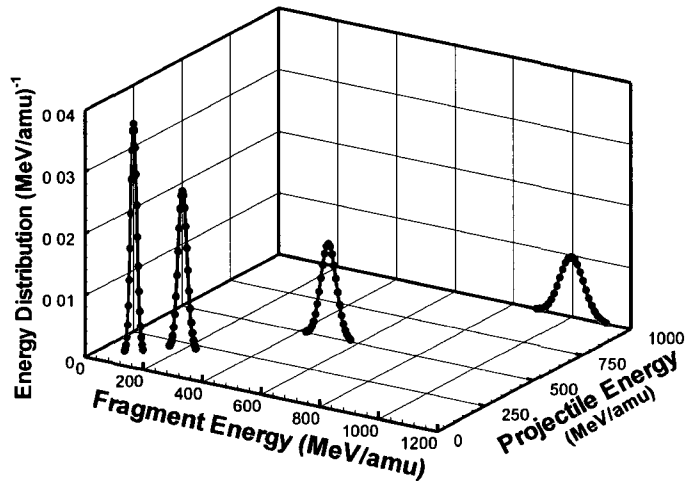

FIGURE 16: A comparison of the quadrature and approximate energy distributions for a ^{7}Li fragment.

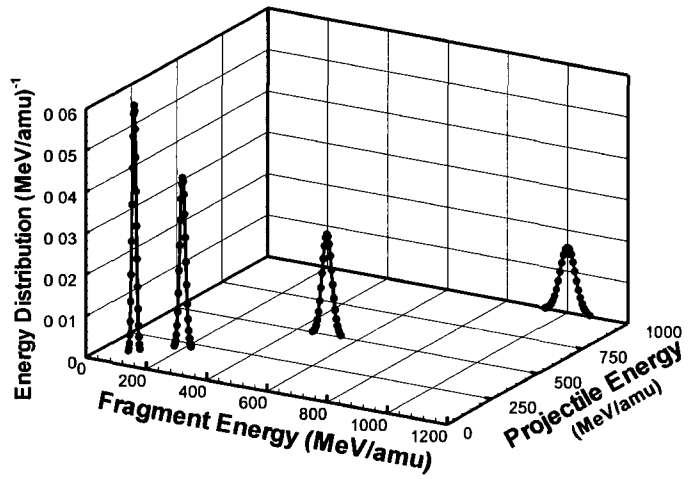

FIGURE 17: A comparison of the quadrature and approximate energy distributions for a ^{16}O fragment.

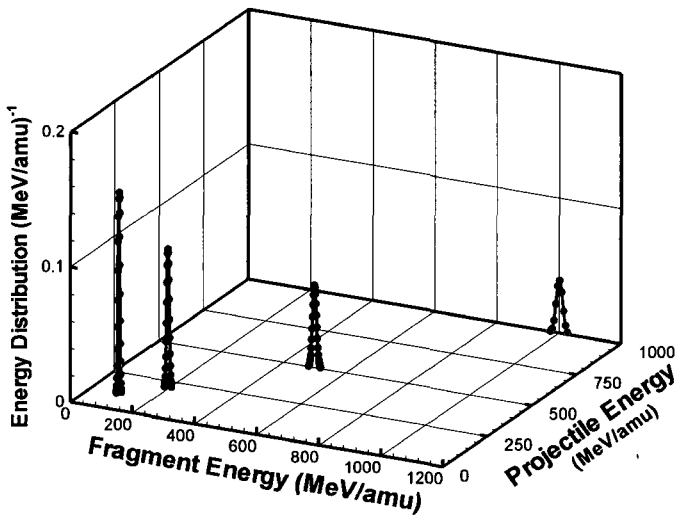

FIGURE 18: A comparison of the quadrature and approximate energy distributions for a ^{40}Ca fragment.

TABLE 2: l^2-norm for Energy Distribution within 4 standard deviations from the peak.

	100 MeV/amu	200 MeV/amu	500 MeV/amu	1000 MeV/amu
hydrogen	0.5319283	0.3412279	0.2491248	0.1849772
helium	0.5146056	0.3346367	0.2458804	0.1832830
lithium	0.5134768	0.3341933	0.2456591	0.1831664
oxygen	0.5119103	0.3335745	0.2453493	0.1830029
calcium	0.5111704	0.3332763	0.2451970	0.1829206

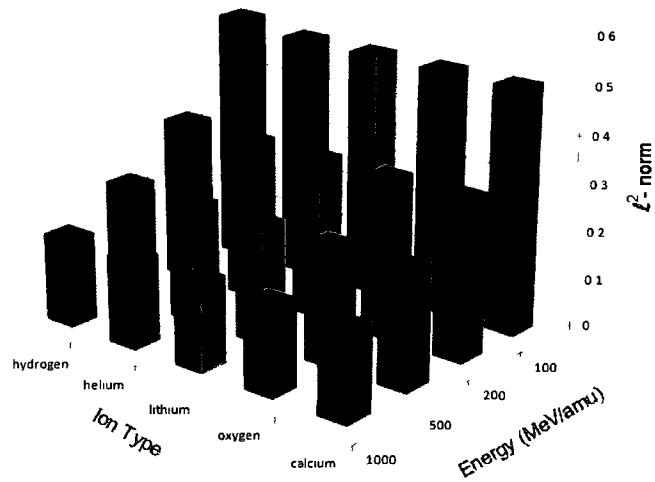

FIGURE 19: l^2-norm for energy distribution

Based on the above figures and tables, our approximation for both the angle and energy distributions are accurate to within a few standard deviations. The approximations do better with heavy ions and with higher energies, but also are fairly accurate for light ions and lower energies. This is expected because the original model was not intended for light ions, and therefore the approximations can only be as accurate as the accuracy of the original model. Overall, the results are good and can now be used to approximate the energy-angle distribution that appears in the calculation of the first and higher order Green's function.

CHAPTER III

THREE DIMENSIONAL TRANSPORT THEORY

III.1 TRANSPORT THEORY

Consideration is given to the transport of high charge and energy (HZE) ions through a three-dimensional convex region V, that is bounded by a smooth surface ∂V, and is filled with a target material. As shown in figure 20, $\mathbf{x}$ and $\mathbf{x}_b$ are the position vectors of arbitrary points in V and ∂V respectively, $\mathbf{n}(\mathbf{x}_b)$ is the unit outward normal at $\mathbf{x}_b$, and $\mathbf{\Omega}$ is an arbitrary unit vector at $\mathbf{x}$.

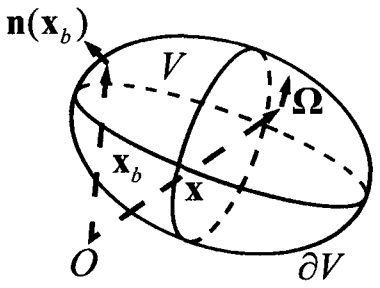

FIGURE 20: Target Material

According to Wilson [26], the transport process of HZE ions through matter is governed by the continuous slowing down, linear Boltzmann equation

$$\begin{aligned}&[\mathbf{\Omega}\cdot\nabla-\partial_E\tilde{S}_j(E)+\sigma_j(E)]\phi_j(\mathbf{x},\mathbf{\Omega},E)\\ &=\sum_{k>j}^{N}\int_E^\infty\int_{4\pi}\sigma_{jk}(\mathbf{\Omega},\mathbf{\Omega}',E,E')\phi_k(\mathbf{x},\mathbf{\Omega}',E')d\mathbf{\Omega}'dE',\end{aligned}\tag{52}$$

with a boundary condition of the form

$$\phi_j(\mathbf{x}_b,\mathbf{\Omega},E)=F_j(\mathbf{x}_b,\mathbf{\Omega},E),\tag{53}$$

where $\mathbf{x}_b$ is a point on the boundary, and N is the number of ions being transported. On the left hand side of equation (52), the notation used in the integral of $\mathbf{\Omega}'$ refers to an integration over all angles. In equation (53), and throughout the rest of this dissertation, it is assumed that all particles arriving at the boundary from points external to V are directed inward toward the volume. In equations (52) and (53), $F_j(\mathbf{x}_b,\mathbf{\Omega},E)$ is a prescribed function, $\phi_k(\mathbf{x},\mathbf{\Omega},E)$ is the flux of type k ions with atomic mass A_k at position $\mathbf{x}$ moving in the direction $\mathbf{\Omega}$ with kinetic energy E, $\sigma_j(E)$

is the macroscopic absorption cross-section, $\tilde{S}_j(E)$ is the ion stopping power, and $\sigma_{jk}(\mathbf{\Omega}, \mathbf{\Omega}', E, E')$ is the double differential production cross section for interactions in which type j ions with energy E and direction $\mathbf{\Omega}$ are produced by type k ions with energy E' and direction $\mathbf{\Omega}'$. Throughout this dissertation, the units of energy will be expressed in MeV/amu, and units of depth in g/cm^2. The latter is obtained by multiplying the linear depth in cm by the material's volumetric density in g/cm^3. Unless otherwise stated, all energies are kinetic.

In order to construct the solution of equation (52), it will be helpful to introduce the continuous slowing down range for a type j ion of energy E

$$R_j(E) = \int_0^E \frac{dH}{\tilde{S}_j(H)}, \tag{54}$$

the function

$$\hat{E}_j = \hat{E}_j(d, E) = R_j^{-1}[R_j(E) - d], \tag{55}$$

may be interpreted as the mean energy at depth d of a j type ion that entered the material with energy E, and its inverse

$$\bar{E}_j = \bar{E}_j(d, E) = R_j^{-1}[R_j(E) + d], \tag{56}$$

which represents the energy on entry, of a j type ion that has residual energy E after penetrating the transport material to a depth d. Also, from equations (54) and (55)

$$\partial_E R_j(\hat{E}_j) = \partial_E[R_j(E) - d], \tag{57}$$

which implies that

$$[S_j(\hat{E}_j)]^{-1}\partial_E \hat{E}_j = [S_j(E_j)]^{-1}, \tag{58}$$

and hence that

$$\partial_E \hat{E}_j(d, E) = \frac{S_j(\hat{E}_j)}{S_j(E)}. \tag{59}$$

Similarly,

$$\partial_E \bar{E}_j(d, E) = \frac{S_j(\bar{E}_j)}{S_j(E)}. \tag{60}$$

In order to solve the Boltzmann Equation, the following definition will be made,

$$Q_j(\mathbf{x},\mathbf{\Omega},E)=\sum_{k>j}\int_E^\infty\int_{4\pi}\sigma_{jk}(\mathbf{\Omega},\mathbf{\Omega}',E,E')\phi_k(\mathbf{x},\mathbf{\Omega}',E')d\mathbf{\Omega}'dE'. \tag{61}$$

With this definition, the Boltzmann Equation can be written as

$$\mathbf{\Omega}\cdot\nabla\phi_j(\mathbf{x},\mathbf{\Omega},E)-\partial_E\{\tilde{S}_j(E)\phi_j(\mathbf{x},\mathbf{\Omega},E)\}+\sigma_j(E)\phi_j(\mathbf{x},\mathbf{\Omega},E)=Q_j(\mathbf{x},\mathbf{\Omega},E), \tag{62}$$

and is subject to the boundary condition (53).

A further simplification can be made by introducing the scaled functions

$$\Psi_j(\mathbf{x},\mathbf{\Omega},E)=\tilde{S}_j(E)\Phi_j(\mathbf{x},\mathbf{\Omega},E), \tag{63}$$

$$\tilde{F}_j(\mathbf{x},\mathbf{\Omega},E)=\tilde{S}_j(E)F_j(\mathbf{x},\mathbf{\Omega},E), \tag{64}$$

and

$$\tilde{Q}_j(\mathbf{x},\mathbf{\Omega},E)=\tilde{S}_j(E)Q_j(\mathbf{x},\mathbf{\Omega},E). \tag{65}$$

Using these functions, the Boltzmann Equation can be written as

$$[\mathbf{\Omega}\cdot\nabla-\tilde{S}_j(E)\frac{\partial}{\partial E}+\sigma_j(E)]\Psi_j(\mathbf{x},\mathbf{\Omega},E)=\tilde{Q}_j(\mathbf{x},\mathbf{\Omega},E), \tag{66}$$

with the boundary condition

$$\Psi_j(\mathbf{x_b},\mathbf{\Omega},E)=\tilde{F}_j(\mathbf{x_b},\mathbf{\Omega},E). \tag{67}$$

With the variables previously presented, a representation for the distance traveled into the material can be obtained. In this regard, let the ray through $\mathbf{x}$ in the direction $\mathbf{\Omega}$, enter V at the point $\mathbf{x}'$ and leave at the point $\mathbf{x}_1'$. Define $\rho=\mathbf{x}\cdot\mathbf{\Omega}$, $\rho'=\mathbf{x}'\cdot\mathbf{\Omega}$, $\rho_1'=\mathbf{x}_1'\cdot\mathbf{\Omega}$, and $\mathbf{x}_n=\mathbf{x}-\rho\mathbf{\Omega}$. Then $\mathbf{x}'=\mathbf{x}_n+\rho'\mathbf{\Omega}$, $\mathbf{x}_1'=\mathbf{x}_n+\rho_1'\mathbf{\Omega}$, $\Psi_j(\mathbf{x},\mathbf{\Omega},E)=\Psi_j(\mathbf{x}_n+\rho\mathbf{\Omega},\mathbf{\Omega},E)$, and $\mathbf{\Omega}\cdot\nabla\Psi_j(\mathbf{x},\mathbf{\Omega},E)=\partial_\rho(\mathbf{x},\mathbf{\Omega},E)\Psi_j(\mathbf{x},\mathbf{\Omega},E)$.

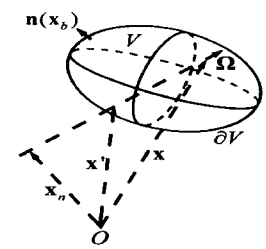

FIGURE 21: Direction of Projectile

In addition, since equation (54) implies that

$$\begin{aligned}\frac{\partial \Psi_j}{\partial E} &= \frac{\partial \Psi_j}{\partial R_j}\frac{\partial R_j}{\partial E} \\ &= \frac{1}{\tilde{S}_j(E)}\frac{\partial \Psi_j}{\partial R_j},\end{aligned}$$

it is now clear that the Boltzmann Equation can be expressed as

$$[\partial_\rho - \partial_{R_j} + \sigma_j(E)]\Psi_j(\mathbf{x}_n + \rho\mathbf{\Omega}, \mathbf{\Omega}, E) = \tilde{Q}_j(\mathbf{x}_n + \rho\mathbf{\Omega}, \mathbf{\Omega}, E), \tag{68}$$

where $\rho' < \rho < \rho_1'$, and is subject to the boundary condition

$$\Psi_j(\mathbf{x}_n + \rho'\mathbf{\Omega}, \mathbf{\Omega}, E) = \tilde{F}_j(\mathbf{x}_n + \rho'\mathbf{\Omega}, \mathbf{\Omega}, E). \tag{69}$$

Following Wilson [26], a convenient reformulation of the problem is obtained by using the method of characteristics, where the characteristic coordinates

$$\eta_j = \rho - R_j(E), \xi_j = \rho + R_j(E), \tag{70}$$

or equivalently

$$\rho = \frac{1}{2}(\xi_j + \eta_j), R_j(E) = \frac{1}{2}(\xi_j - \eta_j), \tag{71}$$

are introduced.

Under this transformation, the lines $E = 0$ and $\rho = \rho'$ in the ρE-plane map to the lines $\xi_j = \eta_j$, and $\xi_j = 2\rho' - \eta_j$ in the $\eta_j\xi_j$-plane respectively(see figures 22 and 23). Also, if Γ is the characteristic curve whose equation is $\rho + R_j(E) = \xi_j = c$, where c is an arbitrary constant, then Γ meets the boundary ∂V at the point $A(\eta_j', \xi_j) = A(\rho', \bar{E}_j)$ whose coordinates may be determined by noting that at A, $\eta_j' = \rho' - R_j(\bar{E}_j)$ and $\xi_j = \rho' + R_j(\bar{E}_j) = \rho + R_j(E)$. Therefore, $R_j(\bar{E}_j) = \xi_j - \rho' = R_j(E) + \rho - \rho'$ and thus,

$$\bar{E}_j = R_j^{-1}[R_j(E) + \rho - \rho']. \tag{72}$$

By defining the variables

$$\chi_j(\eta_j, \xi_j, \mathbf{x}_n, \mathbf{\Omega}) = \Psi_j(\mathbf{x}_n + \rho\mathbf{\Omega}, \mathbf{\Omega}, E), \tag{73}$$

$$\sigma_j(\eta_j, \xi_j) = \sigma_j(E) = \sigma_j(R_j^{-1}(\frac{1}{2}(\xi_j + \eta_j))), \tag{74}$$

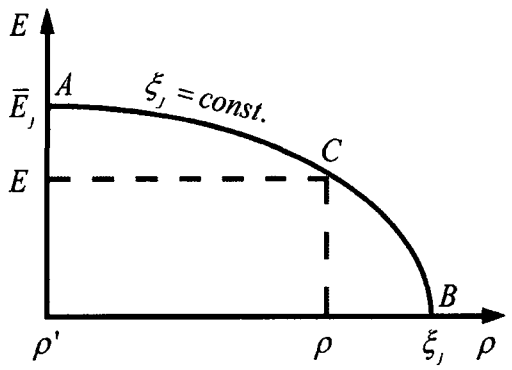

FIGURE 22: Distance vs Energy

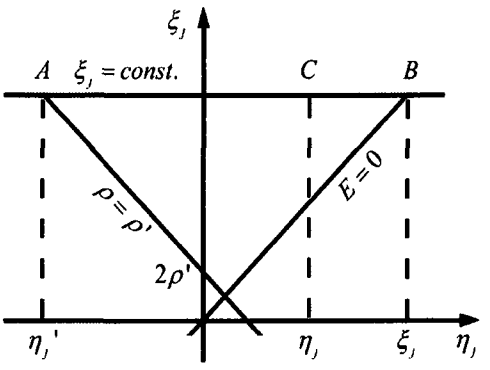

FIGURE 23: New Coordinate System

$$q_j(\eta_j, \xi_j, \mathbf{x}_n, \mathbf{\Omega}) = \tilde{Q}_j(\mathbf{x}_n + \rho\mathbf{\Omega}, \mathbf{\Omega}, E), \tag{75}$$

and noting that

$$\frac{\partial}{\partial \rho} = \frac{\partial}{\partial \xi_j} + \frac{\partial}{\partial \eta_j} \tag{76}$$

$$\frac{\partial}{\partial R_j} = \frac{\partial}{\partial \xi_j} - \frac{\partial}{\partial \eta_j}, \tag{77}$$

the Boltzmann equation (68) can be reduced to a first order linear ordinary differential equation,

$$\frac{\partial}{\partial \eta_j}\chi_j(\eta_j, \xi_j, \mathbf{x}_n, \mathbf{\Omega}) + \frac{1}{2}\sigma_j(\eta_j, \xi_j)\chi_j(\eta_j, \xi_j, \mathbf{x}_n, \mathbf{\Omega}) = \frac{1}{2}q_j(\eta_j, \xi_j, \mathbf{x}_n, \mathbf{\Omega}), \tag{78}$$

along the characteristic curve Γ, with the boundary condition

$$\chi_j(\eta_j', \xi_j, \mathbf{x}_n, \mathbf{\Omega}) = \tilde{F}_j(\mathbf{x}_n + \rho'\mathbf{\Omega}, \mathbf{\Omega}, \bar{E}_j). \tag{79}$$

Since equation (78) has the integrating factor

$$\mu_j(\eta_j, \xi_j) = \exp\left[\int_{\eta_j'}^{\eta_j} \frac{1}{2}\sigma_j(\eta_j'', \xi_j)d\eta_j''\right], \tag{80}$$

its solution can be obtained in the usual way and is given by

$$\chi_g(\eta_g, \xi_g, \mathbf{x}_n, \mathbf{\Omega}) = \frac{\tilde{F}_g(\mathbf{x}_n + \rho'\mathbf{\Omega}, \mathbf{\Omega}, \bar{E}_g)}{\mu_g(\eta_g, \xi_g)} + \frac{1}{2}\int_{\eta'_g}^{\eta_g} \frac{\mu_g(\eta''_g, \xi_g)}{\mu_g(\eta_g, \xi_g)} q_g(\eta''_g, \xi_g, \mathbf{x}_n, \mathbf{\Omega}) d\eta''_g. \quad (81)$$

On reverting to the original variables, it is not difficult to show that the integrating factor can be expressed in the form

$$\mu_g(\eta_g, \xi_g) = \frac{P_g(E)}{P_g(\bar{E}_g)} = \frac{P_g(E)}{P_g(R_g^{-1}[R_g(E) + \rho - \rho'])}, \quad (82)$$

where $P_g(E)$ is the nuclear survival probability, and is defined as

$$P_g(E) = \exp\left(-\int_0^E \frac{\sigma_g(H)}{\tilde{S}_g(H)} dH\right). \quad (83)$$

Next, the integral that occurs in the solution to the ordinary differential equation will need to be evaluated. For convenience, the integral will be defined as I, and is given by

$$I = \frac{1}{2}\int_{\eta'_g}^{\eta_g} \frac{\mu_g(\eta''_g, \xi_g)}{\mu_g(\eta_g, \xi_g)} q_g(\eta''_g, \xi_g, \mathbf{x}_n, \mathbf{\Omega}) d\eta''_g, \quad (84)$$

where

$$\mu_g(\eta''_g, \xi_g) = \frac{P_g(E'')}{P_g(R_g^{-1}[R_g(E'') + \rho'' - \rho'])}. \quad (85)$$

Since

$$\eta''_g = \rho'' - R_g(E''), \quad (86)$$

and

$$\xi_g = \rho'' + R_g(E'') = \rho + R_g(E), \quad (87)$$

it follows that

$$\begin{aligned} R_g(E'') + \rho'' - \rho' &= \xi_g - \rho' \\ &= R_g(E) + \rho - \rho', \end{aligned} \quad (88)$$

and hence that

$$\mu_g(\eta''_g, \xi_g) = \frac{P_g(E'')}{P_g(\bar{E}_g)}. \quad (89)$$

The integral I can therefore be written as

$$I = \int_E^{\bar{E}_j} \frac{P_j(E'')}{P_j(E)} Q_j(\mathbf{x} + \rho''\mathbf{\Omega}, \mathbf{\Omega}, E'')dE''. \tag{90}$$

Also, since $\mathbf{x} = \mathbf{x}_n + \rho\mathbf{\Omega}$, equation (87) implies that

$$\begin{aligned} \mathbf{x}''_\mathbf{n} + \rho''\mathbf{\Omega} &= \mathbf{x_n} + [\rho + R_j(E) - R_j(E'')]\mathbf{\Omega} \\ &= \mathbf{x} + [R_j(E) - R_j(E'')]\mathbf{\Omega}, \end{aligned} \tag{91}$$

and hence that

$$I = \int_E^{\bar{E}_j} \frac{P_j(E'')}{P_j(E)} Q_j(\mathbf{x} + [R_j(E) - R_j(E'')]\mathbf{\Omega}, \mathbf{\Omega}, E'')dE''. \tag{92}$$

Additionally, since

$$\rho'' = \rho + R_j(E) - R_j(E''), \tag{93}$$

and

$$d\rho'' = -\frac{dE''}{\tilde{S}_j(E'')}, \tag{94}$$

the integral (90) can be written in the alternative form

$$I = \int_{\rho'}^{\rho} \frac{P_j(E'')}{P_j(E)} \tilde{Q}_j(\mathbf{x}_n + \rho''\mathbf{\Omega}, \mathbf{\Omega}, E'')d\rho'', \tag{95}$$

where

$$E'' = \bar{E}_j(\rho - \rho'', E) = R_j^{-1}[R_j(E) + \rho - \rho'']. \tag{96}$$

Now, the Boltzmann equation, (81), can be expressed in the form

$$\begin{aligned} \Psi_j(\mathbf{x}_n + \rho''\mathbf{\Omega}, \mathbf{\Omega}, E) &= \frac{P_j(\bar{E}_j)}{P_j(E)} \tilde{F}_j(\mathbf{x}_n + \rho'\mathbf{\Omega}, \mathbf{\Omega}, \bar{E}_j) + \int_E^{\bar{E}_j} \frac{P_j(E'')}{P_j(E)} \\ &\quad \cdot Q_j(\mathbf{x} + [R_j(E) - R_j(E'')]\mathbf{\Omega}, \mathbf{\Omega}, E'')dE'', \end{aligned} \tag{97}$$

or equivalently, as

$$\phi_j(\mathbf{x},\mathbf{\Omega},E) = \frac{P_j(\bar{E}_j)}{P_j(E)}\frac{\tilde{S}_j(\bar{E}_j)}{\tilde{S}_j(E)}F_j(\mathbf{x}'(\mathbf{x},\mathbf{\Omega}),\mathbf{\Omega},\bar{E}_j) + \int_E^{\bar{E}_j}\frac{P_j(E'')}{P_j(E)\tilde{S}_j(E)}Q_j(\mathbf{x}+[R_j(E)-R_j(E'')]\mathbf{\Omega},\mathbf{\Omega},E'')dE'', \quad (98)$$

or, in the alternative form as

$$\phi_j(\mathbf{x},\mathbf{\Omega},E) = \frac{P_j(\bar{E}_j)}{P_j(E)}\frac{\tilde{S}_j(\bar{E}_j)}{\tilde{S}_j(E)}F_j(\mathbf{x}'(\mathbf{x},\mathbf{\Omega}),\mathbf{\Omega},\bar{E}_j) + \int_{\rho'}^{\rho}\frac{P_j(E'')\tilde{S}_j(E'')}{P_j(E)\tilde{S}_j(E)}Q_j(\mathbf{x}_n+\rho''\mathbf{\Omega},\mathbf{\Omega},E'')d\rho''. \quad (99)$$

It should now be recalled that the function $Q_j(\mathbf{x},\mathbf{\Omega},E)$ is related to the particle flux $\phi_k(\mathbf{x},\mathbf{\Omega}',E')$ through its definition as provided by equation (61). Therefore, substitution of this result into equation (98) yields the Transport Integral Equation

$$\phi_j(\mathbf{x},\mathbf{\Omega},E) = \frac{P_j(\bar{E}_j)}{P_j(E)}\frac{\tilde{S}_j(\bar{E}_j)}{\tilde{S}_j(E)}F_j(\mathbf{x}'(\mathbf{x},\mathbf{\Omega}),\mathbf{\Omega},\bar{E}_j) + \sum_{k>j}^{N}\int_E^{\bar{E}_j}\frac{P_j(E'')dE''}{P_j(E)\tilde{S}_j(E)}\int_{E''}^{\infty}dE' \cdot\int_{4\pi}d\mathbf{\Omega}'\sigma_{jk}(\mathbf{\Omega},\mathbf{\Omega}',E'',E')\phi_k(\mathbf{x}+[R_j(E)-R_j(E'')]\mathbf{\Omega},\mathbf{\Omega}',E'), \quad (100)$$

where $\bar{E}_j$ and E'' are defined by equations (56) and (96) respectively.

An alternative form of the transport integral equation is obtained by substituting (61) into (99) and is given by

$$\phi_j(\mathbf{x},\mathbf{\Omega},E) = \frac{P_j(\bar{E}_j)}{P_j(E)}\frac{\tilde{S}_j(\bar{E}_j)}{\tilde{S}_j(E)}F_j(\mathbf{x}'(\mathbf{x},\mathbf{\Omega}),\mathbf{\Omega},\bar{E}_j) + \sum_{k>j}^{N}\int_{\rho'}^{\rho}\frac{P_j(E'')\tilde{S}_j(E'')d\rho''}{P_j(E)\tilde{S}_j(E)}\int_{E''}^{\infty}dE' \cdot\int_{4\pi}d\mathbf{\Omega}'\sigma_{jk}(\mathbf{\Omega},\mathbf{\Omega}',E'',E')\phi_k(\mathbf{x}_n+\rho''\mathbf{\Omega},\mathbf{\Omega}',E'). \quad (101)$$

It should be noted that the integral equations (100) and (101) are of the Volterra type and can therefore be solved by the Neumann series method. A Volterra type equation is one that involves a function, $\phi_j(\mathbf{x},\mathbf{\Omega},E)$ and integrals (in which one limit is a variable) of that function to be solved for $\phi_j(\mathbf{x},\mathbf{\Omega},E)$.

By introducing the field vector $\mathbf{\Phi}(\mathbf{x},\mathbf{\Omega},E)$, whose components are the type j particle fluxes $\phi_j(\mathbf{x},\mathbf{\Omega},E)$, and the fragmentation or collision operator, $\mathbf{\Xi}$, given by

$$\mathbf{\Xi}\cdot\mathbf{\Phi} = [\sum_k \int \sigma_{jk}(\mathbf{\Omega},\mathbf{\Omega}',E,E')\phi_k(\mathbf{x},\mathbf{\Omega}',E')\mathbf{d\Omega}'dE'], \tag{102}$$

the transport integral equation (101) can be written as

$$\begin{aligned}\phi_j(\mathbf{x},\mathbf{\Omega},E) &= \frac{P_j(\bar{E}_j)}{P_j(E)}\frac{\tilde{S}_j(\bar{E}_j)}{\tilde{S}_j(E)}F_j(\mathbf{x}'(\mathbf{x},\mathbf{\Omega}),\mathbf{\Omega},\bar{E}_j) \\ &+ \int_{\rho'}^{\rho}\frac{P_j(E'')\tilde{S}_j(E'')}{P_j(E)\tilde{S}_j(E)} \\ &\cdot [\mathbf{\Xi}\cdot\mathbf{\Phi}]_j(\mathbf{x}'',\mathbf{\Omega},E'')d\rho'',\end{aligned} \tag{103}$$

where $\mathbf{x}'' = \mathbf{x}_n + \rho''\mathbf{\Omega}$.

III.2 THE GREEN'S FUNCTION

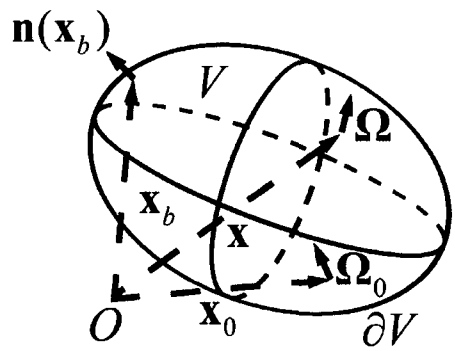

FIGURE 24: Transport Through the Volume

When a mono-energetic beam of type m particles with an energy of E_0 and moving in the direction $\mathbf{\Omega}_0$, enters the material at the point $\mathbf{x}_0 \in \partial V$, the flux on the boundary will be given by

$$\phi_j(\mathbf{x}_b,\mathbf{\Omega},E) = \frac{\delta_{jm}}{2\pi}\delta(1-\mathbf{\Omega}\cdot\mathbf{\Omega}_0)\delta(E-E_0)\overline{\delta}(\mathbf{x}_b-\mathbf{x}_0), \tag{104}$$

where δ_{jm} is the Kronecker delta function, $\delta(1-\mathbf{\Omega}\cdot\mathbf{\Omega}_0)$ and $\delta(E-E_0)$ are Dirac delta functions, and $\overline{\delta}$ is denoting the surface delta function on ∂V. With this boundary condition, the solution to the Boltzmann Equation is called the Green's function and is denoted by the symbol

$$G_{jm}[\mathbf{x},\mathbf{x}_0,\mathbf{\Omega},\mathbf{\Omega}_0,E,E_0]. \tag{105}$$

The Green's function satisfies the transport integral equation

$$\begin{aligned} G_{jm}[\mathbf{x},\mathbf{x}_0,\mathbf{\Omega},\mathbf{\Omega}_0,E,E_0] &= \frac{P_j(\bar{E}_j)}{P_j(E)}\frac{\tilde{S}_j(\bar{E}_j)}{\tilde{S}_j(E)}\frac{\delta_{jm}}{2\pi}\delta(1-\mathbf{\Omega}\cdot\mathbf{\Omega}_0)\delta(\bar{E}_j-E_0) \\ &\quad\cdot\overline{\delta}(\mathbf{x}'-\mathbf{x}_0)+\sum_{k>j}^{N}\int_{\rho'}^{\rho}\frac{P_j(E'')\tilde{S}_j(E'')d\rho''}{P_j(E)\tilde{S}_j(E)}\int_{E''}^{\infty}dE' \\ &\quad\cdot\int_{4\pi}d\mathbf{\Omega}'\sigma_{jk}(\mathbf{\Omega},\mathbf{\Omega}',E'',E') \\ &\quad\cdot G_{km}[\mathbf{x}_n+\rho''\mathbf{\Omega},\mathbf{x}_0,\mathbf{\Omega}',\mathbf{\Omega}_0,E',E_0]. \end{aligned} \tag{106}$$

Once the Green's function is known, the solution for an arbitrary boundary condition, as in equation (53), can be obtained by the formula

$$\begin{aligned} \phi_j(\mathbf{x},\mathbf{\Omega},E) &= \sum_{k\geq j}^{N}\int_{\partial V}d\mathbf{x}_0\int_{4\pi}d\mathbf{\Omega}_0 \\ &\quad\cdot\int_{E}^{\infty}dE_0G_{jk}[\mathbf{x},\mathbf{x}_0,\mathbf{\Omega},\mathbf{\Omega}_0,E,E_0]F_k(\mathbf{x}_0,\mathbf{\Omega}_0,E_0). \end{aligned} \tag{107}$$

Or, in operator notation,

$$\phi_j(\mathbf{x},\mathbf{\Omega},E)=[\mathbf{G}\cdot\mathbf{F}]_j(\mathbf{x},\mathbf{\Omega},E), \tag{108}$$

where $\mathbf{F}$ is the boundary flux vector whose components are the type j boundary fluxes F_j, and the Green's function operator, $\mathbf{G}$, is defined by

$$\begin{aligned} [\mathbf{G}\cdot\mathbf{\Phi}](\mathbf{x},\mathbf{\Omega},E) &= \sum_{m\geq j}^{N}\int_{\partial V}d\mathbf{x}_0\int_{4\pi}d\mathbf{\Omega}_0 \\ &\quad\cdot\int_{E}^{\infty}dE_0G_{jm}[\mathbf{x},\mathbf{x}_0,\mathbf{\Omega},\mathbf{\Omega}_0,E,E_0]\phi_m(\mathbf{x}_0,\mathbf{\Omega}_0,E_0). \end{aligned} \tag{109}$$

III.3 THE NEUMANN SERIES EXPANSION

Recall that the Green's function satisfies the transport integral equation (106), which is of Volterra type and can therefore be solved by a Neumann series expansion.

The first term in equation (106) is called the zero order Green's function, and is denoted by $G^0_{\jmath m}[\mathbf{x}, \mathbf{x}_0, \mathbf{\Omega}, \mathbf{\Omega}_0, E, E_0]$. It follows that

$$\begin{aligned} G^0_{\jmath m}[\mathbf{x}, \mathbf{x}_0, \mathbf{\Omega}, \mathbf{\Omega}_0, E, E_\jmath] &= \frac{P_\jmath(\bar{E}_\jmath)}{P_\jmath(E)} \frac{\tilde{S}_\jmath(\bar{E}_\jmath)}{\tilde{S}_\jmath(E)} \frac{\delta_{\jmath m}}{2\pi} \delta(\bar{E}_\jmath(\rho - \rho', E) - E_0) \\ &\quad \cdot \bar{\delta}(\mathbf{x}' - \mathbf{x}_0) \delta(1 - \mathbf{\Omega} \cdot \mathbf{\Omega}_0), \end{aligned} \tag{110}$$

where

$$\mathbf{x}' = \mathbf{x}'(\mathbf{x}, \mathbf{\Omega}) = \mathbf{x} - (\rho - \rho')\mathbf{\Omega}. \tag{111}$$

By observing that $E_0 = \bar{E}_\jmath(\rho - \rho', \hat{E}_\jmath(\rho - \rho', E_0))$ and making use of the known result

$$\delta[f(x) - f(x_0)]|f'(x)| = \delta(x - x_0), \tag{112}$$

it is readily shown that the zero order Green's function can also be written in the alternative form

$$\begin{aligned} G^0_{\jmath m}[\mathbf{x}, \mathbf{x}_0, \mathbf{\Omega}, \mathbf{\Omega}_0, E, E_\jmath] &= \frac{P_\jmath(\bar{E}_\jmath)}{P_\jmath(E)} \frac{\delta_{\jmath m}}{2\pi} \delta(1 - \mathbf{\Omega} \cdot \mathbf{\Omega}_0) \\ &\quad \cdot \delta(E - \hat{E}_\jmath(\rho - \rho', E_0)) \bar{\delta}(\mathbf{x}' - \mathbf{x}_0), \end{aligned} \tag{113}$$

which often turns out to be useful.

In operator notation, the zero order Green's operator, $\mathbf{G}^0$, with boundary condition $\mathbf{\Phi}_B$ is represented as

$$\begin{aligned} [\mathbf{G^0} \cdot \mathbf{\Phi}_B]_\jmath(\mathbf{x}, \mathbf{\Omega}, E) &= \sum_{m \geq \jmath}^{N} \int_{\partial V} d\mathbf{x}_0 \int_{4\pi} d\mathbf{\Omega}_0 \int_E^\infty dE_0 G^0_{\jmath m}[\mathbf{x}, \mathbf{x}_0, \mathbf{\Omega}, \mathbf{\Omega}_0, E, E_0] \\ &\quad \cdot \phi_m(\mathbf{x}_0, \mathbf{\Omega}_0, E_0) \\ &= \frac{P_\jmath(\bar{E}_\jmath)}{P_\jmath(E)} \frac{\tilde{S}_\jmath(\bar{E}_\jmath)}{\tilde{S}_\jmath(E)} \phi_\jmath(\mathbf{x}'(\mathbf{x}, \mathbf{\Omega}), \mathbf{\Omega}, \bar{E}_\jmath) \\ &= \frac{P_\jmath(\bar{E}_\jmath)}{P_\jmath(E)} \frac{\tilde{S}_\jmath(\bar{E}_\jmath)}{\tilde{S}_\jmath(E)} F_\jmath(\mathbf{x}'(\mathbf{x}, \mathbf{\Omega}), \mathbf{\Omega}, \bar{E}_\jmath). \end{aligned} \tag{114}$$

For notational convenience, the linear transport function, $l_{jm}[\mathbf{x}, \mathbf{x}'', \mathbf{\Omega}, \mathbf{\Omega}_1, E, E_1]$, and the linear transport operator, $\mathbf{L}$, are introduced as follows:

$$l_{jm}[\mathbf{x}, \mathbf{x}'', \mathbf{\Omega}, \mathbf{\Omega}_1, E, E_1] = \frac{P_j(E'')}{P_j(E)} \frac{\tilde{S}_j(E'')}{\tilde{S}_j(E)} \frac{\delta_{jm}}{2\pi} \delta(1 - \mathbf{\Omega} \cdot \mathbf{\Omega}_1) \delta(E'' - E_1), \quad (115)$$

and

$$\begin{aligned} [\mathbf{L} \cdot \mathbf{f}(\mathbf{\Omega}_1, E_1)]_j(\mathbf{x}, \mathbf{x}'', \mathbf{\Omega}, E) &= \sum_{m \geq j}^{N} \int_{4\pi} d\mathbf{\Omega}_1 \int_E^{\infty} dE_1 \\ &\quad \cdot l_{jm}[\mathbf{x}, \mathbf{x}'', \mathbf{\Omega}, \mathbf{\Omega}_1, E, E_1] f_m(\mathbf{\Omega}_1, E_1) \\ &= \int_{4\pi} d\mathbf{\Omega}_1 \int_E^{\infty} dE_1 l_{jj}[\mathbf{x}, \mathbf{x}'', \mathbf{\Omega}, \mathbf{\Omega}_1, E, E_1] f_j(\mathbf{\Omega}_1, E_1) \\ &= \frac{P_j(E'')}{P_j(E)} \frac{\tilde{S}_j(E'')}{\tilde{S}_j(E)} f_j(\mathbf{\Omega}, E''), \end{aligned} \quad (116)$$

where $\mathbf{x}'' = \mathbf{x}_n + \rho'' \mathbf{\Omega}$ and $\rho' \leq \rho'' < \rho$.

With these results, the transport integral equation, (101), can be written as

$$\begin{aligned} \phi_j(\mathbf{x}, \mathbf{\Omega}, E) &= [\mathbf{G}^0 \cdot \mathbf{\Phi}_B]_j(\mathbf{x}, \mathbf{\Omega}, E) \\ &\quad + \int_{\rho'}^{\rho} [\mathbf{L} \cdot \mathbf{\Xi} \cdot \mathbf{\Phi}]_j(\mathbf{x}, \mathbf{x}'', \mathbf{\Omega}, E'') d\rho'', \end{aligned} \quad (117)$$

or, equivalently, it can be expressed in the operator form as

$$\mathbf{\Phi} = \mathbf{G}^0 \cdot \mathbf{\Phi}_B + \mathbf{Q} \cdot \mathbf{L} \cdot \mathbf{\Xi} \cdot \mathbf{\Phi}, \quad (118)$$

where $\mathbf{Q}$ is the quadrature operator.

Since equation (118) is a Volterra type integral equation, it admits the Neumann series solution [20]

$$\begin{aligned} \mathbf{\Phi} &= [\mathbf{G}^0 + (\mathbf{Q} \cdot \mathbf{L} \cdot \mathbf{\Xi}) \cdot \mathbf{G}^0 + (\mathbf{Q} \cdot \mathbf{L} \cdot \mathbf{\Xi})^2 \cdot \mathbf{G}^0 \\ &\quad + (\mathbf{Q} \cdot \mathbf{L} \cdot \mathbf{\Xi})^3 \cdot \mathbf{G}^0 + ...] \cdot \mathbf{\Phi}_B \\ &= [\mathbf{G}^0 + \mathbf{G}^1 + \mathbf{G}^2 + \mathbf{G}^3 + ...] \cdot \mathbf{\Phi}_B, \end{aligned} \quad (119)$$

where $\mathbf{\Phi}_B$ is the boundary flux vector whose components are the type j boundary fluxes ϕ_j. The Neumann series for the transport integral equation is known to be

convergent under suitable conditions [27] and numerical studies by Wilson et al [26, 28] appear to confirm this for many cases of current physical interest.

The term $\mathbf{G}^n$ for $n = 0, 1, 2, 3, \ldots$ appearing in the expansion is called the n^{th} order Green's operator and is associated with the n^{th} generation of fragments produced. The above formalism lends to the following interpretation of the Neumann series. In the first term, $\mathbf{G}^0 \cdot \mathbf{\Phi}_B$, the operator $\mathbf{G}^0$ propagates primary ions from the boundary to the point $\mathbf{x}$ with the attenuation processes. In the second term, $\mathbf{Q} \cdot \mathbf{L} \cdot \mathbf{\Xi} \cdot \mathbf{G}^0 \cdot \mathbf{\Phi}_B$, the operator $\mathbf{G}^0$ propagates primary ions from the boundary to an interior point $\mathbf{x}''$ where a nuclear event takes place. The term $\mathbf{\Xi} \cdot \mathbf{G}^0 \cdot \mathbf{\Phi}_B$ is the production density of first generation secondaries at position $\mathbf{x}''$. These ions are transported from $\mathbf{x}''$ to $\mathbf{x}$ by the linear transport operator $\mathbf{L}$. Lastly, the quadrature operator, $\mathbf{Q}$, sums up all of the first generation fragments that are produced at interior points and transported to the point $\mathbf{x}$. The remaining terms of the Neumann series may be interpreted in a similar way and, from the series, the n^{th} order Green's operator can be computed recursively for $n \geq 1$ as

$$\mathbf{G}^n = (\mathbf{Q} \cdot \mathbf{L} \cdot \mathbf{\Xi}) \cdot \mathbf{G}^{n-1}. \tag{120}$$

Once the Green's Function is known, the solution of the Boltzmann equation for a more general boundary condition can be obtained by quadrature.

III.4 ENERGY STRAGGLING AND THE ZERO ORDER GREEN'S FUNCTION

Up to this point, the assumption is being made that all particles of an initially mono-energetic beam lose the same amount of energy with depth. However, each particle will lose energy in a sequence of random events, which means that different particles, on penetrating to the same depth, are likely to have lost different amounts of energy. The first order correction of particle energy from the mean at a given depth is called energy straggling, and has been investigated by Payne [29] and by Wilson et al. [30].

The zero order Green's function introduced via equation (110) does not take energy straggling into account since its energy spectrum $\frac{P_m(\bar{E}_m)}{P_m(E)}\delta[E - \hat{E}_m(\rho - \rho', E_0)]$, at depth $(\rho - \rho')$, is a delta function which is attenuated by the factor $\frac{P_m(\bar{E}_m)}{P_m(E)}$ and has support at the mean residual energy $\hat{E}_m(\rho - \rho', E_0)$. To account for straggling, the energy spectrum will be modeled by a Gaussian function whose mean is $\hat{E}_m(\rho - \rho', E_0)$ and whose deviation is the corresponding straggling width $s_m(\rho - \rho', E_0)$ [20].

Incorporating these assumptions into our model will yield a new zero order Green's function

$$\begin{aligned} G^0_{jm}[\mathbf{x},\mathbf{x}_0,\mathbf{\Omega},\mathbf{\Omega}_0,E,E_0] \;\approx\; & \frac{P_m(\bar{E}_m)}{P_j(E)}\frac{\delta_{jm}}{2\pi}\delta(1-\mathbf{\Omega}\cdot\mathbf{\Omega}_0)\bar{\delta}(\mathbf{x}'-\mathbf{x}_0) \\ & \cdot\frac{1}{\sqrt{2\pi}s_m(\rho-\rho',E_0)} \\ & \cdot\exp\left\{\frac{-[E-\hat{E}_m(\rho-\rho',E_0)]^2}{2s_m(\rho-\rho',E_0)^2}\right\}, \end{aligned} \tag{121}$$

where $P_m(E)$ is the survival probability for type m ions of energy E, $\bar{E}_m$ and $\hat{E}_m$ are given by the relationships in (56) and (55) respectively, where $\hat{E}_m$ is the mean energy at depth $(\rho-\rho')$ of a type m ion that entered the transport material with kinetic energy E_0, and $s_m(\rho-\rho',E_0)$ is the corresponding energy straggling width. The linear transport function can be generalized similarly and now takes the form

$$\begin{aligned} l_{jm}[\mathbf{x},\mathbf{x}'',\mathbf{\Omega},\mathbf{\Omega}_1,E,E_1] \;=\; & \frac{P_m(E'')}{P_j(E)}\frac{\delta_{jm}}{2\pi}\frac{\delta(1-\mathbf{\Omega}\cdot\mathbf{\Omega}_1)}{\sqrt{2\pi}s_m(\rho-\rho'',E_1)} \\ & \cdot\exp\left\{\frac{-[E-\hat{E}_m(\rho-\rho'',E_1)]^2}{2s_m(\rho-\rho'',E_1)^2}\right\}. \end{aligned} \tag{122}$$

It should be noted that there are similarities between the previously derived one dimensional zero order Green's function, $G^0_{jm}(\rho,\rho',E,E_0)$ [20] and the three dimensional equation that is derived in this dissertation. Specifically, the three dimensional zero order Green's function can be written in terms of its one dimensional equivalent as

$$G^0_{jm}[\mathbf{x},\mathbf{x}_0,\mathbf{\Omega},\mathbf{\Omega}_0,E,E_0] = \frac{1}{2\pi}\delta(1-\mathbf{\Omega}\cdot\mathbf{\Omega}_0)\bar{\delta}(\mathbf{x}'-\mathbf{x}_0)G^0_{jm}(\rho,\rho',E,E_0), \tag{123}$$

and the linear transport function as

$$l_{jm}[\mathbf{x},\mathbf{x}'',\mathbf{\Omega},\mathbf{\Omega}_1,E,E_1] = \frac{1}{2\pi}\delta(1-\mathbf{\Omega}\cdot\mathbf{\Omega}_1)G^0_{jm}(\rho,\rho'',E,E_1). \tag{124}$$

Now that energy straggling has been incorporated into the zero order Green's function and the linear transport function, the higher order Green's functions can be obtained from the recurrence formula as described earlier by equation (120). Note that at this time, multiple scattering is not incorporated into the formalism.

When the boundary condition takes a more general form, as in equation (53), the primary flux is obtained by integrating the zero order Green's function over all energies and directions within the volume as

$$\begin{aligned}\phi_J^0(\mathbf{x},\mathbf{\Omega},E) &= [\mathbf{G^0}\cdot\mathbf{\Phi_B}]_J(\mathbf{x},\mathbf{\Omega},E)\\ &= \int_{\partial V} d\mathbf{x}_0 \int_{4\pi} d\mathbf{\Omega}_0 \int_E^\infty dE_0\\ &\quad \cdot G^0_{JJ}(\mathbf{x},\mathbf{x}_0,\mathbf{\Omega},\mathbf{\Omega}_0,E,E_0)F_J(\mathbf{x}_0,\mathbf{\Omega}_0,E_0),\end{aligned} \tag{125}$$

which, in general, has to be evaluated numerically. In the accelerator beam model described below, equation (125) can be approximated analytically and a closed form expression may be obtained for the zero order primary flux. The result obtained in this case is called the broad zero order Green's function.

III.5 THE BROAD ZERO ORDER GREEN'S FUNCTION

Since ion beam experiments play an important role in analyzing the shielding requirements in space applications, modeling the propagation of linear accelerator beams through potential shielding materials is of interest. A simple model can be constructed by assuming that the accelerator beam consists of mono-energetic type m particles of energy E_0, that move in the direction $\mathbf{\Omega}_0$, and enter the material at the point $\mathbf{x}_0$ on its boundary. In this case, the boundary condition is given by equation (104), and the solution is the corresponding Green's function. In practice, however, the accelerator beam is neither mono-energetic nor uni-directional, and it enters the material at several points that are clustered about the mean value $\mathbf{x}_0$. A more realistic model can therefore be obtained by assuming that the beam has a Gaussian profile in both angle and energy, and that it enters the material at points that are distributed in a Gaussian manner about the mean point of entry, $\mathbf{x}_0$. In order to accomplish this, it is assumed that the boundary is defined by the single-valued, continuously differentiable parametric equations,

$$\partial V = \{\mathbf{x} : \mathbf{x} = \mathbf{x}(u,v), u_s \le u \le u_f, v_s \le v \le v_f\}. \tag{126}$$

In this case, the element of surface area is given by

$$dS = |\partial_u \mathbf{x} \times \partial_v \mathbf{x}| du dv. \tag{127}$$

Further, at a non-singular point, $\mathbf{x}_0 = \mathbf{x}_0(u_0, v_0)$, of the parametric coordinate system, $|\partial_u \mathbf{x}_0 \times \partial_v \mathbf{x}_0| \neq 0$, and the surface delta function is given by

$$\overline{\delta}(\mathbf{x} - \mathbf{x}_0) = \frac{\delta(u - u_0)\delta(v - v_0)}{|\partial_u \mathbf{x}_0 \times \partial_v \mathbf{x}_0|}. \tag{128}$$

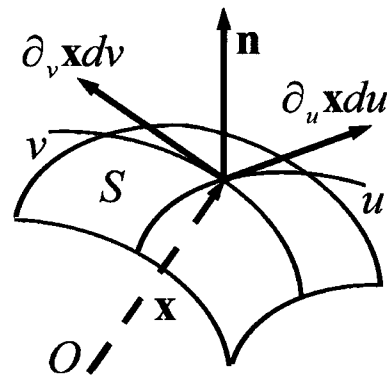

FIGURE 25: Parametric Surface

The boundary condition may then be assumed to take the Gaussian form

$$\begin{aligned} F_j(\mathbf{x}_b, \boldsymbol{\Omega}, E) &= \frac{\delta_{jm} H[-\boldsymbol{\Omega} \cdot \mathbf{n}(\mathbf{x}_b)]}{4\pi s_x^2 s_{\boldsymbol{\Omega}} s_E K_x K_{\boldsymbol{\Omega}} |\partial_u \mathbf{x}_b \times \partial_v \mathbf{x}_b|} \exp\left\{-\frac{(u_b - u_0)^2 + (v_b - v_0)^2}{2s_x^2}\right\} \\ &\quad \cdot \exp\left\{-\frac{(1 - \boldsymbol{\Omega} \cdot \boldsymbol{\Omega}_0)^2}{2s_{\boldsymbol{\Omega}}^2}\right\} \exp\left\{-\frac{(E - E_0)^2}{2s_E^2}\right\}, \end{aligned} \tag{129}$$

where $\mathbf{x}_b = \mathbf{x}_b(u_b, v_b)$, $|\partial_u \mathbf{x}_b \times \partial_v \mathbf{x}_b|$ is the surface Jacobian, $H[x]$ is the Heaviside function, $s_x, s_{\boldsymbol{\Omega}}$, and s_E are the spreads in space, angle and energy respectively, and K_x and $K_{\boldsymbol{\Omega}}$ are normalization constants.

The normalization constants K_x and $K_{\boldsymbol{\Omega}}$ are chosen such that

$$\int_{\partial V} d\mathbf{x}_1 \int_{4\pi} d\boldsymbol{\Omega}_0 \int_E^\infty dE_0 F_j(\mathbf{x}_b, \boldsymbol{\Omega}, E) = 1, \tag{130}$$

in which case

$$\begin{aligned} K_x &= \frac{1}{4}\left[\operatorname{erf}\left(\frac{u_f - u_0}{\sqrt{2}s_x}\right) - \operatorname{erf}\left(\frac{u_s - u_0}{\sqrt{2}s_x}\right)\right] \\ &\quad \cdot \left[\operatorname{erf}\left(\frac{v_f - v_0}{\sqrt{2}s_x}\right) - \operatorname{erf}\left(\frac{v_s - v_0}{\sqrt{2}s_x}\right)\right], \end{aligned} \tag{131}$$

$$K_{\mathbf{\Omega}} = \pi \cdot \mathrm{erf}\left(\frac{\sqrt{2}}{s_{\mathbf{\Omega}}}\right), \tag{132}$$

where erf refers to the error function (see Appendix B for the derivation of the normalization constants). It should be observed that in the limit as $s_x, s_{\mathbf{\Omega}}, s_E \to 0$, the boundary condition (129) reduces to the Green's function boundary condition.

The Green's function, together with the boundary condition given by equation (129), can be used to calculate the primary flux as shown in equation (125).

The primary flux associated with the boundary condition (129) is called the broad zero order Green's function, $G^b_{\jmath m}(\mathbf{x}, \mathbf{x}_0, \mathbf{\Omega}, \mathbf{\Omega}_0, E, E_0)$, and is given by the expression

$$G^b_{\jmath m}(\mathbf{x}, \mathbf{x}_0, \mathbf{\Omega}, \mathbf{\Omega}_0, E, E_0) = [\mathbf{G}^0 \cdot \mathbf{F}]_{\jmath}(\mathbf{x}, \mathbf{\Omega}, E)$$

$$= \sum_{k \geq \jmath}^{N} \int_{\partial V} d\mathbf{x}_1 \int_{4\pi} d\mathbf{\Omega}_1 \int_E^{\infty} dE_1 G^0_{\jmath k}[\mathbf{x}, \mathbf{x}_1, \mathbf{\Omega}, \mathbf{\Omega}_1, E, E_1] \cdot F_k(\mathbf{x}_1, \mathbf{\Omega}_1, E_1)$$

$$\begin{aligned}
= & \sum_{k \geq \jmath}^{N} \delta_{\jmath k} \int_{\partial V} \frac{\delta_{km} \bar{\delta}(\mathbf{x}' - \mathbf{x}_1)}{2\pi s_x^2 K_x |\partial_u \mathbf{x}_1 \times \partial_v \mathbf{x}_1|} \exp\left\{-\frac{(u_1 - u_0)^2 + (v_1 - v_0)^2}{2s_x^2}\right\} d\mathbf{x}_1 \\
& \cdot \int_{4\pi} \frac{\delta(1 - \mathbf{\Omega} \cdot \mathbf{\Omega}_1)}{2\pi} \exp\left\{-\frac{(1 - \mathbf{\Omega}_1 \cdot \mathbf{\Omega}_0)^2}{2s_{\mathbf{\Omega}}^2}\right\} \frac{H[-\mathbf{\Omega}_1 \cdot \mathbf{n}(\mathbf{x}_1)] d\mathbf{\Omega}_1}{\sqrt{2\pi} s_{\mathbf{\Omega}} K_{\mathbf{\Omega}}} \\
& \cdot \int_E^{\infty} \frac{P_k(\bar{E}_k)}{P_k(E)} \exp\left\{-\frac{(E - \hat{E}_k(\rho - \rho', E_1))^2}{2s_k(\rho - \rho', E_1)^2}\right\} \\
& \cdot \exp\left\{-\frac{(E_1 - E_0)^2}{2s_E^2}\right\} \frac{dE_1}{2\pi s_k(\rho - \rho', E_1) s_E} \\
\approx & \frac{\delta_{\jmath m} H[-\mathbf{\Omega} \cdot \mathbf{n}(\mathbf{x}')]}{2\pi\sqrt{2\pi} s_x^2 s_{\mathbf{\Omega}} K_x K_{\mathbf{\Omega}} |\partial_u \mathbf{x}' \times \partial_v \mathbf{x}'|} \exp\left\{-\frac{(u' - u_0)^2 + (v' - v_0)^2}{2s_x^2}\right\} \\
& \cdot \exp\left\{-\frac{(1 - \mathbf{\Omega} \cdot \mathbf{\Omega}_0)^2}{2s_{\mathbf{\Omega}}^2}\right\} \int_E^{\infty} \frac{P_m(\bar{E}_m)}{P_m(E)} \exp\left\{-\frac{(E - \hat{E}_m(\rho - \rho', E_1))^2}{2s_m(\rho - \rho', E_1)^2}\right\} \\
& \cdot \exp\left\{\frac{-(E_1 - E_0)^2}{2s_E^2}\right\} \frac{dE_1}{2\pi s_m(\rho - \rho', E_1) s_E}.
\end{aligned} \tag{133}$$

The integral in equation (133) can be approximated by the mean value theorem and saddle point techniques discussed in [20]. The first approximation is to apply Taylor's Theorem to the mean energy that occurs in equation (133),

$$\hat{E}_m(\rho - \rho', E_1) \approx \hat{E}_m(\rho - \rho', E_0) - [\partial_{E_1} \hat{E}_m(\rho - \rho', E_1)]_{E_0}(E_1 - E_0). \tag{134}$$

Next, let H be the second term of the Taylor expansion, where $H = r(E_1 - E_0)$ and by equation (59)

$$\begin{aligned} r &= [\partial_{E_1} \hat{E}_m(\rho - \rho', E_1)]_{E_0} \\ &= \frac{\tilde{S}_m[\hat{E}_m(\rho - \rho', E_0)]}{\tilde{S}_m[E_0]}. \end{aligned} \tag{135}$$

Therefore, the energy integral in the broad zero order Green's function can be approximated as

$$\begin{aligned} &\int_E^\infty \frac{P_m(\bar{E}_m)}{P_m(E)} \exp\left\{-\frac{(E - \hat{E}_m(\rho - \rho', E_0) - H)^2}{2s_m(\rho - \rho', E_1)^2}\right\} \\ &\cdot \exp\left\{\frac{-H^2}{2r^2 s_E^2}\right\} \frac{dH}{2\pi s_m(\rho - \rho', E_1)(r s_E)} \\ &\approx \frac{P_m(\bar{E}_m)}{P_m(E)} \exp\left\{-\frac{(E - \hat{E}_m(\rho - \rho', E_0))^2}{2s_m^b(\rho - \rho', E_0)^2}\right\} \frac{1}{\sqrt{2\pi} s_m^b(\rho - \rho', E_0)}, \end{aligned} \tag{136}$$

where the energy $\bar{E}$ is given by equation (56) and the broad energy spectral width is

$$s_m^b(\rho - \rho', E_0)^2 = s_m(\rho - \rho', E_0)^2 + \left\{\frac{\tilde{S}_m[\hat{E}_m(\rho - \rho', E_0)]}{\tilde{S}_m[E_0]}\right\}^2 s_E^2. \tag{137}$$

Thus, the broad zero order Green's function can be written as

$$\begin{aligned} G_{jm}^b(\mathbf{x}, \mathbf{x}_0, \mathbf{\Omega}, \mathbf{\Omega}_0, E, E_0) \approx & \frac{\delta_{jm} H[-\mathbf{\Omega} \cdot \mathbf{n}(\mathbf{x}')]}{4\pi s_x^2 s_{\mathbf{\Omega}} s_m^b(\rho - \rho', E_0) K_x K_{\mathbf{\Omega}} |\partial_u \mathbf{x}' \times \partial_v \mathbf{x}'|} \frac{P_m(\bar{E}_m)}{P_m(E)} \\ & \cdot \exp\left\{-\frac{(u' - u_0)^2 + (v' - v_0)^2}{2s_x^2}\right\} \\ & \cdot \exp\left\{-\frac{(1 - \mathbf{\Omega} \cdot \mathbf{\Omega}_0)^2}{2s_{\mathbf{\Omega}}^2}\right\} \\ & \cdot \exp\left\{-\frac{(E - \hat{E}_m(\rho - \rho', E_0))^2}{2s_m^b(\rho - \rho', E_0)^2}\right\}. \end{aligned} \tag{138}$$

We can also represent the broad zero order Green's function in terms of the one dimensional broad zero order Green's function [20] just as we related the energy straggling zero order Green's function to the one dimensional zero order Green's

function as

$$G^b_{jm}(\mathbf{x},\mathbf{x}_0,\mathbf{\Omega},\mathbf{\Omega}_0,E,E_0) = \frac{H[-\mathbf{\Omega}\cdot\mathbf{n}(\mathbf{x}')]}{2\pi s_x^2 K_x|\partial_u\mathbf{x}'\times\partial_v\mathbf{x}'|}\exp\left\{-\frac{(u'-u_0)^2+(v'-v_0)^2}{2s_x^2}\right\}$$
$$\cdot\frac{1}{\sqrt{2\pi}K_{\mathbf{\Omega}}s_{\mathbf{\Omega}}}\exp\left\{-\frac{(1-\mathbf{\Omega}\cdot\mathbf{\Omega}_0)^2}{2s_{\mathbf{\Omega}}^2}\right\}$$
$$\cdot G^b_{jm}(\rho,\rho',E,E_0). \tag{139}$$

It should be observed that in the limit as $s_x, s_{\mathbf{\Omega}}, s_E \rightarrow 0$, the broad zero order Green's function, $G^b_{jm}(\mathbf{x},\mathbf{x}_0,\mathbf{\Omega},\mathbf{\Omega}_0,E,E_0)$, reduces to the zero order Green's function, $G^0_{jm}(\mathbf{x},\mathbf{x}_0,\mathbf{\Omega},\mathbf{\Omega}_0,E,E_0)$.

III.6 INTEGRAL FLUX

For the purpose of illustration, various integral flux calculations will be explored, which will reduce the number of variables. Another reason to take the time to compute the integral forms of the flux is for comparison with earlier theories. We will define the various integral fluxes as

$$\hat{\phi}_j(\mathbf{x},\mathbf{\Omega}) = \int_{-\infty}^{\infty}\phi_j(\mathbf{x},\mathbf{\Omega},E)dE, \tag{140}$$

$$\tilde{\phi}_j(\mathbf{x},E) = \int_{4\pi}\phi_j(\mathbf{x},\mathbf{\Omega},E)d\mathbf{\Omega}, \tag{141}$$

$$\bar{\phi}_j(\mathbf{x}) = \int_{-\infty}^{\infty}\int_{4\pi}\phi_j(\mathbf{x},\mathbf{\Omega},E)d\mathbf{\Omega}dE. \tag{142}$$

Of particular interest are the corresponding integral Green's functions that are discussed below.

Consideration is first given to the energy independent zero order integral Green's

function

$$\begin{aligned}
\hat{G}^b_{jm}(\mathbf{x},\mathbf{x}_0,\mathbf{\Omega},\mathbf{\Omega}_0,E_0) &= \int_{-\infty}^{\infty} G^b_{jm}(\mathbf{x},\mathbf{x}_0,\mathbf{\Omega},\mathbf{\Omega}_0,E,E_0)dE \\
&= \frac{H[-\mathbf{\Omega}\cdot\mathbf{n}(\mathbf{x}')]}{2\pi s_x^2 K_x|\partial_u\mathbf{x}'\times\partial_v\mathbf{x}'|}\exp\left\{-\frac{(u'-u_0)^2+(v'-v_0)^2}{2s_x^2}\right\} \\
&\quad\cdot\frac{1}{\sqrt{2\pi}K_{\mathbf{\Omega}}s_{\mathbf{\Omega}}}\exp\left\{-\frac{(1-\mathbf{\Omega}\cdot\mathbf{\Omega}_0)^2}{2s_{\mathbf{\Omega}}^2}\right\} \\
&\quad\cdot\int_{-\infty}^{\infty} G^b_{jm}(\rho,\rho',E,E_0)dE \\
&\approx \frac{\delta_{jm}H[-\mathbf{\Omega}\cdot\mathbf{n}(\mathbf{x}')]}{2\pi s_x^2 K_x|\partial_u\mathbf{x}'\times\partial_v\mathbf{x}'|}\exp\left\{-\frac{(u'-u_0)^2+(v'-v_0)^2}{2s_x^2}\right\} \\
&\quad\cdot\frac{1}{\sqrt{2\pi}K_{\mathbf{\Omega}}s_{\mathbf{\Omega}}}\exp\left\{-\frac{(1-\mathbf{\Omega}\cdot\mathbf{\Omega}_0)^2}{2s_{\mathbf{\Omega}}^2}\right\} \\
&\quad\cdot\frac{P_m(E_0)}{P_j(\hat{E}_m(\rho-\rho',E_0))}. \qquad (143)
\end{aligned}$$

The angle independent zero order integral Green's function is given by

$$\begin{aligned}
\tilde{G}^b_{jm}(\mathbf{x},\mathbf{x}_0,\mathbf{\Omega}_0,E,E_0) &= \int_{4\pi} G^b_{jm}(\mathbf{x},\mathbf{x}_0,\mathbf{\Omega},\mathbf{\Omega}_0,E,E_0)d\mathbf{\Omega} \\
&= \frac{1}{2\pi s_x^2 K_x|\partial_u\mathbf{x}'\times\partial_v\mathbf{x}'|}\exp\left\{-\frac{(u'-u_0)^2+(v'-v_0)^2}{2s_x^2}\right\} \\
&\quad\cdot\int_{4\pi}\frac{H[-\mathbf{\Omega}\cdot\mathbf{n}(\mathbf{x}')]}{\sqrt{2\pi}K_{\mathbf{\Omega}}s_{\mathbf{\Omega}}}\exp\left\{-\frac{(1-\mathbf{\Omega}\cdot\mathbf{\Omega}_0)^2}{2s_{\mathbf{\Omega}}^2}\right\} \\
&\quad\cdot G^b_{jm}(\rho,\rho',E,E_0)d\mathbf{\Omega} \\
&\approx \frac{H[-\mathbf{\Omega}_0\cdot\mathbf{n}(\mathbf{x}')]}{2\pi s_x^2 K_x|\partial_u\mathbf{x}'\times\partial_v\mathbf{x}'|}\exp\left\{-\frac{(u'-u_0)^2+(v'-v_0)^2}{2s_x^2}\right\} \\
&\quad\cdot G^b_{jm}(\rho,\rho',E,E_0), \qquad (144)
\end{aligned}$$

where $G^b_{jm}(\rho,\rho',E,E_0)$ is the one dimensional broad zero order Green's function [20] and $\mathbf{x}' = \mathbf{x} - (\rho-\rho')\mathbf{\Omega}_0$.

The angle-energy independent zero order integral Green's function is given by

$$\begin{aligned}
\bar{G}^b_{jm}(\mathbf{x},\mathbf{x}_0,\boldsymbol{\Omega}_0,E_0) &= \int_{-\infty}^{\infty}\int_{4\pi} G^b_{jm}(\mathbf{x},\mathbf{x}_0,\boldsymbol{\Omega},\boldsymbol{\Omega}_0,E,E_0)d\boldsymbol{\Omega}dE \\
&\approx \frac{H[-\boldsymbol{\Omega}_0\cdot\mathbf{n}(\mathbf{x}')]}{2\pi s_x^2 K_x|\partial_u\mathbf{x}'\times\partial_v\mathbf{x}'|}\exp\left\{-\frac{(u'-u_0)^2+(v'-v_0)^2}{2s_x^2}\right\} \\
&\quad\cdot\int_{-\infty}^{\infty} G^b_{jm}(\rho,\rho',E,E_0)dE \\
&\approx \frac{\delta_{jm}H[-\boldsymbol{\Omega}_0\cdot\mathbf{n}(\mathbf{x}')]}{2\pi s_x^2 K_x|\partial_u\mathbf{x}'\times\partial_v\mathbf{x}'|}\exp\left\{-\frac{(u'-u_0)^2+(v'-v_0)^2}{2s_x^2}\right\} \\
&\quad\cdot\frac{P_m(E_0)}{P_m(\hat{E}_m(\rho-\rho',E_0))}. \qquad (145)
\end{aligned}$$

These forms will be useful in illustrating results, and also to compare with known theories. Next, specific cases of the zero order Green's function will be discussed in which the theory that has been developed up to this point will be utilized.

III.7 UNIFORM ISOTROPIC BOUNDARY CONDITIONS

When the general convex region V is subject to a uniform isotropic beam of type m particles, the boundary condition will take the form

$$F_j(\mathbf{x}_b,\boldsymbol{\Omega},E) = \delta_{jm}H[-\boldsymbol{\Omega}\cdot\mathbf{n}(\mathbf{x}_b)]F_m(E). \qquad (146)$$

We can then see that the primary flux would be

$$\begin{aligned}
\phi^0_j(\mathbf{x},\boldsymbol{\Omega},E) &= [\mathbf{G}^0\cdot\mathbf{F}]_j(\mathbf{x},\boldsymbol{\Omega},E) \\
&= \sum_{k\geq j}^{N}\delta_{jk}\int_{\partial V}\bar{\delta}(\mathbf{x}'-\mathbf{x}_1)d\mathbf{x}_1\int_{4\pi}\frac{d\boldsymbol{\Omega}_1}{2\pi}\delta(1-\boldsymbol{\Omega}\cdot\boldsymbol{\Omega}_1)\delta_{km}H[-\boldsymbol{\Omega}_1\cdot\mathbf{n}(\mathbf{x}_1)] \\
&\quad\cdot\int_{E}^{\infty}\frac{P_k(\bar{E}_k)}{P_k(E)}\frac{F_m(E_1)dE_1}{\sqrt{2\pi}s_k(\rho-\rho',E_1)}\exp\left\{\frac{-[E-\hat{E}_k(\rho-\rho',E_1)]^2}{2s_k(\rho-\rho',E_1)^2}\right\} \\
&\approx \delta_{jm}H[-\boldsymbol{\Omega}\cdot\mathbf{n}(\mathbf{x}')]\frac{P_m(\bar{E}_m)}{P_m(E)}\int_{-\infty}^{\infty}\frac{F_m(E_1)dE_1}{\sqrt{2\pi}s_m(\rho-\rho',E_1)} \\
&\quad\exp\left\{\frac{-[E-\hat{E}_m(\rho-\rho',E_1)]^2}{2s_m(\rho-\rho',E_1)^2}\right\} \\
&= H[-\boldsymbol{\Omega}\cdot\mathbf{n}(\mathbf{x}')]\int_{-\infty}^{\infty} G^0_{jm}(\rho,\rho',E,E_1)F_m(E_1)dE_1. \qquad (147)
\end{aligned}$$

The integral flux for this case, $\hat{\phi}_j^0(\mathbf{x},\mathbf{\Omega})$ is given by

$$\hat{\phi}_j^0(\mathbf{x},\mathbf{\Omega}) \approx \delta_{jm} H[-\mathbf{\Omega}\cdot\mathbf{n}(\mathbf{x}')] \int_{-\infty}^{\infty} \frac{P_m(E_1)F_m(E_1)}{P_m[\hat{E}_m(\rho-\rho',E_1)]} dE_1. \tag{148}$$

Now, specific boundary conditions that are of interest will be investigated. In particular, start by considering that the boundary condition has a Gaussian energy spectrum.

In this case, $F_m(E)$ will take on the form

$$F_m(E) = \frac{1}{\sqrt{2\pi}s_E} \exp\left\{\frac{-(E-E_0)^2}{2s_E^2}\right\}. \tag{149}$$

With this type of boundary condition, the corresponding primary flux would be

$$\begin{aligned}
\phi_j^0(\mathbf{x},\mathbf{\Omega},E) &\approx \delta_{jm} H[-\mathbf{\Omega}\cdot\mathbf{n}(\mathbf{x}')] \frac{P_m(\bar{E}_m)}{P_m(E)} \int_{-\infty}^{\infty} \exp\left\{\frac{-[E-\hat{E}_m(\rho-\rho',E_1)]^2}{2s_m(\rho-\rho',E_1)^2}\right\} \\
&\quad \cdot \exp\left\{\frac{-(E_1-E_0)^2}{2s_E^2}\right\} \frac{dE_1}{2\pi s_m(\rho-\rho',E_1)s_E} \\
&\approx \delta_{jm} \frac{P_m(\bar{E}_m)}{P_m(E)} \frac{H[-\mathbf{\Omega}\cdot\mathbf{n}(\mathbf{x}')]}{\sqrt{2\pi}s_m^b(\rho-\rho',E_0)} \\
&\quad \cdot \exp\left\{\frac{-(E-\hat{E}_m(\rho-\rho',E_0))^2}{2s_m^b(\rho-\rho',E_0)^2}\right\},
\end{aligned} \tag{150}$$

where $(s_m^b)^2$ is given by equation (137). This primary flux can also be written in terms of the one dimensional broad zero order Green's function [20] as

$$\phi_j^0(\mathbf{x},\mathbf{\Omega},E) = H[-\mathbf{\Omega}\cdot\mathbf{n}(\mathbf{x}')] G_{jm}^b[\rho,\rho',E,E_0]. \tag{151}$$

The integral flux is then given by

$$\hat{\phi}_j^0(\mathbf{x},\mathbf{\Omega}) = \int_{-\infty}^{\infty} \phi_j^0(\mathbf{x},\mathbf{\Omega},E)dE \approx \delta_{jm} H[-\mathbf{\Omega}\cdot\mathbf{n}(\mathbf{x}')] \frac{P_m[E_0]}{P_m[\hat{E}_m(\rho-\rho',E_0)]}. \tag{152}$$

This result is obtained by recalling that the one dimensional zero order Green's

function was approximated by equation (136) and in complete form is given by

$$G^b_{jm}(\rho,\rho',E,E_0) = \frac{\delta_{jm}}{\sqrt{2\pi}}\frac{P_m(\bar{E}_m)}{P_m(E)}\frac{1}{s^b_m(\rho-\rho',E_0)} \cdot\exp\left(-\frac{(E-\hat{E}_m(\rho-\rho',E_0))^2}{2s^b_m(\rho-\rho',E_0)^2}\right). \quad (153)$$

By noting that the attenuation factors vary slowly with E, this allows for the evaluation of the integral by taking the peak value of the exponential and evaluating the other terms at this peak value. Therefore, $P_m(\bar{E}_m)$ would become $P_m(\bar{E}_m(\rho-\rho',\hat{E}_m))$. Applying the definitions of these residual energies, $\bar{E}_m(\rho-\rho',\hat{E}_m)$ reduces to E_0. Also, $P_m(E)$ would become $P_m(\hat{E}_m)$.

III.8 GCR ENERGY SPECTRA

As shown by equation (147), the primary flux for this case is given by

$$\phi^0_j(\mathbf{x},\mathbf{\Omega},E) \approx \delta_{jm}H[-\mathbf{\Omega}\cdot\mathbf{n}(\mathbf{x}')]\frac{P_m(\bar{E}_m)}{P_m(E)}\int_{-\infty}^{\infty}\frac{F_m(E_1)dE_1}{\sqrt{2\pi}s_m(\rho-\rho',E_1)} \exp\left\{\frac{-[E-\hat{E}_m(\rho-\rho',E_1)]^2}{2s_m(\rho-\rho',E_1)^2}\right\}. \quad (154)$$

In general, the energy integral in equation (154) can not be evaluated analytically. One would need to use numerical quadrature to approximate the value. However, when working with GCR Energy Spectra, all of the functions in the integrand vary slowly with E_1 except for the Gaussian, which is very sharply peaked and achieves its maximum when $\hat{E}_m(\rho-\rho',E_1) = E$ or equivalently when $E_1 = \bar{E}_m(\rho-\rho',E)$. We can therefore approximate equation (154) by using the following techniques.

Applying Taylor's Theorem,

$$\hat{E}_m(\rho-\rho',E_1) \approx \hat{E}_m(\rho-\rho',\bar{E}_m) + r_m[\rho-\rho',E](E_1-\bar{E}_m), \quad (155)$$

where

$$r_m[\rho-\rho',E] = [\partial_{E_1}\hat{E}_m(\rho-\rho',E_1)]_{E_1\simeq\bar{E}_m} = \frac{\tilde{S}_m[\bar{E}_m(\rho-\rho',E)]}{\tilde{S}_m[E]}. \quad (156)$$

Therefore

$$\phi_j^0(\mathbf{x},\boldsymbol{\Omega},E) \approx \delta_{jm} H[-\boldsymbol{\Omega}\cdot\mathbf{n}(\mathbf{x}')] \frac{P_m(\bar{E}_m)}{P_m(E)} \frac{\tilde{S}_m(\bar{E}_m)}{\tilde{S}_m(E)} \int_{-\infty}^{\infty} \frac{F_m(E_1)}{\sqrt{2\pi}\tilde{s}_m(\rho-\rho',E_1)} \cdot \exp\left\{-\frac{[E_1-\bar{E}_m(\rho-\rho',E)]^2}{2\tilde{s}_m(\rho-\rho',E_1)^2}\right\} dE_1, \tag{157}$$

where $\tilde{s}_m(\rho-\rho',E_1) = r_m(\rho-\rho',E)s_m(\rho-\rho',E_1)$. This integral can be approximated by taking the value of the Gaussian at its peak, which occurs at $\bar{E}_m$. Thus, the primary flux can be represented as

$$\phi_j^0(\mathbf{x},\boldsymbol{\Omega},E) \approx \delta_{jm} H[-\boldsymbol{\Omega}\cdot\mathbf{n}(\mathbf{x}')] \frac{P_m(\bar{E}_m)}{P_m(E)} \frac{\tilde{S}_m(\bar{E}_m)}{\tilde{S}_m(E)} F_m(\bar{E}_m), \tag{158}$$

where as before, $\bar{E}_m = \bar{E}_m(\rho-\rho',E)$.

Also as before, the integral flux, $\hat{\phi}_j^0(\mathbf{x},\boldsymbol{\Omega})$, is given by equation (148) and needs to be evaluated numerically. By way of illustration, a number of problems in which simple geometrical objects are exposed to an ion beam source, a uniform isotropic radiation, and a space boundary condition will now be investigated.

The ions transported through objects in the section titled **Ion Beam Spectrum** are associated with the previously derived broad zero order Green's function. In the section titled **Uniform Isotropic Boundary Conditions and a Gaussian Energy Profile**, the ions are assumed to be transported with a Gaussian energy profile. Space boundary conditions are used in the section titled **Galactic Cosmic Ray (GCR) Boundary Conditions** in which measured GCR particle fluxes associated with the 1977 solar minimum [11] are transported through the same objects.

CHAPTER IV

ZERO ORDER GREEN'S FUNCTION

IV.1 ION BEAM SPECTRUM

Using the broad zero order Green's function, equation (138), the primary flux can be illustrated for various simple geometric figures.

IV.1.1 Half-space with an Ion Beam Spectrum Boundary Condition

Let V be the half-space, $z \geq 0$, whose boundary ∂V is the xy-plane.

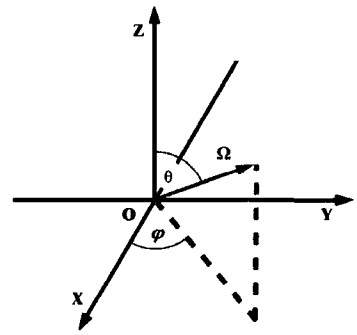

FIGURE 26: Coordinate Variables

For this case, the primary flux is given by

$$
\begin{aligned}
G^b_{jm}(\mathbf{x}, \mathbf{x}_0, \boldsymbol{\Omega}, \boldsymbol{\Omega}_0, E, E_0) \approx & \frac{\delta_{jm} H[-\boldsymbol{\Omega} \cdot \mathbf{n}(\mathbf{x}')]}{4\pi s_x^2 s_{\boldsymbol{\Omega}} s_m^b(\rho - \rho', E_0) K_x K_{\boldsymbol{\Omega}}} \frac{P_m(\bar{E}_m)}{P_m(E)} \\
& \cdot \exp\left\{ -\frac{(x' - x_0)^2 + (y' - y_0)^2}{2s_x^2} \right\} \\
& \cdot \exp\left\{ -\frac{(1 - \boldsymbol{\Omega} \cdot \boldsymbol{\Omega}_0)^2}{2s_{\boldsymbol{\Omega}}^2} \right\} \\
& \cdot \exp\left\{ -\frac{(E - \hat{E}_m(\rho - \rho', E_0))^2}{2s_m^b(\rho - \rho', E_0)^2} \right\}, \qquad (159)
\end{aligned}
$$

where

$$
\partial V = \{\mathbf{x} : \mathbf{x} = \mathbf{x}(x, y), -\infty \leq x \leq \infty, -\infty \leq y \leq \infty\}, \qquad (160)
$$

and

$$dS = dxdy. \tag{161}$$

Figure 27 shows the 1000 MeV/amu iron (^{56}Fe) primary ion flux as a function of inclination angle θ (Deg) and energy E (MeV/amu), at depths $z = 0, 5$, and 15 g/cm^2 of aluminum (^{27}Al) respectively. The results are presented for the case in which $\varphi = 0$ (Deg), $s_E = 30$ (MeV/amu), $s_{\mathbf{\Omega}} = 12$ (Deg), $s_x = .2$, and $\mathbf{\Omega}_0 = (\frac{1}{\sqrt{2}}, 0, \frac{1}{\sqrt{2}})$. At the boundary, the Gaussian profile of the beam is seen where the peak occurs in the mean direction and initial energy of the beam. As the ion propagates into the material, the surviving primary ions lose energy and the variation with theta narrows. The latter occurs because the off-axis ions have lower starting energies due to the Gaussian energy profile boundary condition. Thus, as these ions penetrate into the material, the number of surviving off-axis ions will decrease quicker than those that are in the center of the high energy beam.

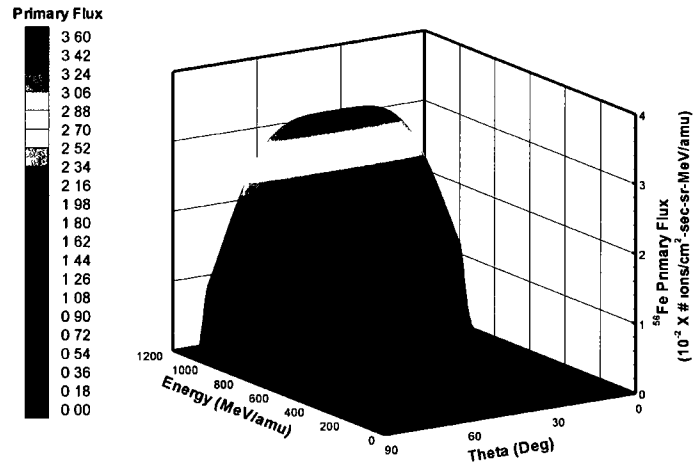

FIGURE 27: The ^{56}Fe primary flux (from left to right) at (0,0,0), (0,0,5), and (0,0,15) with $\varphi = 0$ Deg.

IV.1.2 Sphere with an Ion Beam Spectrum Boundary Condition

Next, consider the target to be a solid aluminum sphere with corresponding equation $x^2 + y^2 + z^2 \leq 16^2$. The boundary will be irradiated by an ion beam source. There are two situations that need to be addressed when working in a spherical coordinate system. These are where $|\partial_\theta \mathbf{x}' \times \partial_\varphi \mathbf{x}'| = 0$ and where $|\partial_\theta \mathbf{x}' \times \partial_\varphi \mathbf{x}'| \neq 0$.

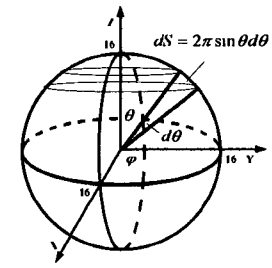

FIGURE 28: Element of surface area

The point at which the Jacobian is equal to 0 is called a singular point. For a spherical coordinate system, this occurs at the poles ($\theta = 0, \pi$). At these points, the parametric ordered pair (θ, φ) breaks down since φ is indeterminate. For this case, the element of surface area will be

$$dS = 2\pi \sin\theta d\theta. \tag{162}$$

Further, at the singular point $\theta = 0$, the surface delta (δ) function is denoted by $\overline{\delta}$ and is given by

$$\overline{\delta}(\mathbf{x} - \mathbf{x_0}) = \frac{\delta(\theta - 0)}{2\pi \sin\theta} = \frac{\delta(1 - \cos\theta)}{2\pi}. \tag{163}$$

Therefore, the corresponding boundary condition becomes

$$\begin{aligned} F_j(\mathbf{x}_b, \mathbf{\Omega}, E) &= \frac{\delta_{jm} H[-\mathbf{\Omega} \cdot \mathbf{n}(\mathbf{x}_b)]}{(2\pi)^{3/2} s_x s_{\mathbf{\Omega}} s_E K_x K_{\mathbf{\Omega}}} \exp\left\{-\frac{(1 - \cos\theta_b)^2}{2s_x^2}\right\} \\ &\quad \cdot \exp\left\{-\frac{(1 - \mathbf{\Omega} \cdot \mathbf{\Omega}_0)^2}{2s_{\mathbf{\Omega}}^2}\right\} \exp\left\{-\frac{(E - E_0)^2}{2s_E^2}\right\}, \end{aligned} \tag{164}$$

where θ_b is the inclination angle of entry, and s_x, $s_{\mathbf{\Omega}}$, and s_E are the spreads in space, angle and energy respectively.

The normalization constants K_x and $K_{\mathbf{\Omega}}$ are derived so that

$$\int_{\partial V} d\mathbf{x}_1 \int_{4\pi} d\mathbf{\Omega}_0 \int_E^\infty dE_0 F_j(\mathbf{x}_b, \mathbf{\Omega}, E) = 1. \tag{165}$$

Thus,

$$
\begin{aligned}
1 \;=\; & \int_{\partial V} d\mathbf{x}_1 \int_{4\pi} d\mathbf{\Omega}_0 \int_E^{\infty} dE_0 \frac{\delta_{jm} H[-\mathbf{\Omega}\cdot\mathbf{n}(\mathbf{x}_b)]}{(2\pi)^{3/2} s_x s_{\mathbf{\Omega}} s_E K_x K_{\mathbf{\Omega}}} \\
& \cdot \exp\left\{-\frac{(1-\cos\theta_b)^2}{2s_x^2}\right\} \\
& \cdot \exp\left\{-\frac{(1-\mathbf{\Omega}\cdot\mathbf{\Omega}_0)^2}{2s_{\mathbf{\Omega}}^2}\right\} \exp\left\{-\frac{(E-E_0)^2}{2s_E^2}\right\}. \qquad (166)
\end{aligned}
$$

Evaluating these integrals yields the normalization constants of

$$
K_x \;=\; \pi \cdot \mathrm{erf}\left(\frac{\sqrt{2}}{s_x}\right), \qquad (167)
$$

$$
K_{\mathbf{\Omega}} \;=\; \pi \cdot \mathrm{erf}\left(\frac{\sqrt{2}}{s_{\mathbf{\Omega}}}\right). \qquad (168)
$$

The Green's function, together with the boundary condition, given by equation (164), can be used to calculate the primary flux.

Therefore, for the case where the ion beam enters the material at the pole, where the entry inclination angle $\theta' = 0$, the broad zero Green's function (138) is given by the expression

$$
\begin{aligned}
G^b_{jm}(\mathbf{x},\mathbf{x}_0,\mathbf{\Omega},\mathbf{\Omega}_0,E,E_0) \;\approx\; & \frac{\delta_{jm} H[-\mathbf{\Omega}\cdot\mathbf{n}(\mathbf{x}')]}{(2\pi)^{3/2} s_x s_{\mathbf{\Omega}} s^b_m(\rho-\rho',E_0) K_x K_{\mathbf{\Omega}}} \frac{P_m(\bar{E}_m)}{P_m(E)} \\
& \cdot \exp\left\{-\frac{(1-\cos\theta')^2}{2s_x^2}\right\} \\
& \cdot \exp\left\{-\frac{(1-\mathbf{\Omega}\cdot\mathbf{\Omega}_0)^2}{2s_{\mathbf{\Omega}}^2}\right\} \\
& \cdot \exp\left\{-\frac{(E-\hat{E}_m(\rho-\rho',E_0))^2}{2s^b_m(\rho-\rho',E_0)^2}\right\}. \qquad (169)
\end{aligned}
$$

Similarly, the pole at $\theta = \pi$ needs to be considered. In this case, the broad zero

order Green's function is given by

$$G^b_{jm}(\mathbf{x},\mathbf{x}_0,\boldsymbol{\Omega},\boldsymbol{\Omega}_0,E,E_0) \approx \frac{\delta_{jm}H[-\boldsymbol{\Omega}\cdot\mathbf{n}(\mathbf{x}')]}{(2\pi)^{3/2}s_x s_{\boldsymbol{\Omega}} s^b_m(\rho-\rho',E_0)K_x K_{\boldsymbol{\Omega}}}\frac{P_m(\bar{E}_m)}{P_m(E)} \cdot\exp\left\{-\frac{(1+\cos\theta')^2}{2s_x^2}\right\} \cdot\exp\left\{-\frac{(1-\boldsymbol{\Omega}\cdot\boldsymbol{\Omega}_0)^2}{2s_{\boldsymbol{\Omega}}^2}\right\} \cdot\exp\left\{-\frac{(E-\hat{E}_m(\rho-\rho',E_0))^2}{2s^b_m(\rho-\rho',E_0)^2}\right\}. \tag{170}$$

Lastly, when calculating the flux away from the poles, where $\mathbf{x}_0=\mathbf{x}_0(\theta_0,\varphi_0)$, and $\mathbf{x}'=\mathbf{x}'(\theta',\varphi')$ are points of entry, and $|\partial_u\mathbf{x}_0\times\partial_v\mathbf{x}_0|\neq 0$, the broad zero order Green's function, and therefore the primary flux, is given by

$$G^b_{jm}(\mathbf{x},\mathbf{x}_0,\boldsymbol{\Omega},\boldsymbol{\Omega}_0,E,E_0) \approx \frac{\delta_{jm}H[-\boldsymbol{\Omega}\cdot\mathbf{n}(\mathbf{x}')]}{4\pi s_x^2 s_{\boldsymbol{\Omega}} s^b_m(\rho-\rho',E_0)K_x K_{\boldsymbol{\Omega}}\sin\theta'}\frac{P_m(\bar{E}_m)}{P_m(E)} \cdot\exp\left\{-\frac{(\varphi'-\varphi_0)^2+(\theta'-\theta_0)^2}{2s_x^2}\right\} \cdot\exp\left\{-\frac{(1-\boldsymbol{\Omega}\cdot\boldsymbol{\Omega}_0)^2}{2s_{\boldsymbol{\Omega}}^2}\right\} \cdot\exp\left\{-\frac{(E-\hat{E}_m(\rho-\rho',E_0))^2}{2s^b_m(\rho-\rho',E_0)^2}\right\}, \tag{171}$$

where

$$K_x = \frac{1}{4}\left[\operatorname{erf}\left(\frac{\pi-\theta_0}{\sqrt{2}s_x}\right)+\operatorname{erf}\left(\frac{\theta_0}{\sqrt{2}s_x}\right)\right] \cdot\left[\operatorname{erf}\left(\frac{2\pi-\varphi_0}{\sqrt{2}s_x}\right)+\operatorname{erf}\left(\frac{\varphi_0}{\sqrt{2}s_x}\right)\right], \tag{172}$$

$$K_{\boldsymbol{\Omega}} = \pi\cdot\operatorname{erf}\left(\frac{\sqrt{2}}{s_{\boldsymbol{\Omega}}}\right). \tag{173}$$

When representing the flux in a spherical coordinate system, both the singular as well as the nonsingular forms of the broad Green's functions may be needed in order to obtain the complete solution. In the figure to follow, figure 29, the iron

(^{56}Fe) primary ion flux where the target is again aluminum (^{27}Al) is represented as a function of θ (Deg) and energy E (MeV/amu). The results are presented for the case in which $\varphi = 0$ (Deg), $s_E = 30$ (MeV/amu), $s_{\mathbf{\Omega}} = 12$ (Deg), $s_x = 12$ (Deg), $\mathbf{\Omega}_0 = (1, 0, 0)$, and $\mathbf{x}_0 = (-16, 0, 0)$. The flux calculations shown below were chosen to illustrate the attenuation into the material. At or near the boundary, the Gaussian profile of the beam is seen where the peak occurs in the mean direction and initial energy of the beam. As the ion propagates into the material, it loses energy and the variation with theta decreases.

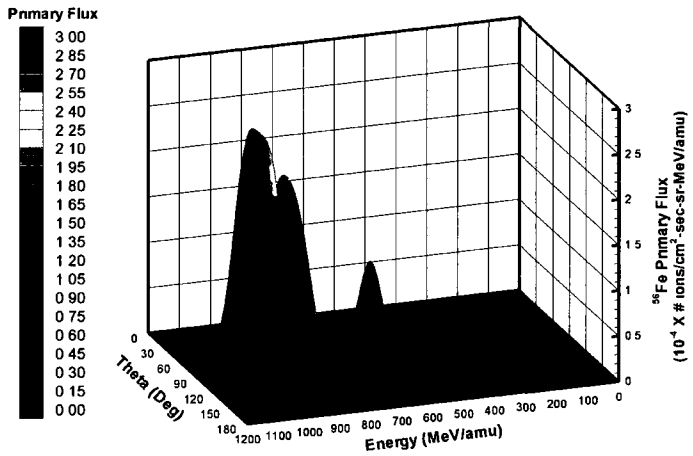

FIGURE 29: The ^{56}Fe primary flux (from left to right) at (-16,0,0), (-12,0,0), (0,0,0), and (12,0,0).

IV.1.3 Integral Flux

As another illustration of the ion beam spectrum where the surface is a sphere, the energy independent integral flux is calculated. For the nonsingular case, the integral flux is given by

$$\begin{aligned}\hat{G}^b_{jm}(\mathbf{x},\mathbf{x}_0,\mathbf{\Omega},\mathbf{\Omega}_0,E_0) &= \int_{-\infty}^{\infty} G^b_{jm}(\mathbf{x},\mathbf{x}_0,\mathbf{\Omega},\mathbf{\Omega}_0,E,E_0)dE \\ &= \frac{\delta_{jm}H[-\mathbf{\Omega}\cdot\mathbf{n}(\mathbf{x}')]}{4\pi s_x^2 K_x K_{\mathbf{\Omega}} s_{\mathbf{\Omega}} \sin\theta'} \exp\left\{-\frac{(\theta'-\theta_0)^2+(\varphi'-\varphi_0)^2}{2s_x^2}\right\} \\ &\quad \cdot \exp\left\{-\frac{(1-\mathbf{\Omega}\cdot\mathbf{\Omega}_0)^2}{2s_{\mathbf{\Omega}}^2}\right\} \frac{P_m(E_0)}{P_j(\hat{E}_m(\rho-\rho',E_0))}. \end{aligned} \quad (174)$$

The integral flux for the singular points (when $\theta = 0, \pi$) are given by

$$\begin{aligned}\hat{G}^b_{jm}(\mathbf{x},\mathbf{x}_0,\mathbf{\Omega},\mathbf{\Omega}_0,E_0) &= \int_{-\infty}^{\infty} G^b_{jm}(\mathbf{x},\mathbf{x}_0,\mathbf{\Omega},\mathbf{\Omega}_0,E,E_0)dE \\ &= \frac{\delta_{jm}H[-\mathbf{\Omega}\cdot\mathbf{n}(\mathbf{x}')]}{(2\pi)^{3/2} s_x K_x K_{\mathbf{\Omega}} s_{\mathbf{\Omega}}} \exp\left\{-\frac{(1-\cos\theta')^2}{2s_x^2}\right\} \\ &\quad \cdot \exp\left\{-\frac{(1-\mathbf{\Omega}\cdot\mathbf{\Omega}_0)^2}{2s_{\mathbf{\Omega}}^2}\right\} \frac{P_m(E_0)}{P_j(\hat{E}_m(\rho-\rho',E_0))}, \end{aligned} \quad (175)$$

and

$$\begin{aligned}\hat{G}^b_{jm}(\mathbf{x},\mathbf{x}_0,\mathbf{\Omega},\mathbf{\Omega}_0,E_0) &= \int_{-\infty}^{\infty} G^b_{jm}(\mathbf{x},\mathbf{x}_0,\mathbf{\Omega},\mathbf{\Omega}_0,E,E_0)dE \\ &= \frac{\delta_{jm}H[-\mathbf{\Omega}\cdot\mathbf{n}(\mathbf{x}')]}{(2\pi)^{3/2} s_x K_x K_{\mathbf{\Omega}} s_{\mathbf{\Omega}}} \exp\left\{-\frac{(1+\cos\theta')^2}{2s_x^2}\right\} \\ &\quad \cdot \exp\left\{-\frac{(1-\mathbf{\Omega}\cdot\mathbf{\Omega}_0)^2}{2s_{\mathbf{\Omega}}^2}\right\} \frac{P_m(E_0)}{P_j(\hat{E}_m(\rho-\rho',E_0))} \end{aligned} \quad (176)$$

respectively.

Since there is built in symmetry on the surface of a sphere, it is sufficient to show the flux of a beam that is entering the material both perpendicular and not perpendicular to the surface. The following figures will demonstrate the profile of the zero order integral flux plotted as a function of φ and θ (Deg). The variation of $\hat{G}^b_{jm}(\mathbf{x},\mathbf{x}_0,\mathbf{\Omega},\mathbf{\Omega}_0,E_0)$ is presented in Cartesian form. By eliminating the energy dependance, the dependance on angle is seen in these figures.

The first plot is given with the target as aluminum (^{27}Al) and the projectile as iron (^{56}Fe) and where $s_E = 30$ (MeV/amu), $s_{\mathbf{\Omega}} = 12$ (Deg), $s_x = 12$ (Deg), $\mathbf{\Omega}_0 = (1,0,0)$, $\mathbf{x}_0 = (-16,0,0)$, and $\mathbf{x} = (0,0,0)$. Furthermore, in the second plot $s_E = 30$ (MeV/amu), $s_{\mathbf{\Omega}} = 12$ (Deg), $s_x = 12$ (Deg), $\mathbf{\Omega}_0 = (\frac{1}{2},\frac{1}{2},\frac{1}{\sqrt{2}})$, $\mathbf{x}_0 = (-8,-8,-11.3)$,

and $\mathbf{x} = (0, 0, 0)$. The concentration of the flux about the initial mean direction is seen in these plots.

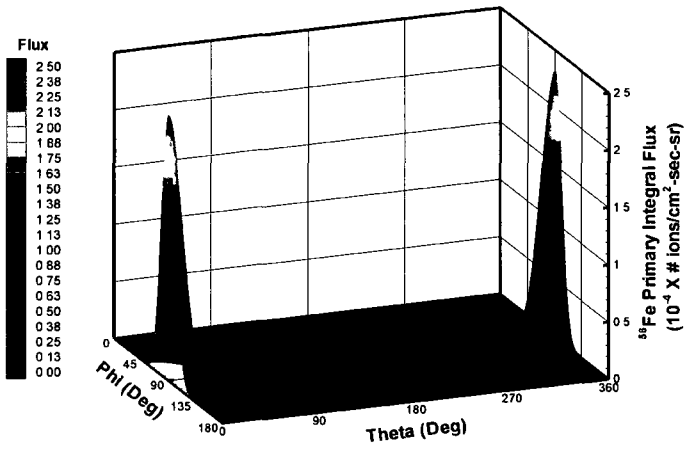

FIGURE 30: A perpendicular ion beam with the entering position of (-16,0,0).

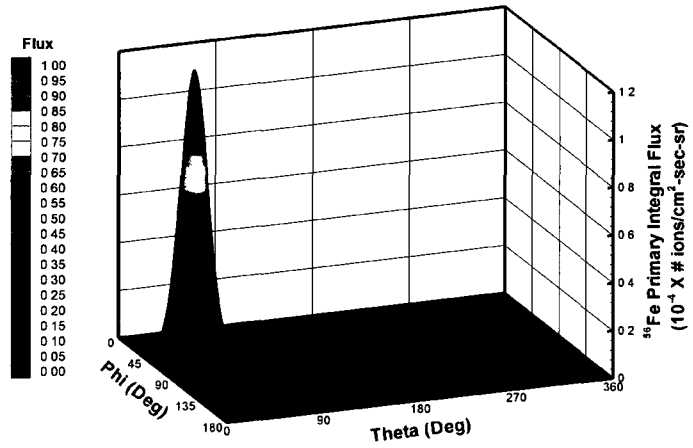

FIGURE 31: A non-perpendicular ion beam with the entering position of (-8,-8,-11.3).

From the analysis and results just presented, one can see that the Green's function solution of the Boltzmann equation is capable of representing an ion beam spectrum. In addition, the Green's function solution can also be used in the cases of broad energy and angular spectra. These cases will now be discussed.

IV.2 A UNIFORM ISOTROPIC BOUNDARY CONDITION AND A GAUSSIAN ENERGY PROFILE

IV.2.1 Half-space with a Uniform Isotropic Boundary Condition and a Gaussian Energy Profile

Let V be the half-space, $z \geq 0$, as represented in figure 32, whose boundary ∂V is the xy-plane.

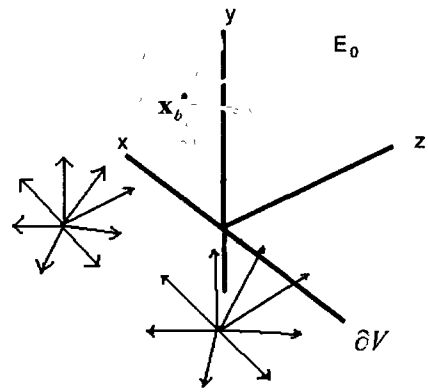

FIGURE 32: A Uniform Isotropic Boundary Condition

In this case, it is assumed that the boundary is subject to a uniform beam of type m particles with mean energy E_0 MeV/amu that are isotropic in direction and have a Gaussian energy profile. The boundary condition then takes the form as given by equations (146) and (149), and the primary flux is given by

$$\begin{aligned}\phi_j^0(\mathbf{x},\boldsymbol{\Omega},E) &= [\mathbf{G}^0\cdot\mathbf{F}]_j(\mathbf{x},\boldsymbol{\Omega},E)\\ &\approx \delta_{jm}H[\boldsymbol{\Omega}\cdot\mathbf{k}]\frac{P_m(\bar{E}_m)}{P_m(E)}\\ &\cdot\frac{1}{\sqrt{2\pi}s_m^b(\rho-\rho',E_0)}\exp\left\{\frac{-[E-\hat{E}_m(\rho-\rho',E_0)]^2}{2s_m^b(\rho-\rho',E_0)^2}\right\},\end{aligned} \tag{177}$$

where $(s_m^b)^2$ is given by equation (137), and

$$\rho-\rho'=\frac{z}{\Omega_3},\quad(\Omega_3>0). \tag{178}$$

Relative to the Cartesian coordinate system $OXYZ$, with spherical polar coordinates $(1, \gamma, \alpha)$, the direction vector $\mathbf{\Omega}$ has components

$$\mathbf{\Omega} = \begin{pmatrix} \Omega_1 \\ \Omega_2 \\ \Omega_3 \end{pmatrix} = \begin{pmatrix} \sin\gamma\cos\alpha \\ \sin\gamma\sin\alpha \\ \cos\gamma \end{pmatrix}. \tag{179}$$

Therefore, the distance of a point $\mathbf{x} \in V$ from the boundary is given by

$$\rho - \rho' = \frac{z}{\cos\gamma}, \quad (0 \leq \gamma < \pi/2). \tag{180}$$

Thus, the primary flux can be expressed in terms of the one dimensional broad Green's function [20] by

$$\phi_j^0(\mathbf{x}, \mathbf{\Omega}, E) = H[\mathbf{\Omega} \cdot \mathbf{k}] G_{jm}^b[\rho, \rho', E, E_0] = H[\cos\gamma] G_{jm}^b[z/\cos\gamma, 0, E, E_0]. \tag{181}$$

Figure 33 shows the 1000 MeV/amu iron (^{56}Fe) primary ion flux as a function of γ (Deg) and energy E (MeV/amu), at depths $z = 0, 5$, and 15 g/cm^2 of aluminum (^{27}Al) respectively. In this case, there is axial symmetry about the z-direction and therefore, the results are presented only for the case in which $\alpha = 0$ (Deg).

The zero order integral flux

$$\hat{\phi}_j(\mathbf{x}, \mathbf{\Omega}[\gamma, \alpha]) = \int_{-\infty}^{\infty} \phi_j(\mathbf{x}, \mathbf{\Omega}, E) dE \approx \delta_{jm} H(\cos\gamma) \frac{P_m[E_0]}{P_m[\hat{E}_m(z/\cos\gamma, E_0)]} \tag{182}$$

is exhibited in figures 34-35, where it is plotted as a function of γ and α at depths $z = 0$, and 5 g/cm^2 of aluminum (^{27}Al) respectively. The variation of $\hat{\phi}_j(\mathbf{x}, \mathbf{\Omega})$ is presented in Cartesian form. The lack of variation with α confirms the axi-symmetric nature of the solution.

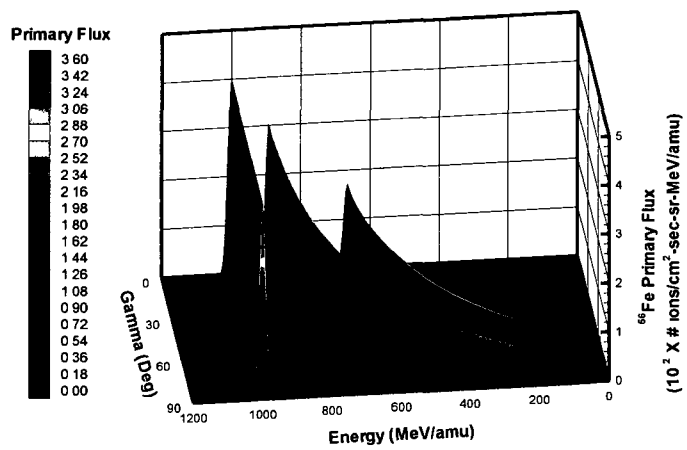

FIGURE 33: The ^{56}Fe primary flux (from left to right) at depths $z = 0, 5$, and 15 g/cm^2 with $\alpha = 0$ Deg.

The uniform nature of the boundary flux is exhibited in figure 33. As the depth into the material increases, which corresponds to an increase in gamma, the primary flux gradually decreases until the stopping range of the projectile is reached.

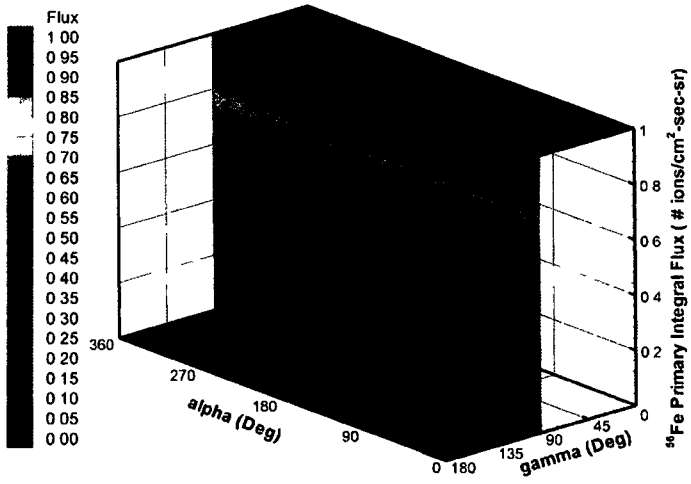

FIGURE 34: The energy independent integral ^{56}Fe primary flux at depth $z = 0$ g/cm^2.

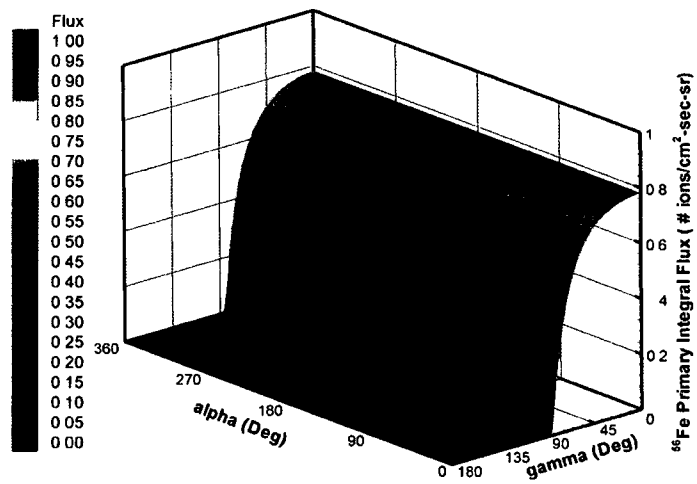

FIGURE 35: The energy independent integral ^{56}Fe primary flux at depth $z = 5$ g/cm^2.

As seen in figures 34 and 35, the only admissible directions for the external flux at the boundary are those into the target material. Again, the attenuation of the primary flux is seen as the depth into the material approaches the ion's stopping range.

IV.2.2 Hemisphere with a Uniform Isotropic Boundary Condition and a Gaussian Energy Profile

The target in this case is a hemispherical aluminum (^{27}Al) solid given by the inequalities $x^2 + y^2 + z^2 \leq 16^2$, $z \geq 0$. A uniform isotropic beam of iron (^{56}Fe) ions with mean energy $E_0 = 1000$ MeV/amu and energy spread $s_E = 10$ MeV/amu will irradiate the boundary. In the figures to follow, figures 37-40, the iron (^{56}Fe) primary ion flux is represented as a function of γ (Deg) and energy E (MeV/amu). Various values of α (Deg) and several target points within the material are tested.

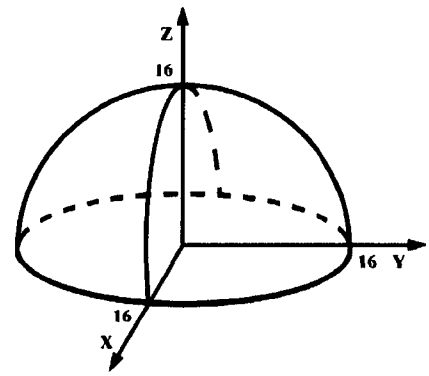

FIGURE 36: Hemisphere

As γ varies, the distance that the primary ion has traveled changes depending on the position of the point inside the material. The attenuation of the projectile can be seen to gradually decrease as its stopping range is approached.

The profile of the zero order integral flux $\hat{\phi}_J(\mathbf{x}, \mathbf{\Omega})$, given by equation (140), is exhibited in figures 41-42, where it is plotted as a function of γ and α (Deg). The variation of $\hat{\phi}_J(\mathbf{x}, \mathbf{\Omega})$ is presented in Cartesian form. By eliminating the energy dependance, the dependance on angle is seen in these figures. Again, the relationship between the distance traveled into the material and the corresponding flux is seen.

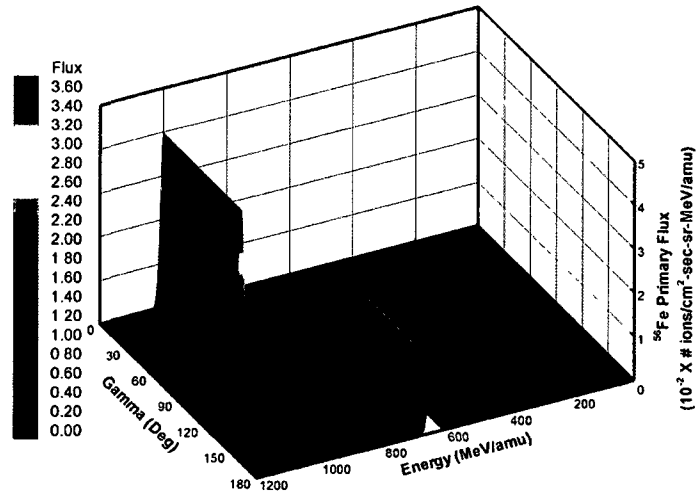

FIGURE 37: The ^{56}Fe primary flux at (0,0,0) with $\alpha = 0$ Deg.

In figure 37, the symmetry of the surface is evident. The flux of primary particles that have reached the point (0,0,0) from every admissible entry point will be the same since these points are equidistant from the origin. Outside of this region, the primary flux is given by the input environment.

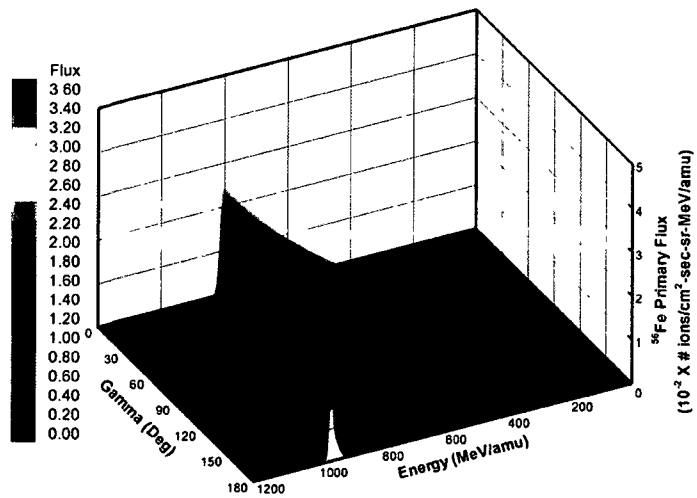

FIGURE 38: The ^{56}Fe primary flux at (11,0,9) with $\alpha = 0$ Deg.

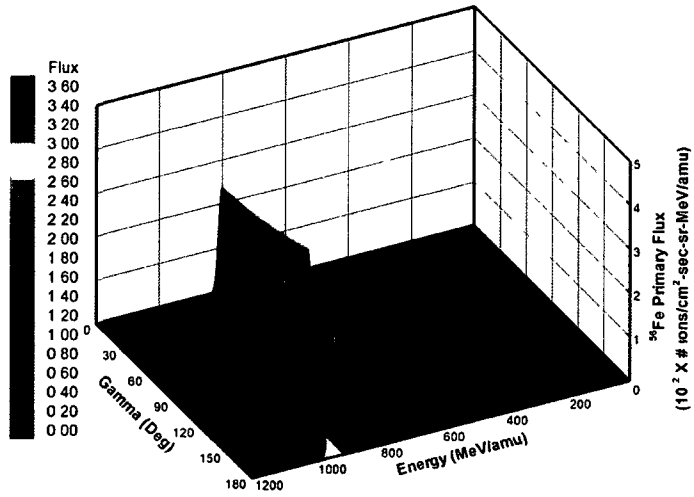

FIGURE 39: The ^{56}Fe primary flux at (11,0,9) with $\alpha = 90$ Deg.

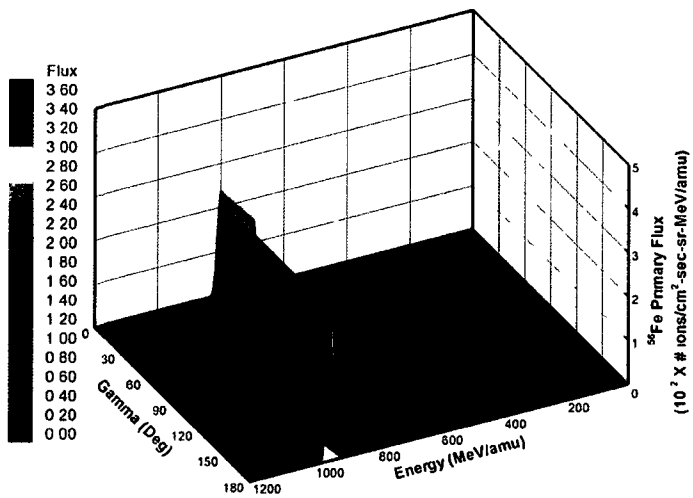

FIGURE 40: The ^{56}Fe primary flux at (11,0,9) with $\alpha = 180$ Deg.

Figures 38-40 demonstrate the lack of axial symmetry about the z-direction at the point (11,0,9) in the material and that the magnitude of the primary flux is seen to be directly correlated with the distance that the ion has traveled into the material.

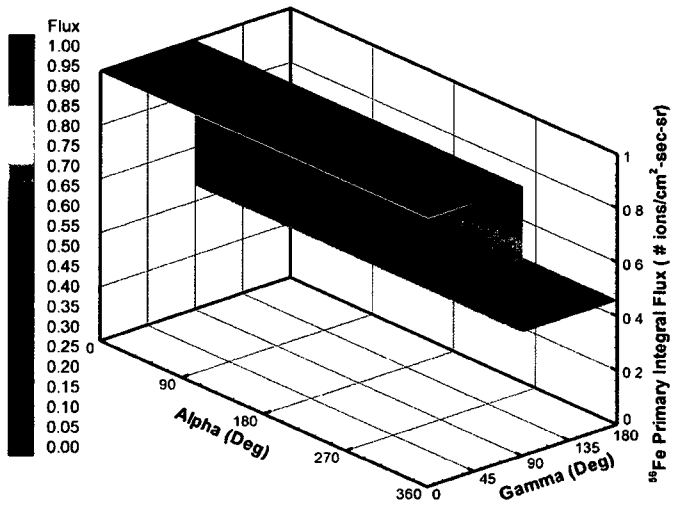

FIGURE 41: The energy independent integral ^{56}Fe primary flux at (0,0,0).

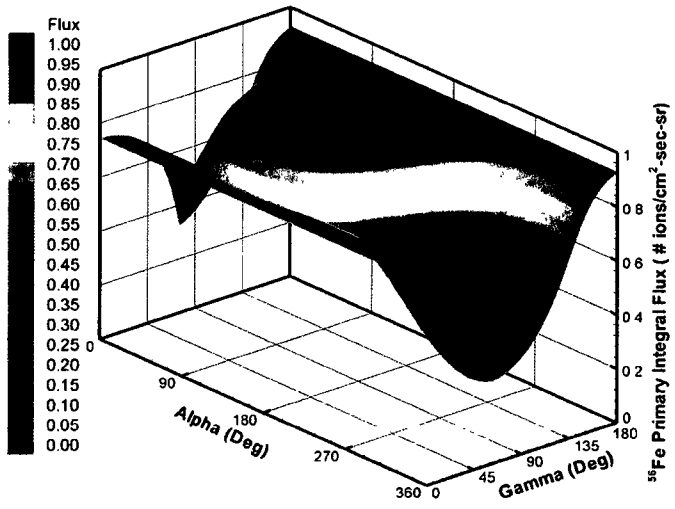

FIGURE 42: The energy independent integral ^{56}Fe primary flux at (10,-10,6).

Integrating out the energy helps to illustrate the dependance on angle at various points in the material as is shown in figures 41-42.

A sample of simple geometries will be used throughout this dissertation in order to demonstrate the ability to incorporate convex boundary regions into the problem and also to show the behavior of the flux at edge points of these regions. Next, the galactic

cosmic ray boundary condition will be explored where again simple geometries will be used as targets.

IV.3 GALACTIC COSMIC RAY (GCR) BOUNDARY CONDITION

Cosmic ray ions are composed of 85 percent protons, 13 percent alpha particles, and about 2 percent of electrons and nuclei of lithium, boron, carbon, oxygen, all the way up to tin [6]. The most abundant particles, such as H, He, C, O, and Fe are known as primary (naturally abundant) particles. Primary cosmic rays are particles that are accelerated (generated) at astrophysical sources [6]. Other particles such as Li, Be, B, Sc, etc. are known as secondary particles and are less abundant [5]. Secondary particles are produced in the interaction of the primary particles with the interstellar gas [6].

Collectively these charged particles are called galactic cosmic rays (GCR). GCR is always present in interstellar space, and the intensity of the GCR is modulated by the solar cycle, during which the Sun's magnetic field varies approximately every eleven years. This type of radiation originates from unknown parts of the galaxy and contains energetic charged particles ranging from hydrogen to tin. These particles can penetrate many of the materials that are now being used to make spacecraft. They produce fragments that can penetrate even deeper into most materials, and could pose a threat to the health and safety of astronauts. This fact makes shielding against GCR a challenging problem.

In this section, the propagation of iron (^{56}Fe) through various aluminum surfaces will be investigated with the imposed GCR boundary conditions. Then, the propagation of carbon (^{12}C), helium (^{4}He), hydrogen (^{1}H), and oxygen (^{16}O) ions through a selection of aluminum (^{27}Al) surfaces will be investigated in order to cover the most abundant particles that are seen in GCR. The magnitude of the primary flux of these elements depends on their abundance in the composition of the GCR and their mass, but the overall shape of their spectra remains the same.

IV.3.1 Half-space with a GCR Boundary Condition

Let V be the half-space, $z \geq 0$, whose boundary ∂V is the xy-plane. In this case, the measured GCR type m particle flux associated with the 1977 solar minimum [11]

is taken as the incoming flux. Thus, the boundary condition will take the form

$$F_j(\mathbf{x}_b, \mathbf{\Omega}, E) = \delta_{jm} H[\mathbf{\Omega}\cdot\mathbf{k}] F_m(E). \tag{183}$$

Following our previous analysis, equation (158), the primary flux will be given by

$$\phi_j^0(\mathbf{x}, \mathbf{\Omega}, E) \approx \delta_{jm} H[\cos\gamma] \frac{P_m(\bar{E}_m)}{P_m(E)} \frac{\tilde{S}_m(\bar{E}_m)}{\tilde{S}_m(E)} F_m(\bar{E}_m). \tag{184}$$

Figures 43-44 show the 1000 MeV/amu iron (^{56}Fe) primary ion flux as a function of γ (Deg) and energy E (MeV/amu), at depths $z = 0, 5$, and 15 g/cm^2 of (^{27}Al) aluminum respectively. In this case, there is axial symmetry about the z-direction and therefore, the results are presented only for the case in which $\alpha = 0$ (Deg).

The profile of the zero order integral flux $\hat{\phi}_j(\mathbf{x}, \mathbf{\Omega})$, given by equation (140), is exhibited in figures 45-46, where it is plotted as a function of γ and α (Deg) at depths $z = 0$, and 5 g/cm^2 of aluminum (^{27}Al) respectively. The variation of $\hat{\phi}_j(\mathbf{x}, \mathbf{\Omega})$ is presented in Cartesian form. The lack of variation with α confirms the axi-symmetric nature of the solution.

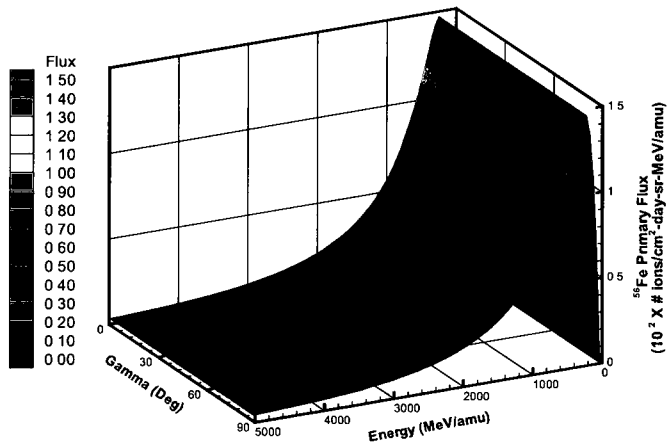

FIGURE 43: The ^{56}Fe primary flux at depth $z = 0$ g/cm^2 with $\alpha = 0$ Deg.

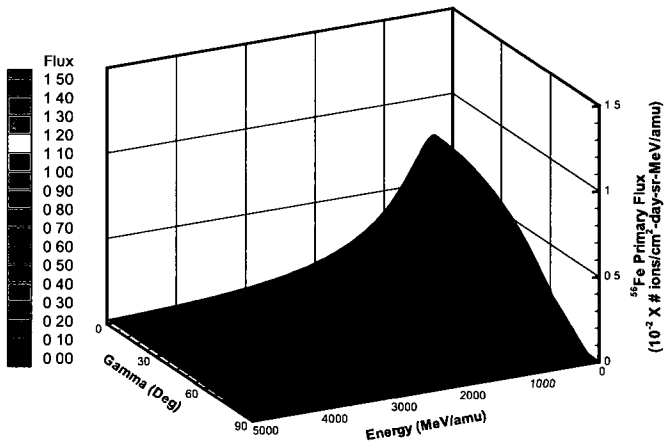

FIGURE 44: The ^{56}Fe primary flux at depth $z = 5$ g/cm^2 with $\alpha = 0$ Deg.

As seen in figure 43, the isotropy of the GCR spectra is clearly seen at the boundary. As the depth increases, as is seen in figure 44, the isotropy is destroyed and the broad spectra of energy is also apparent.

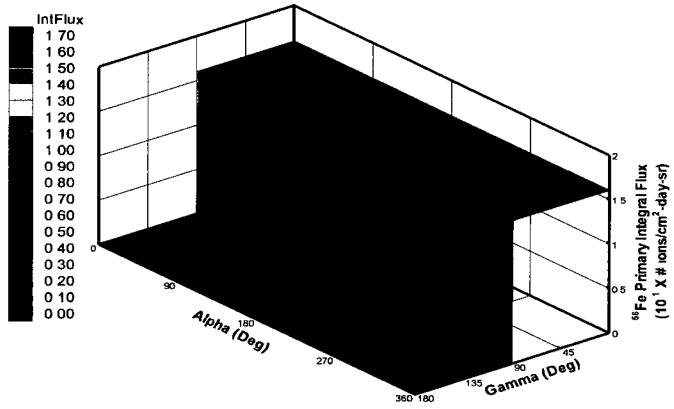

FIGURE 45: The energy independent integral ^{56}Fe primary flux at depth $z = 0$ g/cm^2.

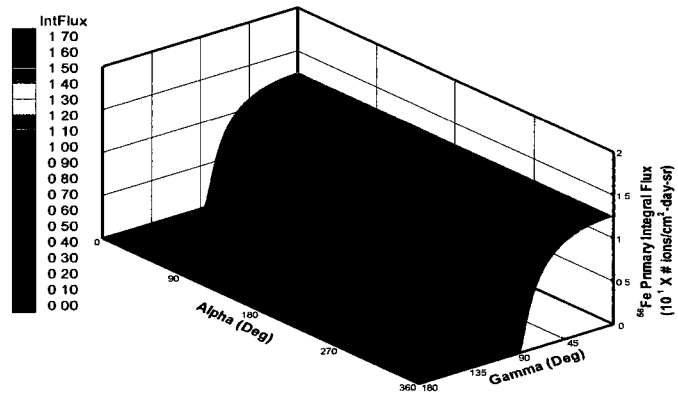

FIGURE 46: The energy independent integral ^{56}Fe primary flux at depth $z = 5$ g/cm^2.

With the energy dependence eliminated, the variation of the primary flux with angle is seen in figures 45 and 46. Again, the relationship between the distance traveled into the material and the corresponding flux is seen.

IV.3.2 Hemisphere with a GCR Boundary Condition

The target in this case is a hemispherical aluminum (^{27}Al) solid given by the inequalities $x^2 + y^2 + z^2 \leq 16^2$, $z \geq 0$. The boundary will be irradiated by the measured GCR type m particle flux associated with the 1977 solar minimum [11]. In the figures to follow, figures 47-50, the iron (^{56}Fe) primary ion flux is represented as a function of γ (Deg) and energy E (MeV/amu). Various values of α (Deg) and several target points within the material are tested.

Effects due to the contour of the boundary are apparent in the figures to follow. As γ varies, the distance that the primary ion has traveled changes depending on the position of the point inside the material. The attenuation of the projectile can also be seen in the figures.

The profile of the zero order integral flux $\hat{\phi}_j(\mathbf{x}, \mathbf{\Omega})$, given by equation (140), is exhibited in figures 51-52, where it is plotted as a function of γ and α (Deg). The variation of $\hat{\phi}_j(\mathbf{x}, \mathbf{\Omega})$ is presented in Cartesian form. By eliminating the energy dependance, the dependance on angle is seen in these figures. Again, the relationship between the distance traveled into the material and the corresponding flux is seen.

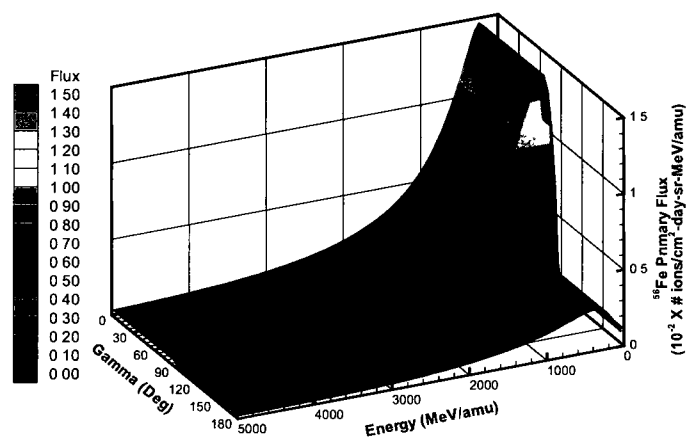

FIGURE 47: The ^{56}Fe primary flux at (0,0,0) with $\alpha = 0$ Deg.

In figure 47, the symmetry of the surface is evident. The flux of primary particles that have reached the point (0,0,0) from every admissible entry point will be the same since these points are equidistant from the origin. Outside of this region, the primary flux is given by the input environment.

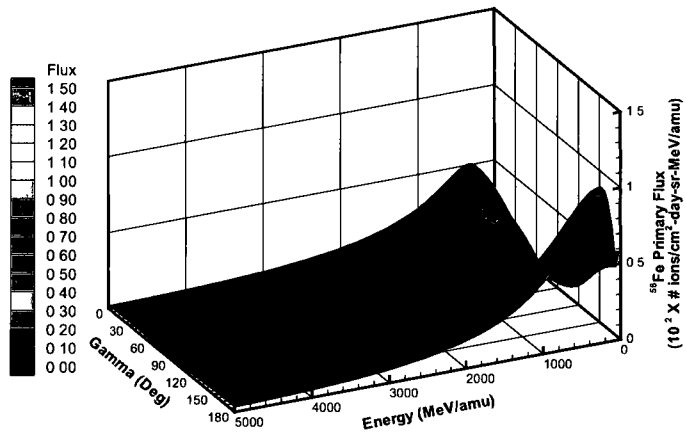

FIGURE 48: The ^{56}Fe primary flux at (11,0,9) with $\alpha = 0$ Deg.

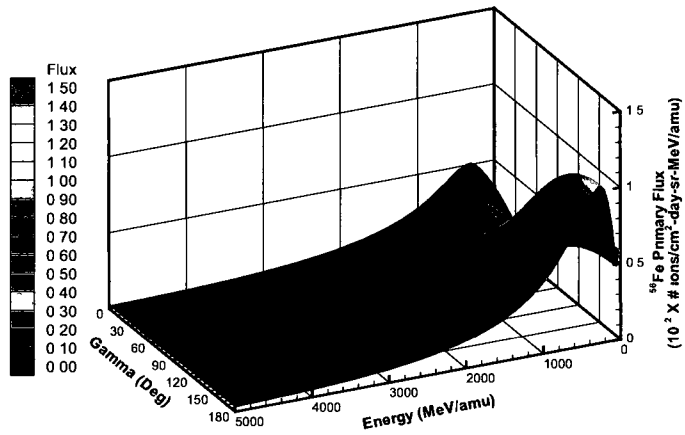

FIGURE 49: The ^{56}Fe primary flux at (11,0,9) with $\alpha = 90$ Deg.

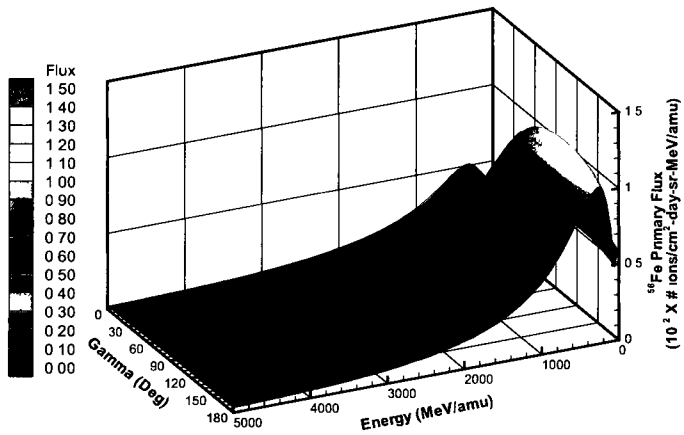

FIGURE 50: The ^{56}Fe primary flux at (11,0,9) with $\alpha = 180$ Deg.

Figures 48-50 demonstrate the fact that there is no axial symmetry about the z-direction for this point in the material. In addition, the figures show that the magnitude of the primary flux is seen to be directly correlated with the distance that the ion has traveled into the material.

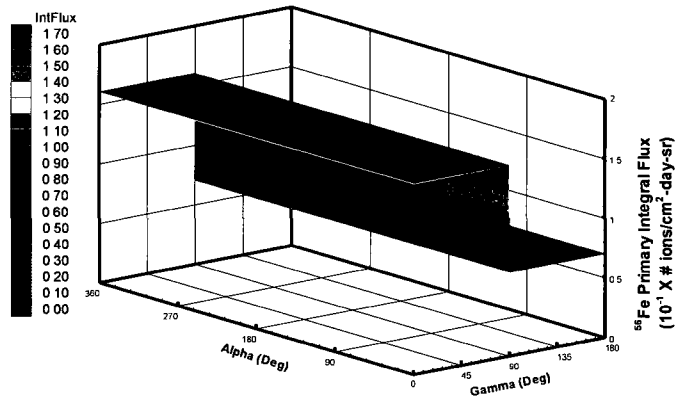

FIGURE 51: The energy independent integral ^{56}Fe primary flux at (0,0,0).

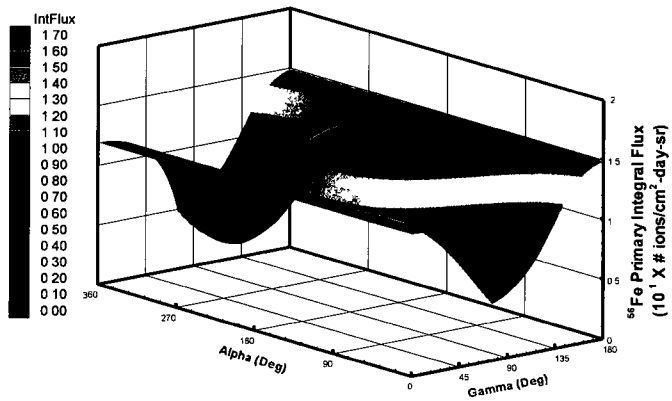

FIGURE 52: The energy independent integral ^{56}Fe primary flux at (10,-10,6).

Integrating out the energy helps to illustrate the dependance on angle at various points in the material as is shown in figures 51-52.

IV.3.3 Half-space with a GCR Boundary Condition using a Hydrogen Projectile

It is also important to demonstrate that the flux calculations can be done for light ions as well. Specifically, hydrogen as well as carbon will be used as projectiles. First, a half-space boundary will be considered where the incoming ion is hydrogen.

Let V be the half-space, $z \geq 0$, whose boundary ∂V is the xy-plane. In this case, the measured GCR type m particle flux associated with the 1977 solar minimum [11] will be taken as our incoming flux. Thus, the boundary condition will take the form of equation (183).

Following our previous analysis, equation (158), the primary flux $\phi_j^0(\mathbf{x}, \mathbf{\Omega}, E)$ is represented by equation (184).

Figures 53-55 show the hydrogen (^{1}H) primary ion flux as a function of γ (Deg) and energy E (MeV/amu), at depth $z = 0, 5$, and 15 g/cm^2 of aluminum (^{27}Al) respectively. In this case, there is axial symmetry about the z-direction and therefore, the results are presented only for the case in which $\alpha = 0$ (Deg).

The profile of the zero order integral flux $\hat{\phi}_j(\mathbf{x}, \mathbf{\Omega})$, given by equation (140), is exhibited in figures 56-57, where it is plotted as a function of γ and α (Deg) at depths $z = 0$, and 5 g/cm^2 of aluminum (^{27}Al) respectively. The variation of $\hat{\phi}_j(\mathbf{x}, \mathbf{\Omega})$ is presented in Cartesian form. The lack of variation with α confirms the axi-symmetric nature of the solution.

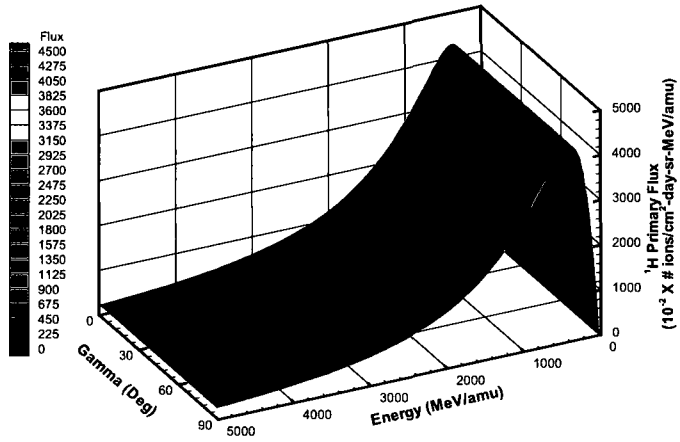

FIGURE 53: The ^{1}H primary flux at depth $z = 0$ g/cm^2 with $\alpha = 0$ Deg.

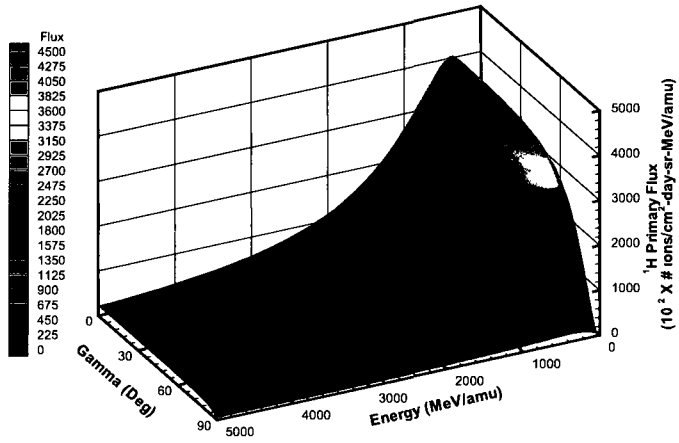

FIGURE 54: The ^{1}H primary flux at depth $z = 5$ g/cm^2 with $\alpha = 0$ Deg.

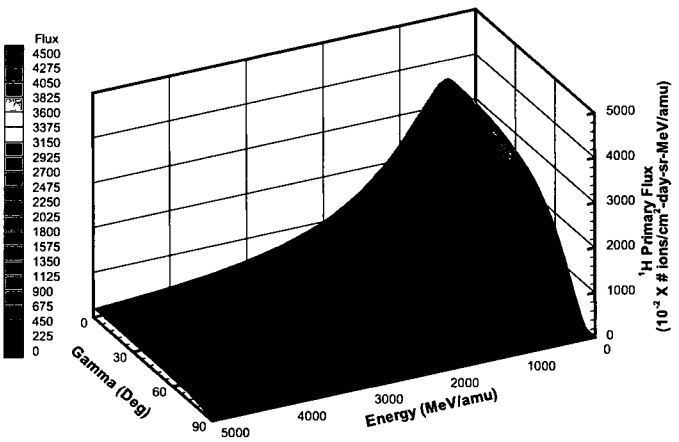

FIGURE 55: The ^{1}H primary flux at depth $z = 15$ g/cm^2 with $\alpha = 0$ Deg.

As seen in figure 53, the isotropy of the GCR spectra is clearly seen at the boundary. As the depth increases, as is seen in figures 54 and 55, the isotropy is destroyed and the broad spectra of energy is also apparent.

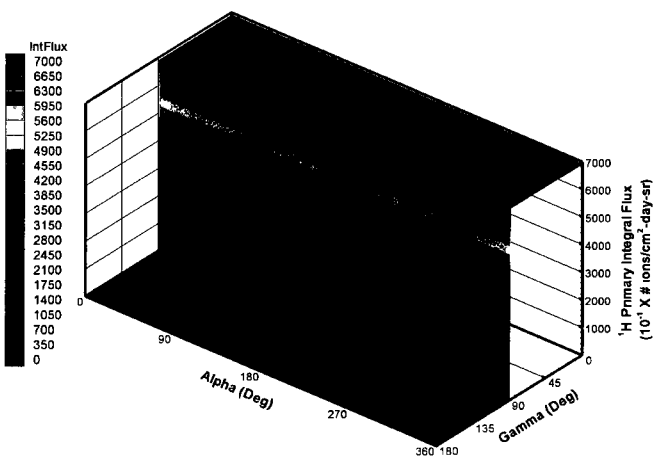

FIGURE 56: The energy independent integral ^{1}H primary flux at depth $z = 0$ g/cm^2.

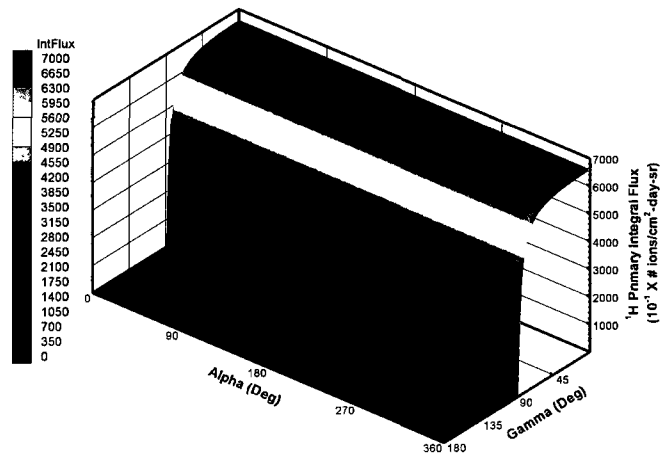

FIGURE 57: The energy independent integral ^{1}H primary flux at depth $z = 5$ g/cm^2.

With the energy dependence eliminated, the variation of the primary flux with angle is seen in these figures. Again, the relationship between the distance traveled into the material and the corresponding flux is seen.

IV.3.4 Half-space with a GCR Boundary Condition using an Oxygen Projectile

Let V be the half-space, $z \geq 0$, whose boundary ∂V is the xy-plane. In this case, the measured GCR type m particle flux associated with the 1977 solar minimum [11] will be taken as our incoming flux. Thus, the boundary condition will take the form of equation (183).

Following our previous analysis, equation (158), the primary flux $\phi_j^0(\mathbf{x}, \mathbf{\Omega}, E)$ is represented by equation (184).

Figures 58-60 show the oxygen (^{16}O) primary ion flux as a function of γ (Deg) and energy E (MeV/amu), at depth $z = 0, 5$, and 15 g/cm^2 of aluminum (^{27}Al) respectively. In this case, there is axial symmetry about the z-direction and therefore, the results are presented only for the case in which $\alpha = 0$ (Deg).

The profile of the zero order integral flux $\hat{\phi}_j(\mathbf{x}, \mathbf{\Omega})$, given by equation (140), is exhibited in figures 61-63, where it is plotted as a function of γ and α (Deg) at depths $z = 0, 5$, and 15 g/cm^2 of aluminum (^{27}Al) respectively. The variation of $\hat{\phi}_j(\mathbf{x}, \mathbf{\Omega})$ is presented in Cartesian form. The lack of variation with α confirms the axi-symmetric nature of the solution.

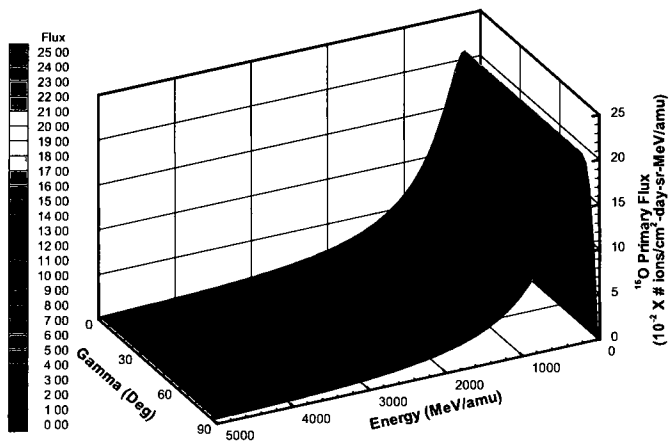

FIGURE 58: The ^{16}O primary flux at depth $z = 0$ g/cm^2 with $\alpha = 0$ Deg.

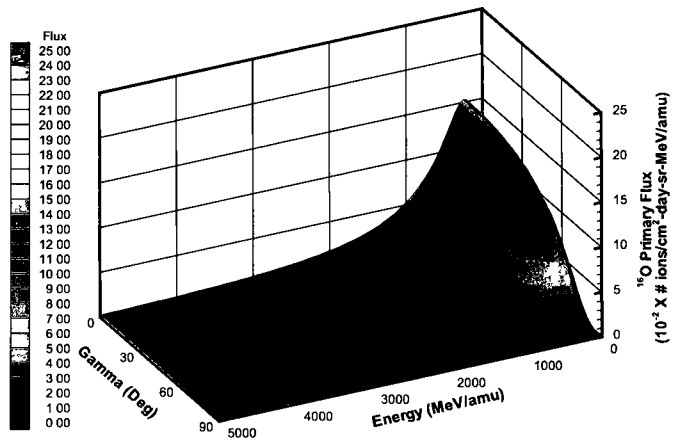

FIGURE 59: The ^{16}O primary flux at depth $z = 5$ g/cm^2 with $\alpha = 0$ Deg.

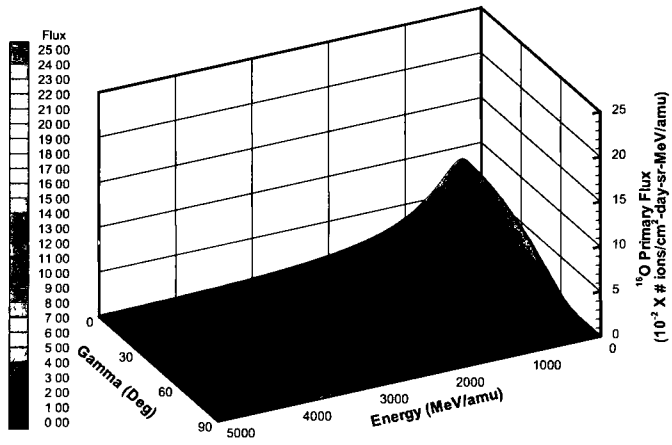

FIGURE 60: The ^{16}O primary flux at depth $z = 15$ g/cm^2 with $\alpha = 0$ Deg.

In the figures above, the attenuation of the primary flux is seen.

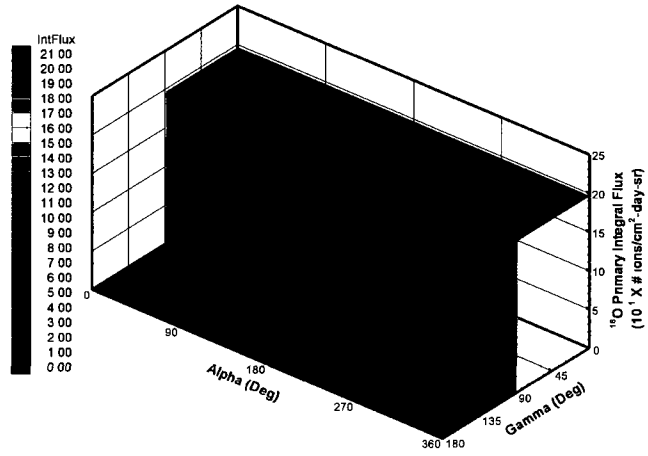

FIGURE 61: The energy independent integral ^{16}O primary flux at depth $z = 0$ g/cm^2.

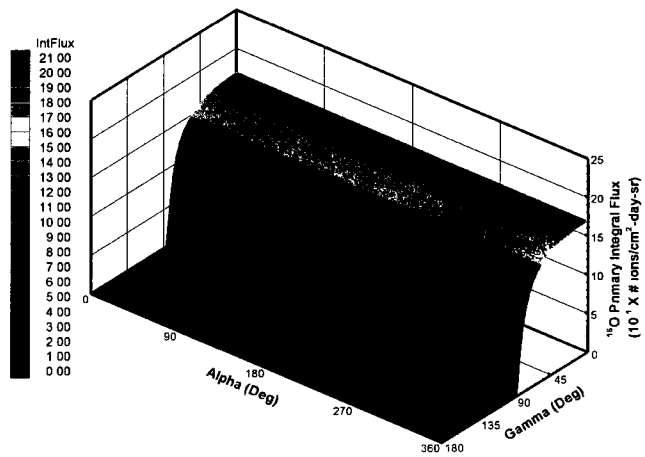

FIGURE 62: The energy independent integral ^{16}O primary flux at depth $z = 5$ g/cm^2.

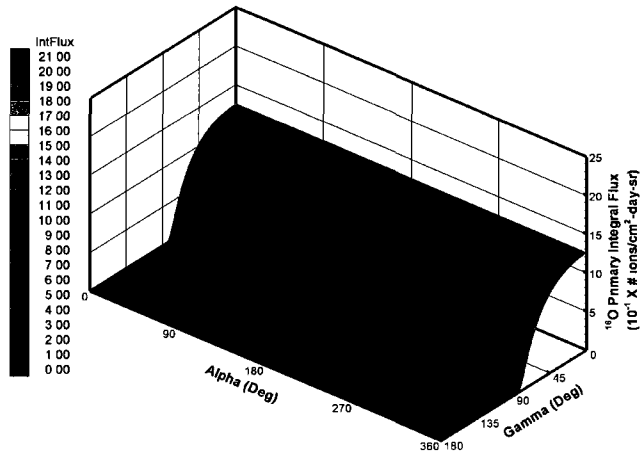

FIGURE 63: The energy independent integral ^{16}O primary flux at depth $z = 15$ g/cm^2.

With the energy dependence eliminated, the variation of the primary flux with angle is seen in these figures. Again, the relationship between the distance traveled into the material and the corresponding flux is seen.

CHAPTER V

FIRST ORDER GREEN'S FUNCTION

The next term in the Neumann Series that needs to be calculated is the first order Green's function, which represents the transport of first generation fragments. Using the Neumann series solution given by equation (119), the first order Green's function is obtained by $\mathbf{G}^1 = (\mathbf{Q} \cdot \mathbf{L} \cdot \mathbf{\Xi}) \cdot \mathbf{G}^0$.

In this expression, the operator $\mathbf{Q}$ is a quadrature operator, $\mathbf{L}$ is the linear transport operator given by equation (116), $\mathbf{\Xi}$ is the fragmentation or collision operator given by equation (102), and $\mathbf{G}^0$ is the zero order Green's function operator.

When the flux on the right-hand side of the Volterra equation (103) is replaced by the primary flux, the two-term Neumann approximation

$$\begin{aligned} \phi_j(\mathbf{x}, \mathbf{\Omega}, E) &= \frac{P_j(\bar{E}_j)}{P_j(E)} \frac{\tilde{S}_j(\bar{E}_j)}{\tilde{S}_j(E)} F_j(\mathbf{x}', \mathbf{\Omega}, \bar{E}_j) \\ &+ \int_{\rho'}^{\rho} \frac{P_j(E'')}{P_j(E)} \frac{\tilde{S}_j(E'')}{\tilde{S}_j(E)} [\mathbf{\Xi} \cdot \mathbf{\Phi}^0]_j(\mathbf{x}'', \mathbf{\Omega}, E'') d\rho'', \end{aligned} \tag{185}$$

is obtained, in which $\mathbf{\Phi}^0$ is the primary flux vector and

$$\begin{aligned} [\mathbf{\Xi} \cdot \mathbf{\Phi}^0]_j(\mathbf{x}, \mathbf{\Omega}, E) &= \sum_{k>j}^{N} \int_E^{\infty} dH_1 \int_{4\pi} d\mathbf{\Omega}_1 \sigma_{jk}(\mathbf{\Omega}, \mathbf{\Omega}_1, E, H_1) \phi_k^0(\mathbf{x}, \mathbf{\Omega}_1, H_1) \\ &= \int_E^{\infty} dH_1 \int_{4\pi} d\mathbf{\Omega}_1 \sigma_{jm}(\mathbf{\Omega}, \mathbf{\Omega}_1, E, H_1) \phi_m^0(\mathbf{x}, \mathbf{\Omega}_1, H_1). \end{aligned} \tag{186}$$

The second term on the right-hand side of (185) represents the first generation fragment flux, which will be denoted by $\phi_j^1(\mathbf{x}, \mathbf{\Omega}, E)$, and is defined as

$$\phi_j^1(\mathbf{x}, \mathbf{\Omega}, E) = \int_{\rho'}^{\rho} \frac{P_j(E'')}{P_j(E)} \frac{\tilde{S}_j(E'')}{\tilde{S}_j(E)} [\mathbf{\Xi} \cdot \mathbf{\Phi}^0]_j(\mathbf{x}'', \mathbf{\Omega}, E'') d\rho''. \tag{187}$$

For notational convenience, an operator, $\mathbf{\Lambda}$, will be introduced. This operator represents the linear production density per unit path length of j type ions with energy E and direction $\mathbf{\Omega}$ at the point $\mathbf{x}$.

$$\mathbf{\Lambda}^1_{\jmath m}[\mathbf{x}, \mathbf{\Omega}, E] = \int_E^\infty dH_1 \int_{4\pi} d\mathbf{\Omega}_1 \sigma_{\jmath m}(\mathbf{\Omega}, \mathbf{\Omega}_1, E, H_1) \phi^0_m(\mathbf{x}, \mathbf{\Omega}_1, H_1). \quad (188)$$

Hence, the first generation flux can be expressed as

$$\phi^1_\jmath(\mathbf{x}, \mathbf{\Omega}, E) = \int_{\rho'}^{\rho} \frac{P_\jmath(E'')}{P_\jmath(E)} \frac{\tilde{S}_\jmath(E'')}{\tilde{S}_\jmath(E)} \mathbf{\Lambda}^1_{\jmath m}(\mathbf{x}'', \mathbf{\Omega}, E'') d\rho''. \quad (189)$$

Since numerical integration is computationally expensive, equation (189) will be evaluated by analytic approximations. As with the primary flux, $\mathbf{\Omega}$ will be described by spherical polar coordinates $(1, \gamma, \alpha)$ so that the components relative to the Cartesian coordinate system $OXYZ$ are given by equation (179).

A new Cartesian coordinate system, $O'X'Y'Z'$, is obtained by rotating the rectangular Cartesian coordinates, $OXYZ$, by α radians about the z-axis, followed by γ radians about the rotated y-axis. This allows us to write components of $\mathbf{\Omega}$ relative to the coordinate system $O'X'Y'Z'$ as

$$\mathbf{\Omega}' = \begin{pmatrix} \Omega'_1 \\ \Omega'_2 \\ \Omega'_3 \end{pmatrix} = \begin{pmatrix} 0 \\ 0 \\ 1 \end{pmatrix}. \quad (190)$$

This transformation can also be expressed in terms of rotation matrices, $R_y(\gamma)$ and $R_z(\alpha)$, by noting that

$$\mathbf{\Omega}' = R_{yz}\mathbf{\Omega} = R_y(\gamma) R_z(\alpha) \mathbf{\Omega}, \quad (191)$$

and

$$\mathbf{\Omega} = R^{-1}_{yz}\mathbf{\Omega}' = R_z(-\alpha) R_y(-\gamma) \mathbf{\Omega}', \quad (192)$$

where

$$R_y(\gamma) = \begin{pmatrix} \cos\gamma & 0 & -\sin\gamma \\ 0 & 1 & 0 \\ \sin\gamma & 0 & \cos\gamma \end{pmatrix}, \quad (193)$$

and

$$R_z(\alpha) = \begin{pmatrix} \cos\alpha & \sin\alpha & 0 \\ -\sin\alpha & \cos\alpha & 0 \\ 0 & 0 & 1 \end{pmatrix}. \tag{194}$$

Since the flux is a function of position as well as direction, it will be convenient to translate the coordinate system $O'X'Y'Z'$ so that its origin coincides with the point $\mathbf{x}$ in the target material as shown in figure 64. The components of $\mathbf{\Omega}_1$ relative to $O'X'Y'Z'$, can be expressed in terms of the spherical polar $(1, \theta, \beta)$ by

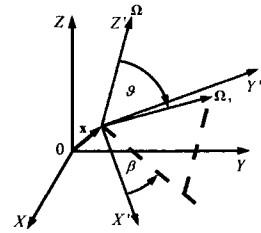

FIGURE 64: Coordinate Translation

$$\mathbf{\Omega}_1' = \begin{pmatrix} \Omega_{11}' \\ \Omega_{12}' \\ \Omega_{13}' \end{pmatrix} = \begin{pmatrix} \sin\theta\cos\beta \\ \sin\theta\sin\beta \\ \cos\theta \end{pmatrix}, \tag{195}$$

and relative to the original system $OXYZ$ by

$$\mathbf{\Omega}_1 = R_{yz}^{-1}\mathbf{\Omega}_1{}' = R_z(-\alpha)R_y(-\gamma)\mathbf{\Omega}_1' = \begin{pmatrix} \Omega_{11}(\theta,\beta) \\ \Omega_{12}(\theta,\beta) \\ \Omega_{13}(\theta,\beta). \end{pmatrix}, \tag{196}$$

where

$$\begin{aligned} \Omega_{11}(\theta,\beta) &= \cos\alpha\cos\gamma\sin\theta\cos\beta - \sin\alpha\sin\theta\sin\beta + \cos\alpha\sin\gamma\cos\theta \\ \Omega_{12}(\theta,\beta) &= \sin\alpha\cos\gamma\sin\theta\cos\beta + \cos\alpha\sin\theta\sin\beta + \sin\alpha\sin\gamma\cos\theta \\ \Omega_{13}(\theta,\beta) &= -\sin\gamma\sin\theta\cos\beta + \cos\gamma\cos\theta. \end{aligned} \tag{197}$$

Now recall (50) that the double differential cross section for the production of type j ions of energy E in the direction $\mathbf{\Omega}$ from type m ions of energy H_1 in the direction $\mathbf{\Omega}_1$ is given approximately by

$$\sigma_{jm}(\mathbf{\Omega}, \mathbf{\Omega}_1, E, H_1) = \sigma_{jm}(\theta, E, H_1) = \sigma_{jm}(H_1) f_E(E, H_1) f_\Omega(\theta, H_1), \tag{198}$$

and is independent of β. Then it becomes clear that the equation for the production density, $\mathbf{\Lambda}$, can be rewritten as

$$\begin{aligned}\mathbf{\Lambda}^1_{jm}[\mathbf{x},\mathbf{\Omega},E] &= \int_E^\infty dH_1 \int_0^\pi \sin\theta d\theta \int_0^{2\pi} d\beta \sigma_{jm}(H_1) f_E(E,H_1) \\ &\cdot f_\Omega(\theta,H_1)\phi^0_m[\mathbf{x},\mathbf{\Omega}_1(\theta,\beta),H_1]. \end{aligned} \tag{199}$$

For future reference, some additional notation that is needed in later subsections is now introduced. Let $\mathbf{x}'_1$ be the point where the ray through $\mathbf{x}$ in the direction $\mathbf{\Omega}_1$ first meets the boundary ∂V and let $\rho_1 = \mathbf{x}\cdot\mathbf{\Omega}_1$, and $\mathbf{x}^1_n = \mathbf{x} - \rho_1\mathbf{\Omega}_1$. Then $\mathbf{x} = \mathbf{x}^1_n + \rho_1\mathbf{\Omega}_1$, $\mathbf{x}'_1 = \mathbf{x}^1_n + \rho'_1\mathbf{\Omega}_1$, and $\mathbf{x} - \mathbf{x}'_1 = (\rho_1 - \rho'_1)\mathbf{\Omega}_1 = d_1(\theta,\beta)\mathbf{\Omega}_1$ as shown in figure 65.

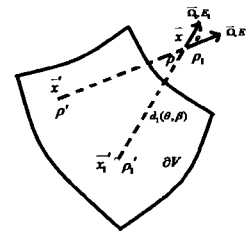

FIGURE 65: Surface

V.1 THE BROAD FIRST ORDER GREEN'S FUNCTION

Since the above analysis is applicable in the case of a broad Green's function boundary condition (129), it can be asserted that the broad first order Green's function is given by

$$G^1_{jm}(\mathbf{x},\mathbf{x}_0,\mathbf{\Omega},\mathbf{\Omega}_0,E,E_0) = \int_{\rho'}^{\rho} d\rho'' \frac{P_j(E'')}{P_j(E)} \frac{\tilde{S}_j(E'')}{\tilde{S}_j(E)} \mathbf{\Lambda}^1_{jm}[\mathbf{x}'',\mathbf{x}_0,\mathbf{\Omega},\mathbf{\Omega}_0,E'',E_0], \tag{200}$$

where

$$\begin{aligned}\mathbf{\Lambda}^1_{jm}[\mathbf{x},\mathbf{x}_0,\mathbf{\Omega},\mathbf{\Omega}_0,E,E_0] &= \int_E^\infty dH_1 \int_0^\pi \sin\theta d\theta \int_0^{2\pi} d\beta \sigma_{jm}(H_1) f_E(E,H_1) \\ &\cdot f_\Omega(\theta,H_1) G^b_{mm}(\mathbf{x},\mathbf{x}_0,\mathbf{\Omega}_1(\theta,\beta),\mathbf{\Omega}_0,H_1,E_0), \end{aligned} \tag{201}$$

and G^b_{mm} is the broad zero order Green's function given by equation (138). It follows that

$$\begin{aligned}\mathbf{\Lambda}^1_{jm}(\mathbf{x},\mathbf{x}_0,\mathbf{\Omega},\mathbf{\Omega}_0,E,E_0) &= \int_E^\infty dH_1 \int_0^{\pi/2} d\theta \sigma_{jm}(H_1) f_E(E,H_1)\sin(\theta) f_{\mathbf{\Omega}}(\theta,H_1) \\ &\cdot \int_0^{2\pi} d\beta \frac{H[-\mathbf{\Omega}_1(\theta,\beta)\cdot\mathbf{n}(\mathbf{x}')]}{2\pi K_x |\partial_u \mathbf{x}' \times \partial_v \mathbf{x}'| s_x^2} \\ &\cdot \exp\left\{-\frac{(u'-u_0)^2+(v'-v_0)^2}{2s_x^2}\right\} \\ &\cdot \frac{1}{\sqrt{2\pi}K_{\mathbf{\Omega}} s_{\mathbf{\Omega}}} \exp\left\{\frac{(1-\mathbf{\Omega}_1(\theta,\beta)\cdot\mathbf{\Omega}_0)^2}{2s_{\mathbf{\Omega}}^2}\right\} \\ &\cdot G^b_{mm}(d_1(\theta,\beta),0,H_1,E_0). \end{aligned} \tag{202}$$

It should now be recalled (45) that

$$\sin\theta f_{\mathbf{\Omega}}(\theta,E_1) = H[\pi/2-\theta]\frac{\sin(\theta)\cos(\theta)}{2\pi\omega^2}\exp\left(-\frac{\sin^2\theta}{2\omega^2}\right), \tag{203}$$

where $\omega = \frac{\sigma_\parallel}{\gamma_L \beta_L m_p}$ is very small. It follows that $\sin\theta f_\Omega(\theta,E_1)$ is sharply peaked at about $\theta \approx \omega \approx 0$ for heavy ions. Hence, only primaries approaching $\mathbf{x}$ from within a cone of very small angle about $\mathbf{\Omega}$ will contribute significantly to the first generation secondaries. Since the cone is very slender, we can make the simplifying assumption that $\mathbf{\Omega}(\theta,\beta) \approx \mathbf{\Omega}$ and that the distance from its apex $\mathbf{x}$ to the boundary ∂V is independent of the angle β giving $d_1(\theta,\beta) \approx d_1(\theta)$, which is a slowly varying function of θ. It should be noted that this will need to be relaxed for light ions. This yields

$$
\begin{aligned}
\Lambda^1_{jm}(\mathbf{x},\mathbf{x}_0,\mathbf{\Omega},\mathbf{\Omega}_0,E,E_0) &= \frac{H[-\mathbf{\Omega}\cdot\mathbf{n}(\mathbf{x}')]}{2\pi K_x|\partial_u\mathbf{x}'\times\partial_v\mathbf{x}'|s_x^2}\exp\left\{-\frac{(u'-u_0)^2+(v'-v_0)^2}{2s_x^2}\right\} \\
&\quad\cdot\frac{1}{\sqrt{2\pi}K_{\mathbf{\Omega}}s_{\mathbf{\Omega}}}\exp\left\{\frac{(1-\mathbf{\Omega}\cdot\mathbf{\Omega_0})^2}{2s_{\mathbf{\Omega}}^2}\right\} \\
&\quad\cdot\int_E^\infty dH_1\sigma_{jm}(H_1)f_E(E,H_1)2\pi G^b_{mm}(d_1(\omega),0,H_1,E_0) \\
&\quad\cdot\int_0^{\pi/2}d\theta\sin(\theta)f_{\mathbf{\Omega}}(\theta,H_1) \\
&\approx \frac{H[-\mathbf{\Omega}\cdot\mathbf{n}(\mathbf{x}')]}{K_x|\partial_u\mathbf{x}'\times\partial_v\mathbf{x}'|s_x^2}\exp\left\{-\frac{(u'-u_0)^2+(v'-v_0)^2}{2s_x^2}\right\} \\
&\quad\cdot\frac{1}{\sqrt{2\pi}K_{\mathbf{\Omega}}s_{\mathbf{\Omega}}}\exp\left\{\frac{(1-\mathbf{\Omega}\cdot\mathbf{\Omega}_0)^2}{2s_{\mathbf{\Omega}}^2}\right\} \\
&\quad\cdot\int_E^\infty dH_1\sigma_{jm}(H_1)f_E(E,H_1) \\
&\quad\cdot G^b_{mm}(\rho-\rho',0,H_1,E_0), \qquad (204)
\end{aligned}
$$

where in the last approximation, use has been made of the results $\omega\approx 0$ and $d_1(\omega)\approx d_1(0)=\rho-\rho'$.

Next, from [20], it is seen that

$$
\begin{aligned}
G^b_{mm}(\rho-\rho',0,H_1,E_0) &= \frac{P_m(\bar{E}_m)}{P_m(H_1)}\frac{1}{\sqrt{2\pi}s^b_m(\rho-\rho',E_0)} \\
&\quad\cdot\exp\left(-\frac{[H_1-\hat{E}_m(\rho-\rho',E_0)]^2}{2s^b_m(\rho-\rho',E_0)^2}\right), \qquad (205)
\end{aligned}
$$

and from the approximation of $f_E(E,H_1)$ (given by equation (40)), let $E_{jm}=E_{jm}(H_1)=E_s(H_1)$ be the collision energy downshift for type j fragments produced from type m projectiles and $\epsilon_{jm}=\epsilon_{jm}(H_1)=\sigma_{\|}\gamma_{L}(H_1)\beta_{L}(H_1)$ be the corresponding width. These are both slowly varying functions of H_1. Therefore, it is possible to make the approximation,

$$
\begin{aligned}
&\int_E^\infty dH_1 \sigma_{jm}(H_1) f_E(E,H_1) G^b_{mm}(\rho-\rho',0,H_1,E_0) \\
&\approx \int_{-\infty}^\infty \frac{\sigma_{jm}(H_1)}{\sqrt{2\pi}\epsilon_{jm}} \exp\left\{-\frac{[H_1-E_{jm}(H_1)-E]^2}{2\epsilon_{jm}^2}\right\} \\
&\cdot \frac{P_m(\bar{E}_m)}{P_m(H_1)} \frac{1}{\sqrt{2\pi}s^b_m(\rho-\rho',E_0)} \exp\left(-\frac{[H_1-\hat{E}_m(\rho-\rho',E_0)]^2}{2s^b_m(\rho-\rho',E_0)^2}\right) dH_1 \\
&\approx \frac{\sigma_{jm}[\hat{E}_m(\rho-\rho',E_0)]P_m(E_0)}{P_m[\hat{E}_m(\rho-\rho',E_0)]} \int_{-\infty}^\infty \frac{1}{\sqrt{2\pi}(\sigma_{\|}\gamma_{_L}(\hat{E}_m)\beta_{_L}(\hat{E}_m))} \\
&\cdot \exp\left\{-\frac{[H_1-E_{jm}(\hat{E}_m)-E]^2}{2\epsilon_{jm}^2}\right\} \\
&\cdot \frac{1}{\sqrt{2\pi}s^b_m(\rho-\rho',E_0)} \exp\left(-\frac{[H_1-\hat{E}_m(\rho-\rho',E_0)]^2}{2s^b_m(\rho-\rho',E_0)^2}\right) dH_1 \\
&= \frac{P_m(E_0)}{P_m(\hat{E}_m)} \frac{\sigma_{jm}(\hat{E}_m)}{\sqrt{2\pi}s^1_m(\rho-\rho',E_0)} \exp\left(-\frac{[\hat{E}_m-E_{jm}(\hat{E}_m)-E]^2}{2s^1_m(\rho-\rho',E_0)^2}\right), \qquad (206)
\end{aligned}
$$

where

$$
s^1_m(\rho''-\rho',E_0)^2 = s^b_m(\rho''-\rho',E_0)^2 + \epsilon^2_{jm}. \qquad (207)
$$

It now follows that

$$
\begin{aligned}
\mathbf{\Lambda}^1_{jm}(\mathbf{x},\mathbf{x}_0,\mathbf{\Omega},\mathbf{\Omega}_0,E,E_0) \;\approx\; & \frac{H[-\mathbf{\Omega}\cdot\mathbf{n}(\mathbf{x}')]}{K_x|\partial_u\mathbf{x}'\times\partial_v\mathbf{x}'|s_x^2} \exp\left\{-\frac{(u'-u_0)^2+(v'-v_0)^2}{2s_x^2}\right\} \\
& \cdot \frac{1}{\sqrt{2\pi}K_{\mathbf{\Omega}}s_{\mathbf{\Omega}}} \exp\left\{\frac{(1-\mathbf{\Omega}\cdot\mathbf{\Omega}_0)^2}{2s^2_{\mathbf{\Omega}}}\right\} \frac{P_m(E_0)}{P_m(\hat{E}_m)} \\
& \cdot \frac{\sigma_{jm}(\hat{E}_m)}{\sqrt{2\pi}s^1_m(\rho-\rho',E_0)} \\
& \cdot \exp\left(-\frac{[\hat{E}_m-E_{jm}(\hat{E}_m)-E]^2}{2s^1_m(\rho-\rho',E_0)^2}\right), \qquad (208)
\end{aligned}
$$

and hence that the broad first order Green's function (200) is given by

$$
\begin{aligned}
G^1_{\jmath m}(\mathbf{x},\mathbf{x}_0,\mathbf{\Omega},\mathbf{\Omega}_0,E,E_0) \approx\ & \frac{H[-\mathbf{\Omega}\cdot\mathbf{n}(\mathbf{x}')]}{K_x|\partial_u\mathbf{x}'\times\partial_v\mathbf{x}'|s_x^2}\exp\left\{-\frac{(u'-u_0)^2+(v'-v_0)^2}{2s_x^2}\right\} \\
& \cdot\frac{1}{\sqrt{2\pi}K_{\mathbf{\Omega}}s_{\mathbf{\Omega}}}\exp\left\{\frac{(1-\mathbf{\Omega}\cdot\mathbf{\Omega}_0)^2}{2s_{\mathbf{\Omega}}^2}\right\} \\
& \cdot\int_{\rho'}^{\rho}\frac{P_\jmath(E'')}{P_\jmath(E)}\frac{\tilde{S}_\jmath(E'')}{\tilde{S}_\jmath(E)}\frac{P_m(E_0)}{P_m(\hat{E}_m)}\frac{\sigma_{\jmath m}(\hat{E}_m)}{\sqrt{2\pi}s_m^1(\rho''-\rho',E_0)} \\
& \cdot\exp\left(-\frac{[E''+E_{\jmath m}(\hat{E}_m)-\hat{E}_m]^2}{2s_m^1(\rho''-\rho',E_0)^2}\right)d\rho'', \qquad (209)
\end{aligned}
$$

where $s_m^1(\rho''-\rho',E_0)^2$ was defined by equation (207), $E''=\bar{E}_\jmath(\rho-\rho'',E)$, and $\hat{E}_m=\hat{E}_m(\rho-\rho'',E)$. The remaining integral

$$
\begin{aligned}
J =\ & \int_{\rho'}^{\rho}\frac{P_\jmath(E'')}{P_\jmath(E)}\frac{\tilde{S}_\jmath(E'')}{\tilde{S}_\jmath(E)}\frac{P_m(E_0)}{P_m(\hat{E}_m)}\frac{\sigma_{\jmath m}(\hat{E}_m)}{\sqrt{2\pi}s_m^1(\rho''-\rho',E_0)} \\
& \cdot\exp\left(-\frac{[E''+E_{\jmath m}(\hat{E}_m)-\hat{E}_m]^2}{2s_m^1(\rho''-\rho',E_0)^2}\right)d\rho'', \qquad (210)
\end{aligned}
$$

can be approximated by two methods, which are now discussed.

Define

$$
\begin{aligned}
C_{\jmath m}(\rho'') &= C_{\jmath m}(\rho,\rho',E,E_0;\rho'') \\
&= \frac{P_\jmath(E'')}{P_\jmath(E)}\frac{\tilde{S}_\jmath(E'')}{\tilde{S}_\jmath(E)}\frac{P_m(E_0)}{P_m(\hat{E}_m)}\sigma_{\jmath m}(\hat{E}_m), \qquad (211)
\end{aligned}
$$

and

$$
\begin{aligned}
g_{\jmath m}(\rho'') &= g_{\jmath m}(\rho,\rho',E,E_0;\rho'') \\
&= \hat{E}_m(\rho''-\rho',E_0)-\bar{E}_\jmath(\rho-\rho'',E)-E_{\jmath m}(\hat{E}_m). \qquad (212)
\end{aligned}
$$

Then the integral J can be expressed in the form

$$
J = \int_{\rho'}^{\rho}\frac{C_{\jmath m}(\rho'')}{\sqrt{2\pi}s_m^1(\rho''-\rho',E_0)}\exp\left(-\frac{g_{\jmath m}(\rho'')^2}{2s_m^1(\rho''-\rho',E_0)^2}\right)d\rho''. \qquad (213)
$$

The exponential term in this equation achieves its maximum at some point $\rho''=$

ρ^*, where $g_{jm}(\rho^*) = 0$. Additionally, $s_m^1(\rho'' - \rho', E_0)$ is a slowly varying function of ρ'' and by Taylor's theorem,

$$g_{jm}(\rho'') \approx g'_{jm}(\rho^*)(\rho'' - \rho^*), \tag{214}$$

it is possible to make the approximation

$$J \approx \int_{\rho'}^{\rho} \frac{C_{jm}(\rho'')}{\sqrt{2\pi} s_m^* g'_{jm}(\rho^*)} \exp\left(-\frac{(\rho'' - \rho^*)^2}{2(s_m^*)^2}\right) d\rho'', \tag{215}$$

where

$$s_m^* = \frac{s_m^1(\rho^*)}{g'_{jm}(\rho^*)} = \frac{s_m^1(\rho^* - \rho', E_0)}{g'_{jm}(\rho^*)}. \tag{216}$$

Approximation 1

In the first approximation, it is assumed that $C_{jm}(\rho'')$ is a slowly varying function of ρ'', in which case

$$\begin{aligned} J &\approx \frac{C_{jm}(\rho^*)}{g'_{jm}(\rho^*)} \int_{\rho'}^{\rho} \frac{1}{\sqrt{2\pi} s_m^*} \exp\left(-\frac{(\rho'' - \rho^*)^2}{2(s_m^*)^2}\right) d\rho'' \\ &= \frac{C_{jm}(\rho^*)}{2g'_{jm}(\rho^*)} \left\{ \operatorname{erf}\left[\frac{g_{jm}(\rho)}{\sqrt{2\pi} s_m^1(\rho^*)}\right] - \operatorname{erf}\left[\frac{g_{jm}(\rho')}{\sqrt{2\pi} s_m^1(\rho^*)}\right] \right\}, \end{aligned} \tag{217}$$

and the broad first order Green's function is approximated by

$$\begin{aligned} G_{jm}^1(\mathbf{x}, \mathbf{x_0}, \mathbf{\Omega}, \mathbf{\Omega_0}, E, E_0) \approx\ & \frac{H[-\mathbf{\Omega} \cdot \mathbf{n}(\mathbf{x}')]}{(2\pi)^{3/2} K_x K_{\mathbf{\Omega}} |\partial_u \mathbf{x}' \times \partial_v \mathbf{x}'| s_x^2 s_{\mathbf{\Omega}}} \exp\left\{-\frac{(1 - \mathbf{\Omega} \cdot \mathbf{\Omega_0})^2}{2s_{\mathbf{\Omega}}^2}\right\} \\ & \cdot \exp\left\{-\frac{(u' - u_0)^2 + (v' - v_0)^2}{2s_x^2}\right\} \frac{C_{jm}(\rho^*)}{2g'_{jm}(\rho^*)} \\ & \cdot \left\{ \operatorname{erf}\left(\frac{g_{jm}(\rho)}{\sqrt{2} s_m^1(\rho^*)}\right) - \operatorname{erf}\left(\frac{g_{jm}(\rho')}{\sqrt{2} s_m^1(\rho^*)}\right) \right\}. \end{aligned} \tag{218}$$

Approximation 2

In the second approximation, Taylor's theorem is used to express $C_{jm}(\rho'')$ in the

form

$$C_{jm}(\rho'') \approx C_{jm}(\rho^*) + C'_{jm}(\rho^*)(\rho'' - \rho^*), \tag{219}$$

in which case

$$\begin{aligned} J &\approx \frac{C_{jm}(\rho^*)}{g'_{jm}(\rho^*)} \int_{\rho'}^{\rho} \frac{1}{\sqrt{2\pi} s_m^*} \exp\left(-\frac{(\rho'' - \rho^*)^2}{2(s_m^*)^2}\right) d\rho'' \\ &\quad + \frac{C'_{jm}(\rho^*)}{g'_{jm}(\rho^*)} \int_{\rho'}^{\rho} \frac{(\rho'' - \rho^*)}{\sqrt{2\pi} s_m^*} \exp\left(-\frac{(\rho'' - \rho^*)^2}{2(s_m^*)^2}\right) d\rho'' \\ &= \frac{C_{jm}(\rho^*)}{2g'_{jm}(\rho^*)} \left\{ \operatorname{erf}\left[\frac{g_{jm}(\rho)}{\sqrt{2} s_m^1(\rho^*)}\right] - \operatorname{erf}\left[\frac{g_{jm}(\rho')}{\sqrt{2} s_m^1(\rho^*)}\right] \right\} \\ &\quad - \frac{C'_{jm}(\rho^*) s_m^1(\rho^*)}{\sqrt{2\pi} g'_{jm}(\rho^*)^2} \left\{ \exp\left[-\frac{g_{jm}(\rho)^2}{2 s_m^1(\rho^*)^2}\right] - \exp\left[-\frac{g_{jm}(\rho')^2}{2 s_m^1(\rho^*)^2}\right] \right\}. \end{aligned} \tag{220}$$

The corresponding broad first order Green's function is then given by

$$\begin{aligned} G^1_{jm}(\mathbf{x}, \mathbf{x}_0, \mathbf{\Omega}, \mathbf{\Omega}_0, E, E_0) &\approx \frac{H[-\mathbf{\Omega} \cdot \mathbf{n}(\mathbf{x}')]}{(2\pi)^{3/2} K_x K_{\mathbf{\Omega}} |\partial_u \mathbf{x}' \times \partial_v \mathbf{x}'| s_x^2 s_{\mathbf{\Omega}}} \\ &\quad \cdot \exp\left\{-\frac{(u' - u_0)^2 + (v' - v_0)^2}{2 s_x^2}\right\} \\ &\quad \cdot \exp\left\{-\frac{(1 - \mathbf{\Omega} \cdot \mathbf{\Omega_0})^2}{2 s_{\mathbf{\Omega}}^2}\right\} \\ &\quad \cdot \left[\frac{C_{jm}(\rho^*)}{2 g'_{jm}(\rho^*)} \left\{ \operatorname{erf}\left(\frac{g_{jm}(\rho)}{\sqrt{2} s_m^1(\rho^*)}\right) - \operatorname{erf}\left(\frac{g_{jm}(\rho')}{\sqrt{2} s_m^1(\rho^*)}\right) \right\} \right. \\ &\quad - \frac{C'_{jm}(\rho^*) s_m^1(\rho^*)}{\sqrt{2\pi} g'_{jm}(\rho^*)^2} \\ &\quad \left. \cdot \left\{ \exp\left(-\frac{g_{jm}(\rho)^2}{2 s_m^1(\rho^*)^2}\right) - \exp\left(-\frac{g_{jm}(\rho')^2}{2 s_m^1(\rho^*)^2}\right) \right\} \right]. \end{aligned} \tag{221}$$

V.2 THE FIRST ORDER GREEN'S FUNCTION

Since the first order Green's function is the special case corresponding to the boundary condition (104), it is easily found by taking the limit of the broad first order Green's function as s_x, $s_{\mathbf{\Omega}}$, $s_E \to 0$. For approximation 1, this yields

$$G^1_{\jmath m}(\mathbf{x},\mathbf{x}_0,\boldsymbol{\Omega},\boldsymbol{\Omega}_0,E,E_0) \approx \frac{H[-\boldsymbol{\Omega}\cdot\mathbf{n}(\mathbf{x}')]}{2\pi}\delta(1-\boldsymbol{\Omega}\cdot\boldsymbol{\Omega}_0)\overline{\delta}(\mathbf{x}'-\mathbf{x}_0)\frac{C_{\jmath m}(\rho^*)}{2g'_{\jmath m}(\rho^*)} \cdot\left\{\operatorname{erf}\left(\frac{g_{\jmath m}(\rho)}{\sqrt{2}s^1_m(\rho^*)}\right)-\operatorname{erf}\left(\frac{g_{\jmath m}(\rho')}{\sqrt{2}s^1_m(\rho^*)}\right)\right\}, \quad (222)$$

and for approximation 2, it yields

$$\begin{aligned} G^1_{\jmath m}(\mathbf{x},\mathbf{x}_0,\boldsymbol{\Omega},\boldsymbol{\Omega}_0,E,E_0) \approx{}& \frac{H[-\boldsymbol{\Omega}\cdot\mathbf{n}(\mathbf{x}')]}{2\pi}\delta(1-\boldsymbol{\Omega}\cdot\boldsymbol{\Omega}_0)\overline{\delta}(\mathbf{x}'-\mathbf{x}_0) \\ &\cdot\left(\frac{C_{\jmath m}(\rho^*)}{2g'_{\jmath m}(\rho^*)}\left\{\operatorname{erf}\left(\frac{g_{\jmath m}(\rho)}{\sqrt{2}s^1_m(\rho^*)}\right)-\operatorname{erf}\left(\frac{g_{\jmath m}(\rho')}{\sqrt{2}s^1_m(\rho^*)}\right)\right\}\right. \\ &-\frac{C'_{\jmath m}(\rho^*)s^1_m(\rho^*)}{\sqrt{2\pi}g'_{\jmath m}(\rho^*)^2} \\ &\left.\cdot\left\{\exp\left(-\frac{g_{\jmath m}(\rho)^2}{2s^1_m(\rho^*)^2}\right)-\exp\left(-\frac{g_{\jmath m}(\rho')^2}{2s^1_m(\rho^*)^2}\right)\right\}\right), \quad (223) \end{aligned}$$

where

$$s^1_m(\rho''-\rho',E_0)^2 = s_m(\rho''-\rho',E_0)^2+\epsilon^2_{\jmath m}. \quad (224)$$

V.3 ION BEAM SPECTRUM

The broad Green's function finds application in the modeling of ion beam experiments of the type used to analyze the shielding requirements for space missions. An example is therefore presented to illustrate the first generation fragment flux in an aluminum (^{27}Al) half-space $z \geq 0$ with ion beam type boundary conditions (129). The projectile beam is assumed to have mean direction $\boldsymbol{\Omega}_0 = (\frac{1}{\sqrt{2}}, 0, \frac{1}{\sqrt{2}})$ and to consist of iron (^{56}Fe) with mean energy 1000 MeV/amu and spreads $s_E = 30$ (MeV/amu), $s_{\boldsymbol{\Omega}} = 45$ (Deg), $s_x = 1$. Since the Jacobian in this case is $|\partial_u\mathbf{x}' \times \partial_v\mathbf{x}'| = 1$, equation (221) shows that the first generation fragment flux is given by

$$\phi^1_{jm}(\mathbf{x},\mathbf{\Omega},E) = \frac{H[-\mathbf{\Omega}\cdot\mathbf{n}(\mathbf{x}')]}{2\pi s_x^2 K_x}\exp\left\{-\frac{(u'-u_0)^2+(v'-v_0)^2}{2s_x^2}\right\}$$
$$\cdot\frac{1}{\sqrt{2\pi}s_{\mathbf{\Omega}}K_{\mathbf{\Omega}}}\exp\left(-\frac{(1-\mathbf{\Omega}\cdot\mathbf{\Omega}_0)^2}{2s_{\mathbf{\Omega}}^2}\right)\left(\frac{C_{jm}(\rho^*)}{2g'_{jm}(\rho^*)}\right.$$
$$\cdot\left\{\mathrm{erf}\left(\frac{g_{jm}(\rho)}{\sqrt{2}s^1_m(\rho^*)}\right)-\mathrm{erf}\left(\frac{g_{jm}(\rho')}{\sqrt{2}s^1_m(\rho^*)}\right)\right\}-\frac{C'_{jm}(\rho^*)s^1_m(\rho^*)}{\sqrt{2\pi}g'_{jm}(\rho^*)^2}$$
$$\left.\cdot\left\{\exp\left(-\frac{g_{jm}(\rho)^2}{2s^1_m(\rho^*)^2}\right)-\exp\left(-\frac{g_{jm}(\rho')^2}{2s^1_m(\rho^*)^2}\right)\right\}\right). \qquad (225)$$

In the following figure shown below, figure 66, the first generation oxygen (^{16}O) fragment flux is plotted as a function of inclination angle, γ (Deg), and energy (MeV/amu) at depths $z = 2, 5$, and 15 g/cm^2 of aluminum (^{27}Al). From this figure, it is seen that the fragment flux peaks around 5 g/cm^2. Beyond that, the energy spread increases and the direction is sharply peaked around the mean initial direction of the projectile.

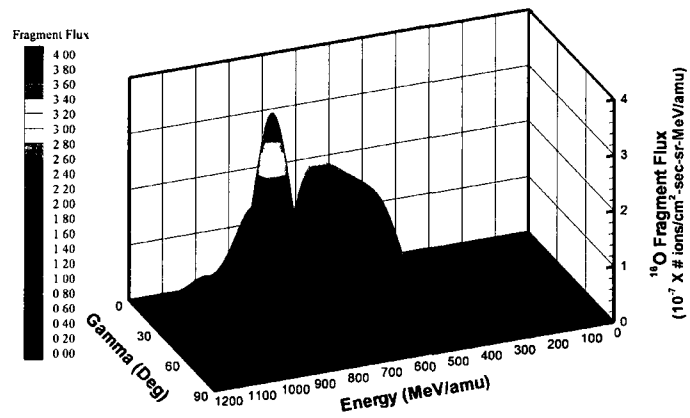

FIGURE 66: The first generation ^{16}O fragment flux at depths (from left to right) $z = 2, 5$, and 15 g/cm^2 with $\alpha = 0$ Deg.

For consideration of other target geometries, such as a sphere or cylinder, the surface Jacobian, $|\partial_u \mathbf{x}' \times \partial_v \mathbf{x}'|$, needs to be calculated and the singular points need to be considered as was done for the zero order Green's function.

V.4 UNIFORM ISOTROPIC BOUNDARY CONDITIONS

For the special case in which the boundary flux is uniform, isotropic, and has a Gaussian energy profile, the first generation flux is obtained by integrating equation (221) over all boundary points, $\mathbf{x}_0$, and all directions, $\mathbf{\Omega}_0$. This yields the result

$$\begin{aligned}\phi_j^1(\mathbf{x},\mathbf{\Omega},E) &= \frac{C_{jm}(\rho^*)}{2g'_{jm}(\rho^*)}\left\{\operatorname{erf}\left(\frac{g_{jm}(\rho)}{\sqrt{2}s_m^1(\rho^*)}\right)-\operatorname{erf}\left(\frac{g_{jm}(\rho')}{\sqrt{2}s_m^1(\rho^*)}\right)\right\}-\frac{C'_{jm}(\rho^*)s_m^1(\rho^*)}{\sqrt{2\pi}g'_{jm}(\rho^*)^2}\\ &\quad\cdot\left\{\exp\left(-\frac{g_{jm}(\rho)^2}{2s_m^1(\rho^*)^2}\right)-\exp\left(-\frac{g_{jm}(\rho')^2}{2s_m^1(\rho^*)^2}\right)\right\}. \qquad (226)\end{aligned}$$

This result can also be obtained directly from the uniform isotropic boundary condition (146) by means of the techniques used in section V.1, but the computations are omitted in the interest of brevity.

V.4.1 First Generation Flux in a Half-space with a Uniform Isotropic Boundary Condition and a Gaussian Energy Profile

For illustrative purposes, an aluminum (^{27}Al) half-space is considered as the target material of interest. The first three figures, figures 67-69, show the first generation oxygen (^{16}O) fragment flux as a function of inclination angle, γ (Deg), and energy (MeV/amu) at depths $z = 5, 10$, and 15 g/cm^2 of aluminum (^{27}Al) for an iron (^{56}Fe) projectile with a mean energy of 1000 MeV/amu and spread $s_E = 30$ (MeV/amu).

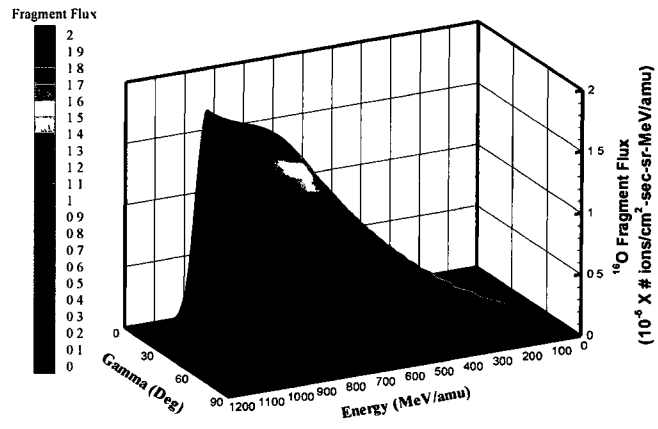

FIGURE 67: The first generation ^{16}O fragment flux at depth $z = 5$ g/cm^2 with $\alpha = 0$ Deg.

In the previous figure, the number of fragments are increasing with depth until approximately 80 degrees where a large decrease with depth occurs as the stopping range of the particle is approached. Close to the boundary, the flux of fragments will be low, which is why there is still an increase in the flux at a relatively shallow depth. These fragments will accumulate as the depth increases and will eventually peak.

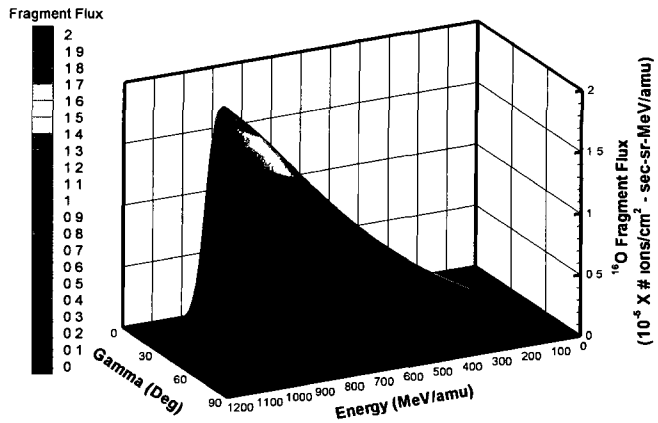

FIGURE 68: The first generation ^{16}O fragment flux at depth $z = 10$ g/cm^2 with $\alpha = 0$ Deg.

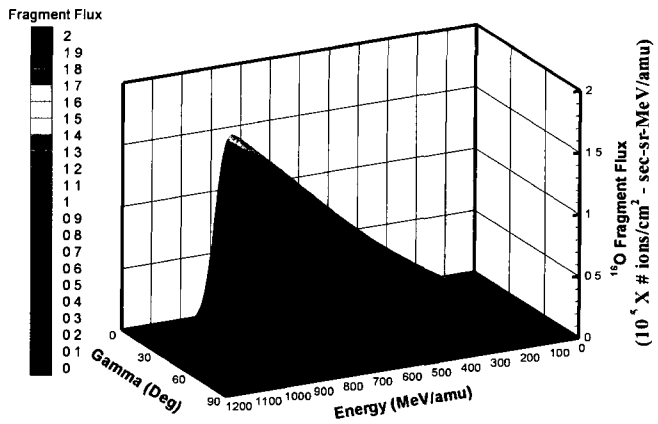

FIGURE 69: The first generation ^{16}O fragment flux at depth $z = 15$ g/cm^2 with $\alpha = 0$ Deg.

Figures 68 and 69 show that with increasing depth, the number of fragments decrease as the stopping range is approached.

As a verification of the approximations used, the first generation fragment flux was computed by evaluating the integrals numerically using a simple trapezoidal method. A comparison was then made between the numerical results and those

obtained by analytical approximations. This comparison is shown in figures 70 and 71, which exhibit the oxygen (^{16}O) fragment flux at depth $z = 10$ g/cm^2. Figure 70 shows the variation of the fragment flux with inclination angle,γ (Deg), for several energy values (MeV/amu) and figure 71 shows the variation of the fragment flux with energy (MeV/amu) for several values of the inclination angle, γ (Deg). Note that there is good agreement between the results, indicating that the approximations used are accurate.

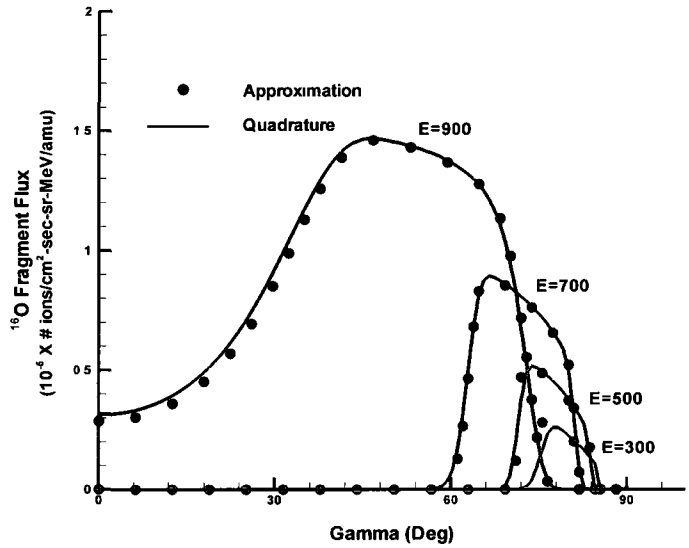

FIGURE 70: A comparison between the numerical and approximate first generation ^{16}O fragment fluxes at depth $z = 10$ g/cm^2 for several energies (MeV/amu).

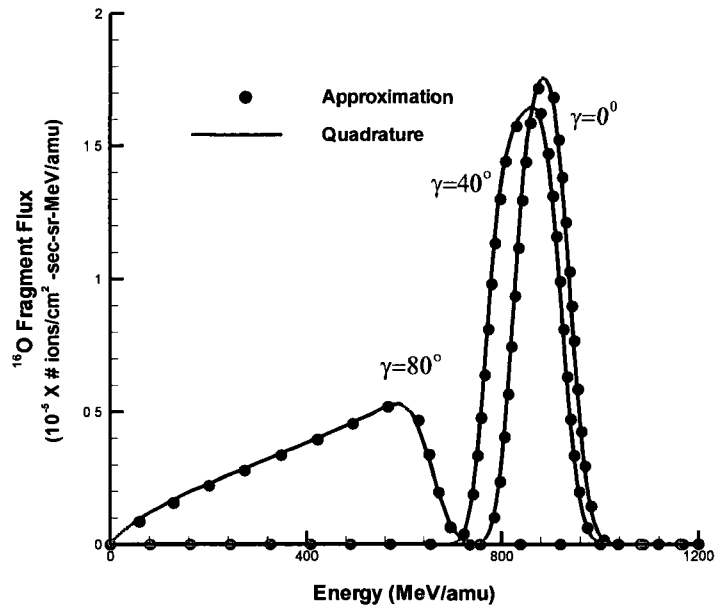

FIGURE 71: A comparison between the numerical and approximate first generation ^{16}O fragment fluxes at depth $z = 10$ g/cm^2 for several inclination angles (Deg).

The approximation in equation (226) can be used to calculate the fragment flux of any heavy ion. However, even with light ions, such as lithium (^{7}Li), there is still good agreement. Figures 72 - 74 show the first generation lithium (^{7}Li) fragment flux as a function of inclination angle, γ (Deg), and energy at depths $z = 5, 10$, and 15 g/cm^2 of aluminum (^{27}Al) with an 1000 MeV/amu iron (^{56}Fe) projectile. Consistent with the figures for oxygen (^{16}O), these figures show that at a depth of $z = 5$ g/cm^2, the number of fragments are increasing with depth until approximately 80 degrees where a large decrease with depth occurs as the stopping range of the ion is approached.

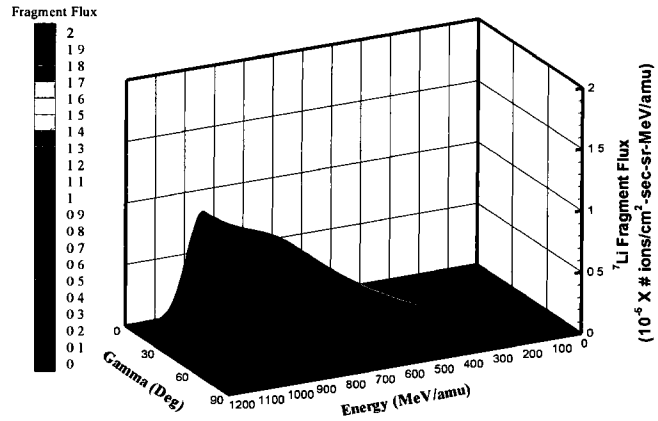

FIGURE 72: The first generation ^{7}Li fragment flux at depth $z = 5$ g/cm^2 with $\alpha = 0$ Deg.

Close to the boundary, the flux of fragments produced will be low, which is why there is still an increase in fragments at a relatively shallow depth.

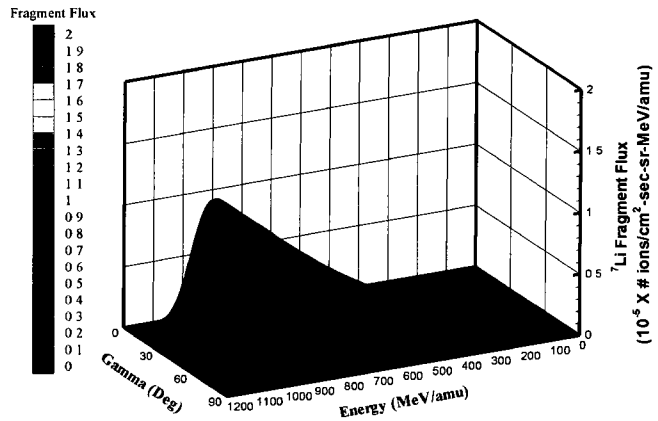

FIGURE 73: The first generation ^{7}Li fragment flux at depth $z = 10$ g/cm^2 with $\alpha = 0$ Deg.

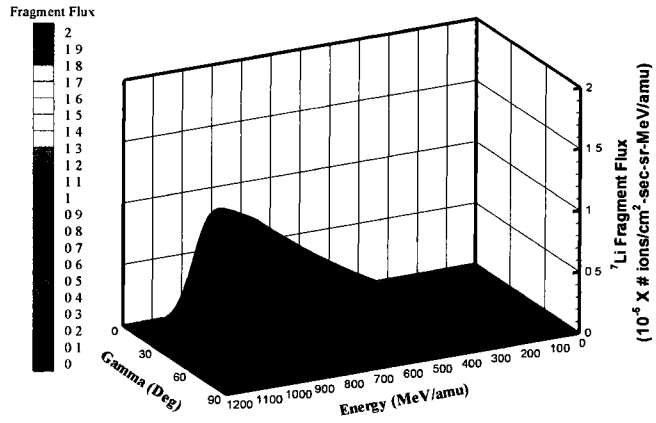

FIGURE 74: The first generation ^{7}Li fragment flux at depth $z = 15$ g/cm^2 with $\alpha = 0$ Deg.

Figures 73 and 74 show that with increasing depth, the number of fragments decrease as the stopping range is approached.

V.4.2 First Generation Flux in a Circular Cylinder with a Uniform Isotropic Boundary Condition and a Gaussian Energy Profile

For another simple geometry, consider a solid aluminum (^{27}Al) cylinder occupying the region $x^2+y^2 \leq 16^2$, $0 \leq z \leq 36$ to be the target. The boundary will be irradiated by a uniform isotropic beam of iron (^{56}Fe) ions with mean energy $E_0 = 1000$ MeV/amu and energy spread $s_E = 10$ MeV/amu. In the figures to follow, figures 75-78, the oxygen (^{16}O) fragment flux is represented as a function of inclination angle, γ (Deg), and energy E (MeV/amu). Various values of α (Deg) and several target points within the material are tested.

These figures illustrate the variation of the fragment flux with the distance that the ion has traveled into the material. The contour of the target material is evident within these figures.

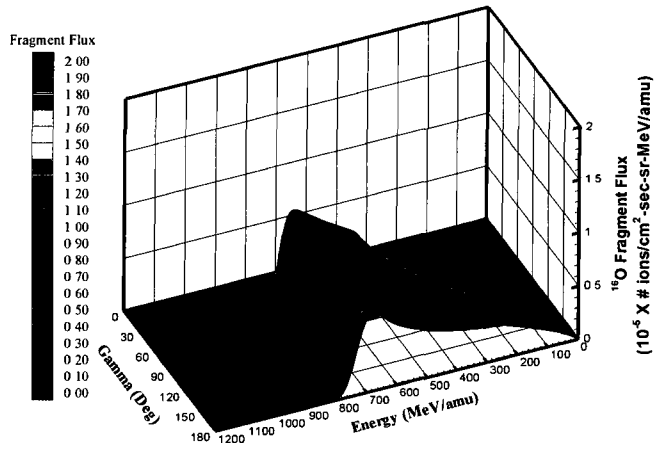

FIGURE 75: The first generation ^{16}O fragment flux at (0,0,0) with $\alpha = 0$ Deg.

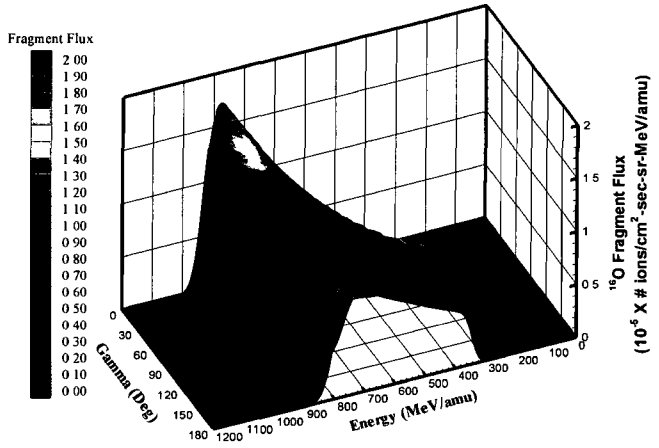

FIGURE 76: The first generation ^{16}O fragment flux at (14,0,9) with $\alpha = 0$ Deg.

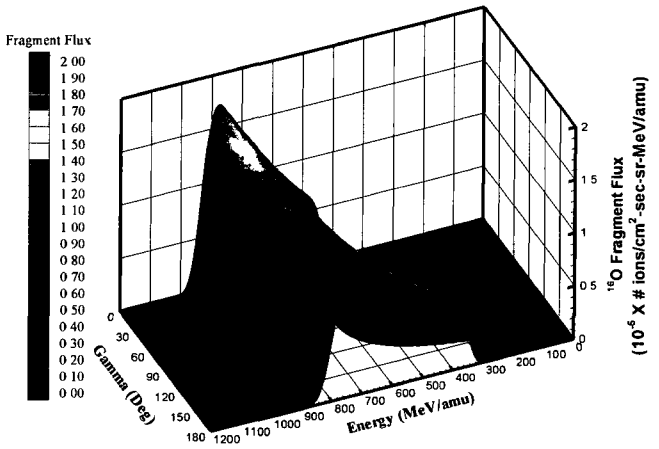

FIGURE 77: The first generation ^{16}O fragment flux at (14,0,9) with $\alpha = 90$ Deg.

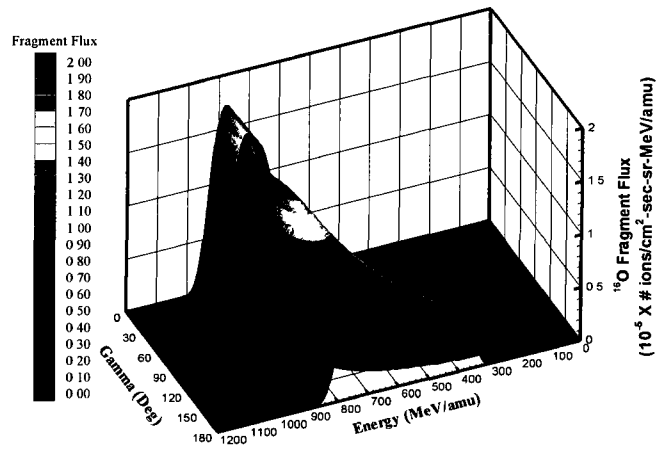

FIGURE 78: The first generation ^{16}O fragment flux at (14,0,9) with $\alpha = 180$ Deg.

V.5 GCR BOUNDARY CONDITION

From previous analysis, it has been shown that the primary flux for a GCR energy spectrum is given by equation (158). The production density is therefore given by

$$\begin{aligned}\mathbf{\Lambda}^1_{jm}[\mathbf{x},\mathbf{\Omega},E] &= \int_E^\infty dH_1\sigma_{jm}(H_1)f_E(E,H_1)\int_0^\pi d\theta\sin\theta f_\Omega(\theta,H_1)\\ &\cdot\int_0^{2\pi}d\beta H[-\mathbf{\Omega}_1\cdot\mathbf{n}(\mathbf{x}'_1)]\frac{P_m(\bar{E}^1_m)\tilde{S}_m(\bar{E}^1_m)}{P_m(H_1)\tilde{S}_m(H_1)}F_m(\bar{E}^1_m),\end{aligned}\tag{227}$$

where $\bar{E}^1_m \approx \bar{E}_m(\rho-\rho',H_1)$. Lastly, since $f_E(E,H_1)$ is sharply peaked, the energy integral can be evaluated in the usual way and yields the approximation

$$\mathbf{\Lambda}^1_{jm}[\mathbf{x},\mathbf{\Omega},E]=\sigma_{jm}(\tilde{E})\frac{P_m(\bar{E}^1_m(\rho-\rho',\tilde{E}))\tilde{S}_m(\bar{E}^1_m(\rho-\rho',\tilde{E}))}{P_m(\tilde{E})\tilde{S}_m(\tilde{E})}F_m(\bar{E}^1_m(\rho-\rho',\tilde{E})),\tag{228}$$

where $\tilde{E}=E+E_s[\hat{E}_m(\rho-\rho',E_0)]$. The first generation fragment flux is then given by the integral

$$\phi^1_j(\mathbf{x},\mathbf{\Omega},E)=\sum_{k\geq j}^N\int_{\rho'}^\rho d\rho''\frac{P_j(E'')\tilde{S}_j(E'')}{P_j(E)\tilde{S}_j(E)}\mathbf{\Lambda}^1_{jk}[\mathbf{x}'',\mathbf{\Omega},E''],\tag{229}$$

where $E''=\bar{E}_j(\rho-\rho'',E)$, and needs to be evaluated by numerical quadrature.

An alternative expression for the first generation fragment flux can be obtained by making use of the fundamental property of the Green's function that allows us to write

$$
\begin{aligned}
\phi_j^1(\mathbf{x},\boldsymbol{\Omega},E) &= [\mathbf{G}^1\cdot\mathbf{F}]_j(\mathbf{x},\boldsymbol{\Omega},E)\\
&= \sum_{k\geq j}^{N}\int_{\partial V}d\mathbf{x}_0\int_{4\pi}d\boldsymbol{\Omega}_0\int_E^{\infty}dE_0 G_{jk}^1(\mathbf{x},\mathbf{x}_0,\boldsymbol{\Omega},\boldsymbol{\Omega}_0,E,E_0)F_k(E_0)\\
&= \sum_{k\geq j}^{N}\int_{\partial V}d\mathbf{x}_0\int_{4\pi}d\boldsymbol{\Omega}_0\int_E^{\infty}dE_0\frac{H[-\boldsymbol{\Omega}\cdot\mathbf{n}(\mathbf{x}')]}{2\pi K_x|\partial_u\mathbf{x}'\times\partial_v\mathbf{x}'|s_x^2}\\
&\quad\cdot\exp\left\{-\frac{(u'-u_0)^2+(v'-v_0)^2}{2s_x^2}\right\}\\
&\quad\cdot\frac{1}{\sqrt{2\pi}K_{\boldsymbol{\Omega}}s_{\boldsymbol{\Omega}}}\exp\left\{-\frac{(1-\boldsymbol{\Omega}\cdot\boldsymbol{\Omega}_0)^2}{2s_{\boldsymbol{\Omega}}^2}\right\}\\
&\quad\cdot\frac{C_{jk}(\rho^*)}{2g'_{jk}(\rho^*)}\left[\operatorname{erf}\left\{\frac{g_{jk}(\rho)}{\sqrt{2}s_k^1(\rho^*)}\right\}-\operatorname{erf}\left\{\frac{g_{jk}(\rho')}{\sqrt{2}s_k^1(\rho^*)}\right\}\right]F_k(E_0)\\
&= \sum_{k\geq j}^{N}\int_E^{\infty}dE_0\frac{C_{jk}(\rho^*)}{2g'_{jk}(\rho^*)}\left[\operatorname{erf}\left\{\frac{g_{jk}(\rho)}{\sqrt{2}s_k^1(\rho^*)}\right\}\right.\\
&\quad\left.-\operatorname{erf}\left\{\frac{g_{jk}(\rho')}{\sqrt{2}s_k^1(\rho^*)}\right\}\right]F_k(E_0). \qquad (230)
\end{aligned}
$$

V.5.1 First Generation Flux in a Half-space with a GCR Boundary Condition

Let V be the half-space, $z\geq 0$, whose boundary ∂V is the xy-plane. In this case, the measured GCR particle flux associated with the 1977 solar minimum [11] will be taken as the incoming flux. Thus, the boundary condition will take the form of equation (183).

Following our previous analysis, the first generation fragment flux $\phi_j^1(\mathbf{x},\boldsymbol{\Omega},E)$ is represented by equation (230).

Figures 79-81 show the oxygen (^{16}O) first generation fragment flux from the iron (^{56}Fe) component of the GCR as a function of γ (Deg) and energy E (MeV/amu), at depths $z=5,10$, and 15 g/cm^2 of aluminum (^{27}Al) respectively. In this case, there is axial symmetry about the z-direction and therefore, the results are presented only for the case in which $\alpha=0$ (Deg). As seen in the figures to follow, the number of fragments are increasing with depth until approximately 80 degrees where a large decrease with depth occurs as the stopping range of the ion is approached. Close to the boundary, the flux of fragments will be low, which is why there is still an

increase in the flux at a relatively shallow depth. These fragments will accumulate with increased depth and will eventually peak as is shown in the first figure. The other two figures show that with increasing depth, the number of fragments decrease as the stopping range is approached.

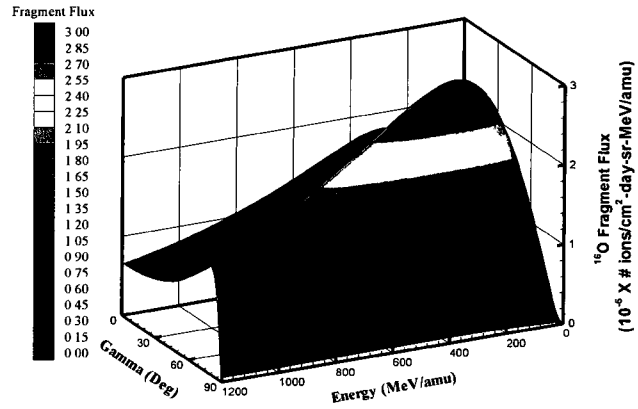

FIGURE 79: The first generation ^{16}O fragment flux at depth $z = 5$ g/cm^2 with $\alpha = 0$ Deg. associated with the ^{56}Fe component of the GCR.

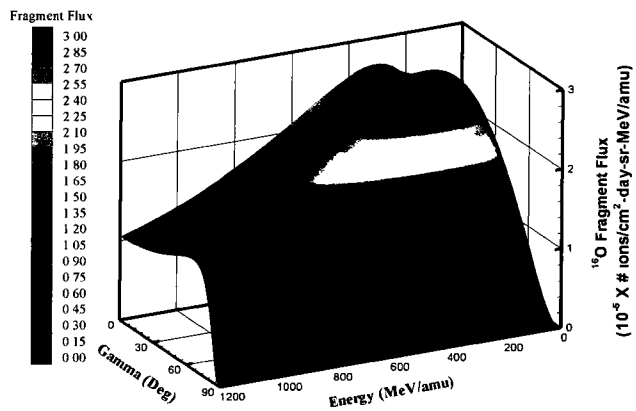

FIGURE 80: The first generation ^{16}O fragment flux at depth $z = 10$ g/cm^2 with $\alpha = 0$ Deg. associated with the ^{56}Fe component of the GCR.

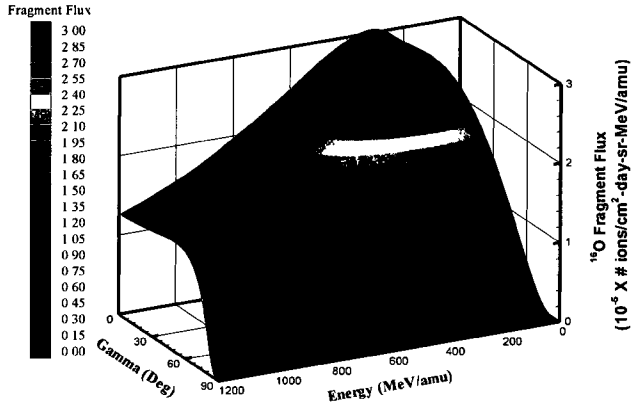

FIGURE 81: The first generation ^{16}O fragment flux at depth $z = 15$ g/cm^2 with $\alpha = 0$ Deg. associated with the ^{56}Fe component of the GCR.

V.5.2 First Generation Flux in a Circular Cylinder with a GCR Boundary Condition

Next, we can consider the target to be a solid aluminum (^{27}Al) cylinder occupying the region $x^2 + y^2 \leq 16^2$, $0 \leq z \leq 36$. The boundary will be irradiated by the measured GCR type m particle flux associated with the 1977 solar minimum [11]. In the figures to follow, figures 82-85, the oxygen (^{16}O) first generation fragment flux from the iron (^{56}Fe) component of the GCR is represented as a function of γ (Deg) and energy E (MeV/amu). Various values of α (Deg) and several target points within the material will be tested.

As γ varies, the distance that the secondary ion has traveled changes depending on the position of the point inside the material.

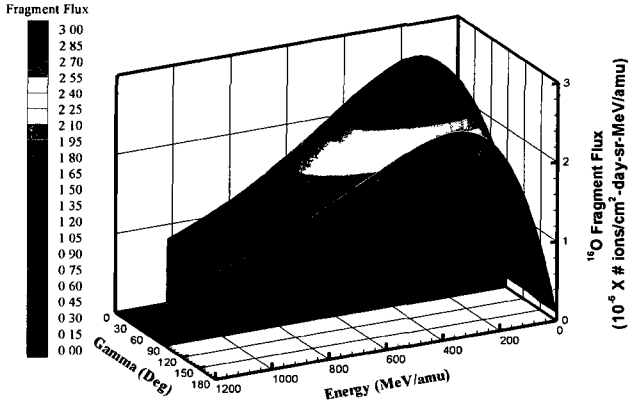

FIGURE 82: The first generation ^{16}O fragment flux at (0,0,0) with $\alpha = 0$ Deg. associated with the ^{56}Fe component of the GCR.

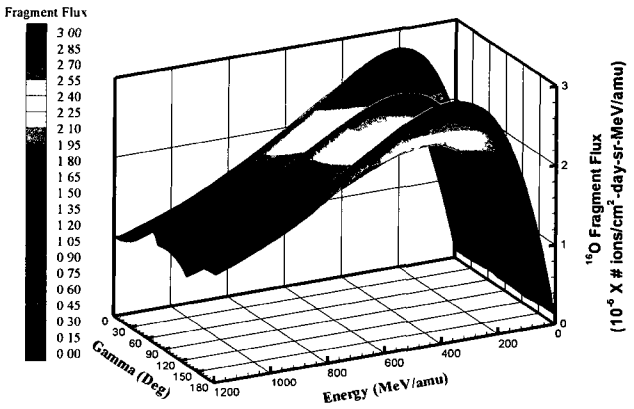

FIGURE 83: The first generation ^{16}O fragment flux at (14,0,9) with $\alpha = 0$ Deg. associated with the ^{56}Fe component of the GCR.

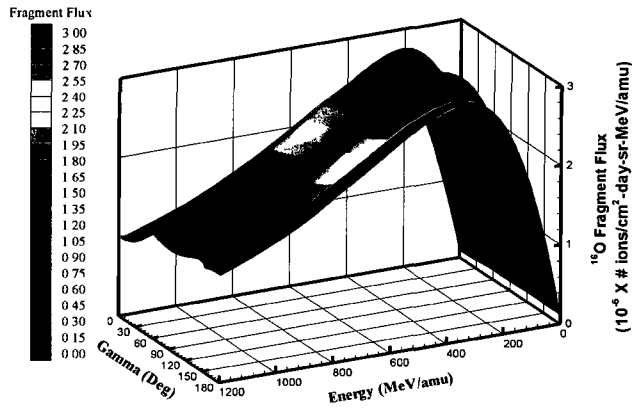

FIGURE 84: The first generation ^{16}O fragment flux at (14,0,9) with $\alpha = 90$ Deg. associated with the ^{56}Fe component of the GCR.

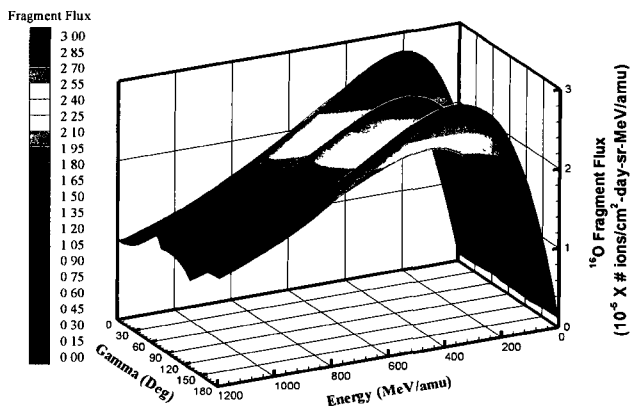

FIGURE 85: The first generation ^{16}O fragment flux at (14,0,9) with $\alpha = 180$ Deg. associated with the ^{56}Fe component of the GCR.

CHAPTER VI

SECOND ORDER GREEN'S FUNCTION

The third term in the Neumann Series is the second order Green's function, which represents the transport of second generation fragments. From the recurrence relation (119), it is seen that the second order Green's function is given by the formula $\mathbf{G}^2 = (\mathbf{Q} \cdot \mathbf{L} \cdot \mathbf{\Xi}) \cdot \mathbf{G}^1$, or in expanded form by

$$\begin{aligned} G^2_{jm}(\mathbf{x}, \mathbf{x_0}, \mathbf{\Omega}, \mathbf{\Omega_0}, E, E_0) &= \int_{\rho'}^{\rho} \frac{P_j(E_2)}{P_j(E)} \frac{\tilde{S}_j(E_2)}{\tilde{S}_j(E)} \\ &\cdot [\mathbf{\Xi} \cdot \mathbf{G}^1]_{jm}(\mathbf{x}_2, \mathbf{x}_0, \mathbf{\Omega}, \mathbf{\Omega}_0, E_2, E_0) d\rho_2, \end{aligned} \tag{231}$$

where $\mathbf{x}_2 = \mathbf{x}' + (\rho_2 - \rho')\mathbf{\Omega}$, $E_2 = \bar{E}_j(\rho - \rho_2, E)$ and

$$\begin{aligned} [\mathbf{\Xi} \cdot \mathbf{G}^1]_{jm}(\mathbf{x}_2, \mathbf{x}_0, \mathbf{\Omega}, \mathbf{\Omega}_0, E_2, E_0) &= \sum_{k=j+1}^{m-1} \int_{E_2}^{\infty} dH_2 \int_{4\pi} d\mathbf{\Omega}_2 \sigma_{jk}(\mathbf{\Omega}, \mathbf{\Omega}_2, E, H_2) \\ &\cdot G^1_{km}(\mathbf{x}, \mathbf{x}_0, \mathbf{\Omega}_2, \mathbf{\Omega}_0, H_2, E_0). \end{aligned} \tag{232}$$

As in the primary flux case, the linear production density is defined by,

$$\begin{aligned} \mathbf{\Lambda}^2_{jkm}(\mathbf{x}_2, \mathbf{x}_0, \mathbf{\Omega}, \mathbf{\Omega}_0, E_2, E_0) &= \int_{E_2}^{\infty} dH_2 \int_{4\pi} d\mathbf{\Omega}_2 \sigma_{jk}(\mathbf{\Omega}, \mathbf{\Omega}_2, E, H_2) \\ &\cdot G^1_{km}(\mathbf{x}, \mathbf{x}_0, \mathbf{\Omega}_2, \mathbf{\Omega}_0, H_2, E_0), \end{aligned} \tag{233}$$

in which case the second order Green's function can be expressed in the form

$$\begin{aligned} G^2_{jm}(\mathbf{x}, \mathbf{x}_0, \mathbf{\Omega}, \mathbf{\Omega}_0, E, E_0) &= \sum_{k=j+1}^{m-1} \int_{\rho'}^{\rho} \frac{P_j(E_2)}{P_j(E)} \frac{\tilde{S}_j(E_2)}{\tilde{S}_j(E)} \\ &\cdot \mathbf{\Lambda}^2_{jkm}(\mathbf{x}_2, \mathbf{x}_0, \mathbf{\Omega}, \mathbf{\Omega}_0, E_2, E_0) d\rho_2. \end{aligned} \tag{234}$$

Since the Green's function is a special case of the broad Green's function, or ion beam spectrum, only the latter need be examined. Therefore, by making use of

equation (198), the linear production density can be expressed as

$$\begin{aligned}\mathbf{\Lambda}^2_{\jmath km}(\mathbf{x}_2,\mathbf{x}_0,\mathbf{\Omega},\mathbf{\Omega}_0,E_2,E_0) \;\approx\; & \int_{E_2}^{\infty} dH_2\sigma_{\jmath k}(H_2)f_E(E_2,H_2)\int_0^{\pi/2}\sin\theta f_\Omega(\theta,H_2)d\theta \\ & \cdot\int_0^{2\pi} d\beta G^1_{km}(\mathbf{x}_2,\mathbf{x}_0,\mathbf{\Omega}_2(\theta,\beta),\mathbf{\Omega}_0,H_2,E_0). \qquad (235)\end{aligned}$$

The angular integrals can be approximated as in the first order Green's function case (204) and yields

$$\begin{aligned}\mathbf{\Lambda}^2_{\jmath km}(\mathbf{x}_2,\mathbf{x}_0,\mathbf{\Omega},\mathbf{\Omega}_0,E_2,E_0) \;\approx\; & \int_{E_2}^{\infty} dH_2\sigma_{\jmath k}(H_2)f_E(E_2,H_2) \\ & \cdot 2\pi G^1_{km}(\mathbf{x}_2,\mathbf{x}_0,\mathbf{\Omega},\mathbf{\Omega}_0,H_2,E_0). \qquad (236)\end{aligned}$$

Now,

$$f_E(E_2,H_2)\approx\frac{1}{\sqrt{2\pi}\epsilon_{\jmath k}}\exp\left(-\frac{(H_2-E_{\jmath k}-E_2)^2}{2\epsilon^2_{\jmath k}}\right), \qquad (237)$$

is very sharply peaked about $\tilde{E}_{\jmath k}=E_{\jmath k}+E_2$, where $E_{\jmath k}=E_{\jmath k}(E_2)=E_s(E_2,A_\jmath,A_k)$ is the collision energy downshift (12) for type j fragments produced from type k projectiles and $\epsilon_{\jmath k}=\epsilon_{\jmath k}(E_2)=\sigma_{\|}(A_\jmath,A_k)\gamma_L(E_2,A_\jmath,A_k)\beta_L(E_2,A_\jmath,A_k)$ is the corresponding width. Therefore, since the other terms in (236) vary slowly with H_2, we can make the additional approximation

$$\mathbf{\Lambda}^2_{\jmath km}(\mathbf{x}_2,\mathbf{x}_0,\mathbf{\Omega},\mathbf{\Omega}_0,E_2,E_0)\approx 2\pi\sigma_{\jmath k}(\tilde{E}_{\jmath k})G^1_{km}(\mathbf{x}_2,\mathbf{x}_0,\mathbf{\Omega},\mathbf{\Omega}_0,\tilde{E}_{\jmath k},E_0). \qquad (238)$$

On substituting into (234), it now follows that the second order Green's function is given by

$$\begin{aligned}G^2_{\jmath m}(\mathbf{x},\mathbf{x}_0,\mathbf{\Omega},\mathbf{\Omega}_0,E,E_0) \;\approx\; & \sum_{k=\jmath+1}^{m-1}\int_{\rho'}^{\rho}\frac{P_\jmath(E_2)}{P_\jmath(E)}\frac{\tilde{S}_\jmath(E_2)}{\tilde{S}_\jmath(E)}\sigma_{\jmath k}(\tilde{E}_{\jmath k}) \\ & \cdot 2\pi G^1_{km}(\mathbf{x}_2,\mathbf{x}_0,\mathbf{\Omega},\mathbf{\Omega}_0,\tilde{E}_{\jmath k},E_0)d\rho_2. \qquad (239)\end{aligned}$$

Let

$$\begin{aligned} g_{km}(\rho'') &= g_{km}(\rho_2, \rho', \tilde{E}_{jk}, E_0; \rho'') \\ &= \hat{E}_m(\rho'' - \rho', E_0) - \bar{E}_k(\rho_2 - \rho'', \tilde{E}_{jk}) - E_{km}(\hat{E}_m(\rho'' - \rho', E_0)), \end{aligned} \quad (240)$$

and let $\rho_1^* = \rho_1^*(\rho_2, \rho', \tilde{E}_{jk}, E_0)$ be the root of the equation $g_{km}(\rho'') = 0$. Then, as shown by equation (218), $G_{km}^1(\mathbf{x}_2, \mathbf{x}_0, \mathbf{\Omega}, \mathbf{\Omega}_0, \tilde{E}_{jk}, E_0)$ is given by

$$\begin{aligned} G_{km}^1(\mathbf{x}_2, \mathbf{x}_0, \mathbf{\Omega}, \mathbf{\Omega}_0, \tilde{E}_{jk}, E_0) \approx & \frac{H[-\mathbf{\Omega} \cdot \mathbf{n}(\mathbf{x}')]}{(2\pi)^{3/2} K_x K_{\mathbf{\Omega}} |\partial_u \mathbf{x}' \times \partial_v \mathbf{x}'| s_x^2 s_{\mathbf{\Omega}}} \\ & \cdot \exp\left\{ -\frac{(1 - \mathbf{\Omega} \cdot \mathbf{\Omega}_0)^2}{2 s_{\mathbf{\Omega}}^2} \right\} \\ & \cdot \exp\left\{ -\frac{(u' - u_0)^2 + (v' - v_0)^2}{2 s_x^2} \right\} \frac{C_{km}(\rho_1^*)}{2 g_{km}'(\rho_1^*)} \\ & \cdot \left\{ \operatorname{erf}\left(\frac{g_{km}(\rho_2)}{\sqrt{2} s_{km}^1(\rho_1^*)} \right) - \operatorname{erf}\left(\frac{g_{km}(\rho')}{\sqrt{2} s_{km}^1(\rho_1^*)} \right) \right\} \end{aligned} \quad (241)$$

where $C_{km}(\rho'') = C_{km}(\rho_2, \rho', \tilde{E}_{jk}, E_0; \rho'') = \dfrac{P_k(E_1)\tilde{S}_k(E_1)}{P_k(\tilde{E}_{jk})\tilde{S}_k(\tilde{E}_{jk})} \dfrac{P_m(E_0)}{P_m(\hat{E}_m)} \sigma_{jm}(\hat{E}_m)$, $s_{km}^1(\rho'')^2 = s_{km}^1(\rho'' - \rho', E_0)^2 = s_m^b(\rho'' - \rho', E_0)^2 + \epsilon_{km}(\hat{E}_m)^2$, $E_1 = \bar{E}_k(\rho_2 - \rho'', \tilde{E}_{jk})$, $\hat{E}_m = \hat{E}_m(\rho'' - \rho', E_0)$, and $g_{km}'(\rho'') = \partial_{\rho''} g_{km}(\rho'')$. It follows that equation (239) can be written in the form

$$\begin{aligned} G_{jm}^2(\mathbf{x}, \mathbf{x}_0, \mathbf{\Omega}, \mathbf{\Omega}_0, E, E_0) \approx & \sum_{k=j+1}^{m-1} \int_{\rho'}^{\rho} \frac{B_{jk}(\rho_2) C_{km}(\rho_1^*)}{2 g_{km}'(\rho_1^*)} \left\{ \operatorname{erf}\left[\frac{g_{km}(\rho_2)}{\sqrt{2} s_{km}^1(\rho_1^*)} \right] \right. \\ & \left. - \operatorname{erf}\left[\frac{g_{km}(\rho')}{\sqrt{2} s_{km}^1(\rho_1^*)} \right] \right\} d\rho_2, \end{aligned} \quad (242)$$

where

$$\begin{aligned} B_{jk}(\rho_2) = & \frac{P_j(E_2)\tilde{S}_j(E_2)}{P_j(E)\tilde{S}_j(E)} \frac{H[-\mathbf{\Omega} \cdot \mathbf{n}(\mathbf{x}')]}{2\pi s_x^2 K_x |\partial_u \mathbf{x}' \times \partial_v \mathbf{x}'|} \\ & \cdot \sigma_{jk}(\tilde{E}_{jk}) \exp\left\{ -\frac{(u' - u_0)^2 + (v' - v_0)^2}{2 s_x^2} \right\} \\ & \cdot \frac{1}{\sqrt{2\pi} s_{\mathbf{\Omega}} K_{\mathbf{\Omega}}} \exp\left\{ -\frac{(1 - \mathbf{\Omega} \cdot \mathbf{\Omega}_0)^2}{2 s_{\mathbf{\Omega}}^2} \right\}. \end{aligned} \quad (243)$$

Now, let $\rho_2 = \rho_2^*$ be a suitable mean value of ρ_2, which is taken to be $\frac{1}{2}(\rho' + \rho)$ in the computations below, and let $E_2^* = E_2^*(\rho - \rho_2^*, E) = \bar{E}_j(\rho - \rho_2^*, E)$ and $\tilde{E}_{jk}^* = \tilde{E}_{jk}(\rho - \rho_2^*, E) = E_{jk}(E^*) + E_2^*$, $\rho^* = \rho_1^*(\rho_2^*, \rho', \tilde{E}_{jk}, E_0)$, and $s_{km}^{1*} = s_{km}^1(\rho^*)$. Then, since ρ_1^*, B_{jk}, C_{km}, g_{km}', and s_{km}^1 are slowly varying functions of ρ_2, we can make the approximation

$$G_{jm}^2(\mathbf{x}, \mathbf{x}_0, \boldsymbol{\Omega}, \boldsymbol{\Omega}_0, E, E_0) = \sum_{k=j+1}^{m-1} \frac{B_{jk}(\rho_2^*) C_{km}(\rho^*)}{2g_{km}'(\rho^*)} \int_{\rho'}^{\rho} \left\{ \operatorname{erf}\left[\frac{g_{km}(\rho_2)}{\sqrt{2}s_{km}^{1*}}\right] - \operatorname{erf}\left[\frac{g_{km}(\rho')}{\sqrt{2}s_{km}^{1*}}\right] \right\} d\rho_2. \tag{244}$$

In order to evaluate the remaining integral in (244), it is convenient to introduce the functions

$$\begin{aligned} w_1(\rho_2) &= w_1(j,k,m,\rho,\rho',E,E_0;\rho_2) = g_{km}(\rho_2,\rho',\tilde{E}_{jk},E_0;\rho_2) \\ &= \hat{E}_m(\rho_2 - \rho', E_0) - \tilde{E}_{jk}(E_2) - E_{km}(\hat{E}_m(\rho_2 - \rho', E_0)), \end{aligned} \tag{245}$$

and

$$\begin{aligned} w_2(\rho_2) &= w_2(j,k,m,\rho,\rho',E,E_0;\rho_2) = g_{km}(\rho_2,\rho',\tilde{E}_{jk},E_0;\rho') \\ &= E_0 - \bar{E}_k(\rho_2 - \rho', \tilde{E}_{jk}(E_2)) - E_{km}(E_0), \end{aligned} \tag{246}$$

in which case it is found that

$$G_{jm}^2(\mathbf{x}, \mathbf{x}_0, \boldsymbol{\Omega}, \boldsymbol{\Omega}_0, E, E_0) = \sum_{k=j+1}^{m-1} \frac{B_{jk}(\rho_2^*) C_{km}(\rho^*)}{2g_{km}'(\rho^*)} \left[W_{km}^{(1)}(\rho,\rho') - W_{km}^{(2)}(\rho,\rho') \right], \tag{247}$$

where

$$W_{km}^{(p)}(\rho,\rho') = \int_{\rho'}^{\rho} \operatorname{erf}\left[\frac{w_p(\rho_2)}{\sqrt{2}s_{km}^{1*}}\right] d\rho_2, \tag{248}$$

and $p = 1, 2$.

VI.0.3 Approximations for $W_{km}^{(1)}(\rho,\rho')$ and $W_{km}^{(2)}(\rho,\rho')$

First observe that $w_p(\rho_2)$ $(p=1,2)$ is a monotone function of ρ_2, and let $\rho_2=\rho_{w_p}$ be the solution of the equation $w_p(\rho_2)=0$. Then, from equations (245) and (246), it can be shown that

$$\rho_{w_1}\approx\rho'+\frac{\nu_j}{\nu_m-\nu_j}(R_j(E_0)-R_j(E)+\rho'-\rho), \tag{249}$$

and

$$\rho_{w_2}\approx\rho'+\frac{\nu_j}{\nu_k-\nu_j}(R_j(E_0)-R_j(E)+\rho'-\rho). \tag{250}$$

Now define,

$$\hat{\rho}_p=\begin{cases}\rho_{w_p} & \text{if } \rho'\le\rho_{w_p}\le\rho\\ \rho' & \text{otherwise}\end{cases} \tag{251}$$

and introduce the linear approximation

$$w_p(\rho_2)\approx w_p(\hat{\rho}_2)+w_p'(\hat{\rho}_2)(\rho_2-\hat{\rho}_2), \tag{252}$$

for which $w_p'(\rho_2)\approx w_p'(\hat{\rho}_2)$. Then, by making the change of variables $t_2=\dfrac{w_p(\rho_2)}{\sqrt{2}s_{km}^{1*}}$, $dt_2=\dfrac{w_p'(\hat{\rho}_2)}{\sqrt{2}s_{km}^{1*}}d\rho_2$, in equation (248) it is found that

$$\begin{aligned}
W_{km}^{(p)}(\rho,\rho') &= \int_{\rho'}^{\rho}\operatorname{erf}\left[\frac{w_p(\rho_2)}{\sqrt{2}s_{km}^{1*}}\right]d\rho_2\\
&\approx \frac{\sqrt{2}s_{km}^{1*}}{w_p'(\hat{\rho}_2)}\int_{t'}^{t}\operatorname{erf}[t_2]\,dt_2\\
&= \frac{\sqrt{2}s_{km}^{1*}}{w_p'(\hat{\rho}_2)}\left[t_2\operatorname{erf}(t_2)+\frac{1}{\sqrt{\pi}}\exp\left\{-(t_2)^2\right\}\right]\Bigg|_{t'}^{t}\\
&= \frac{\sqrt{2}s_{km}^{1*}}{w_p'(\hat{\rho}_2)}\left[\frac{w_p(\rho)}{\sqrt{2}s_{km}^{1*}}\operatorname{erf}\left(\frac{w_p(\rho)}{\sqrt{2}s_{km}^{1*}}\right)\right.\\
&\quad -\frac{w_p(\rho')}{\sqrt{2}s_{km}^{1*}}\operatorname{erf}\left(\frac{w_p(\rho')}{\sqrt{2}s_{km}^{1*}}\right)\\
&\quad \left.+\frac{1}{\sqrt{\pi}}\exp\left(-\frac{w_p(\rho)^2}{2(s_{km}^{1*})^2}\right)-\frac{1}{\sqrt{\pi}}\exp\left(-\frac{w_p(\rho')^2}{2(s_{km}^{1*})^2}\right)\right].
\end{aligned} \tag{253}$$

As a verification of the approximations used, the second order broad Green's

function was computed by evaluating the integrals in equation (247) numerically by using a simple trapezoidal rule. A comparison was then made between the analytical approximation and those obtained by the quadrature results. This comparison is shown in figures 86 and 87, which exhibit the oxygen (^{16}O) fragment flux at depth $z =$ 10 g/cm^2 when the projectile is taken to be iron (^{56}Fe) with an initial energy of 1000 (MeV/amu), a width of 10 (MeV/amu), and the target was aluminum (^{27}Al). Note that there is good agreement between the results, indicating that the approximations used are accurate.

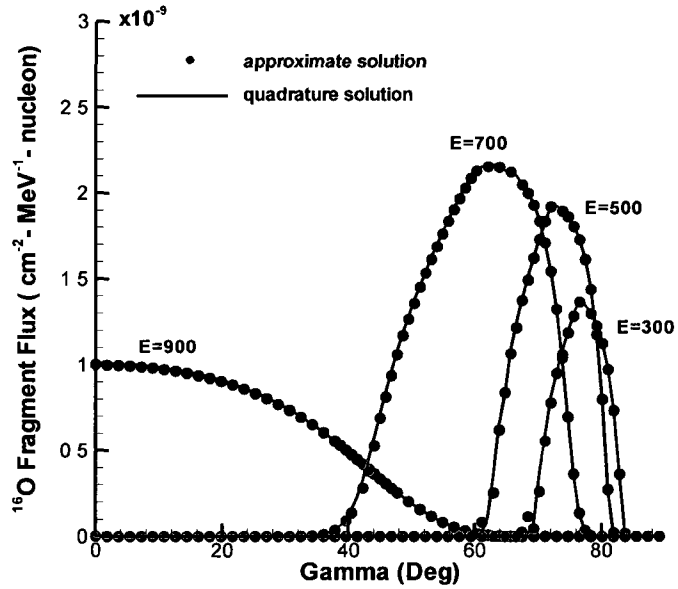

FIGURE 86: A comparison between the approximate and quadrature solution for the second generation ^{16}O fragment flux at depth $z = 10$ g/cm^2 for several energies (MeV/amu).

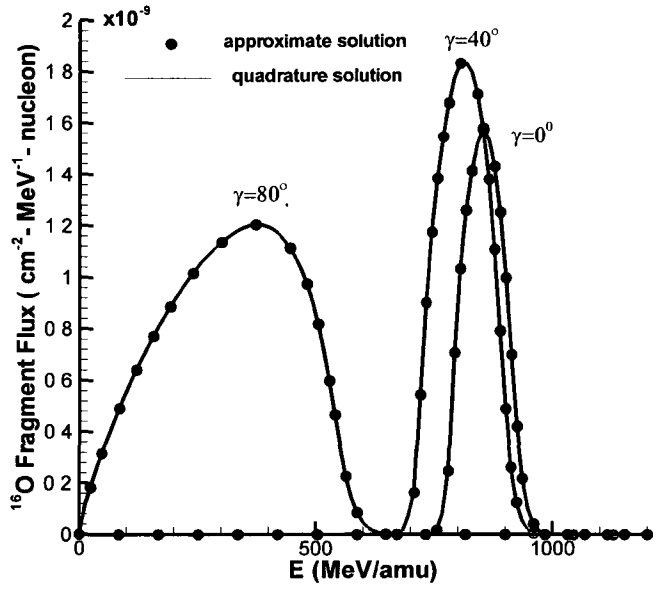

FIGURE 87: A comparison between the approximate and quadrature solution for the second generation ^{16}O fragment flux at depth $z = 10$ g/cm^2 for several inclination angles (Deg).

The next two figures show the profile of the secondary oxygen (^{16}O) fragment flux as a function of initial projectile energy and fragment energy at a depth of $z = 10$ g/cm^2 of aluminum (^{27}Al) with a iron (^{56}Fe) projectile for both the approximate and the quadrature solution. The global similarities between the solutions can be seen in these figures.

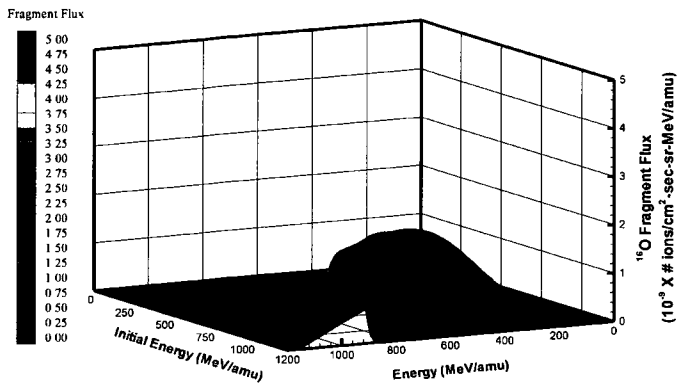

FIGURE 88: Approximate solution for the second generation ^{16}O fragment flux with varying projectile and fragment energies.

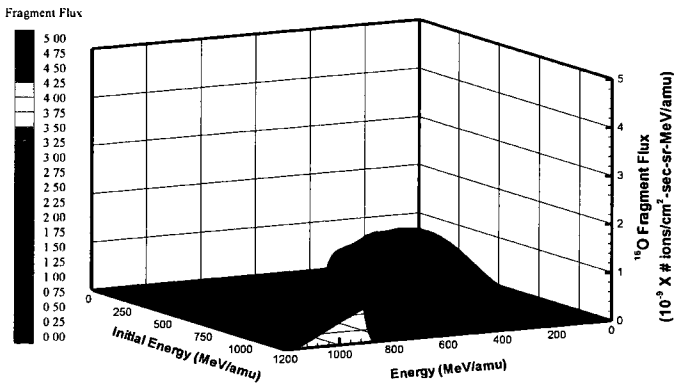

FIGURE 89: Quadrature solution for the second generation ^{16}O fragment flux with varying projectile and fragment energies.

VI.0.4 Second Generation Flux in a Half-space with an Ion Beam Boundary Condition

For illustrative purposes, an aluminum (^{27}Al) half-space is considered as the target material of interest. For this case, the second generation fragment flux is given by

$$G^2_{jm}(\mathbf{x},\mathbf{x}_0,\mathbf{\Omega},\mathbf{\Omega}_0,E,E_0) \approx \sum_{k=j+1}^{m-1} \frac{P_j(E_2^*)\tilde{S}_j(E_2^*)}{P_j(E)\tilde{S}_j(E)} \frac{H[-\mathbf{\Omega}\cdot\mathbf{n}(\mathbf{x}')]}{2\pi s_x^2 K_x}$$
$$\cdot\sigma_{jk}(\tilde{E}_{jk}^*)\exp\left\{-\frac{(x'-x_0)^2+(y'-y_0)^2}{2s_x^2}\right\}$$
$$\cdot\frac{1}{\sqrt{2\pi}s_{\mathbf{\Omega}}K_{\mathbf{\Omega}}}\exp\left\{-\frac{(1-\mathbf{\Omega}\cdot\mathbf{\Omega}_0)^2}{2s_{\mathbf{\Omega}}^2}\right\}\frac{C_{km}(\rho^*)}{2g'_{km}(\rho^*)}$$
$$\cdot\left[W^{(1)}_{km}(\rho,\rho')-W^{(2)}_{km}(\rho,\rho')\right], \qquad (254)$$

where the boundary, ∂V, is given by equation (160) and the surface differential, dS, is given by equation (161).

In the following figure, the second generation oxygen (^{16}O) fragment flux as a function of inclination angle, γ (Deg), and energy (MeV/amu) at depths $z = 5, 10, 15$ and 30 g/cm^2 of aluminum (^{27}Al) with an 1000 MeV/amu iron (^{56}Fe) projectile are illustrated. Furthermore, $s_E = 30$ (MeV/amu), $s_{\mathbf{\Omega}} = 45$ (Deg), $s_x = 1$, and $\mathbf{\Omega}_0 = (\frac{1}{\sqrt{2}}, 0, \frac{1}{\sqrt{2}})$. From this figure, it is seen that the fragment flux peaks around 15 g/cm^2. After which, the flux becomes more spread out with energy, but becomes sharply peaked around the mean initial direction of the projectile.

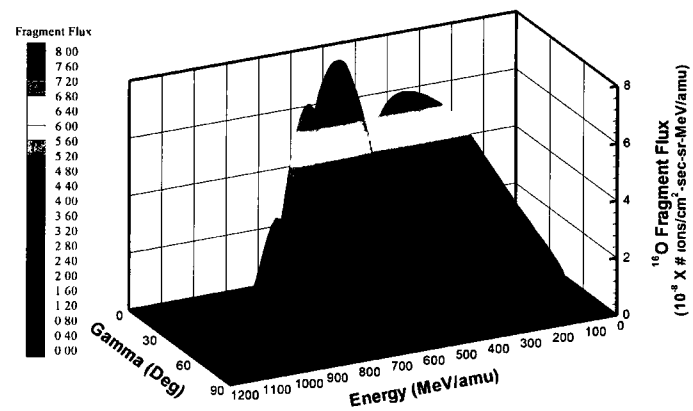

FIGURE 90: The second generation ^{16}O fragment flux at depths $z = 5, 10, 15$, and 30 g/cm^2 with $\alpha = 0$ Deg.

For consideration of other target geometries, such as a sphere or cylinder, the

surface Jacobian, $|\partial_u \mathbf{x}' \times \partial_v \mathbf{x}'|$, needs to be calculated and the singular points need to be considered as was done for the zero order Green's function.

VI.1 A UNIFORM ISOTROPIC BOUNDARY CONDITION

For the special case in which the boundary flux is uniform, isotropic, and has a Gaussian energy profile, the primary and first generation flux are given by equation (150) and (226) respectively. The second generation fragment flux can be obtained by integrating equation (254) over all the boundary points, $\mathbf{x}_0$, and all directions, $\mathbf{\Omega}_0$. This yields the result

$$\begin{aligned}
\phi_j^2(\mathbf{x},\mathbf{\Omega},E) \approx & \sum_{k=j+1}^{m-1} \frac{P_j(E_2^*)\tilde{S}_j(E_2^*)}{P_j(E)\tilde{S}_j(E)} \sigma_{jk}(\tilde{E}_{jk}^*) \frac{C_{km}(\rho^*)}{2g'_{km}(\rho^*)} \\
& \cdot \left\{ \frac{\sqrt{2}s_{km}^{1*}}{w_1'(\hat{\rho}_2)} \left[\frac{w_1(\rho)}{\sqrt{2}s_{km}^{1*}} \operatorname{erf}\left(\frac{w_1(\rho)}{\sqrt{2}s_{km}^{1*}} \right) \right. \right. \\
& - \frac{w_1(\rho')}{\sqrt{2}s_{km}^{1*}} \operatorname{erf}\left(\frac{w_1(\rho')}{\sqrt{2}s_{km}^{1*}} \right) + \frac{1}{\sqrt{\pi}} \exp\left(-\frac{w_1(\rho)^2}{2(s_{km}^{1*})^2} \right) \\
& \left. - \frac{1}{\sqrt{\pi}} \exp\left(-\frac{w_1(\rho')^2}{2(s_{km}^{1*})^2} \right) \right] \\
& - \frac{\sqrt{2}s_{km}^{1*}}{w_2'(\hat{\rho}_2)} \left[\frac{w_2(\rho)}{\sqrt{2}s_{km}^{1*}} \operatorname{erf}\left(\frac{w_2(\rho)}{\sqrt{2}s_{km}^{1*}} \right) - \frac{w_2(\rho')}{\sqrt{2}s_{km}^{1*}} \operatorname{erf}\left(\frac{w_2(\rho')}{\sqrt{2}s_{km}^{1*}} \right) \right. \\
& \left. \left. + \frac{1}{\sqrt{\pi}} \exp\left(-\frac{w_2(\rho)^2}{2(s_{km}^{1*})^2} \right) - \frac{1}{\sqrt{\pi}} \exp\left(-\frac{w_2(\rho')^2}{2(s_{km}^{1*})^2} \right) \right] \right\}. \qquad (255)
\end{aligned}$$

VI.1.1 Second Generation Flux in a Half-space with a Uniform Isotropic Boundary Condition

For illustrative purposes, an aluminum half-space is considered as the target material of interest. Figures 91-93 show the secondary oxygen (^{16}O) fragment flux as a function of inclination angle, γ, and energy at depths $z = 5, 10, 15$, and 30 g/cm^2 of aluminum (^{27}Al) with an 1000 MeV/amu iron (^{56}Fe) projectile. In these figures, at the smaller depths, the number of fragments are increasing with depth up to approximately 80 degrees where a large decrease with depth occurs as the stopping range of the particle is approached. Close to the boundary, there are no fragments produced, which is why there is still an increase in fragments at a relatively shallow depths.

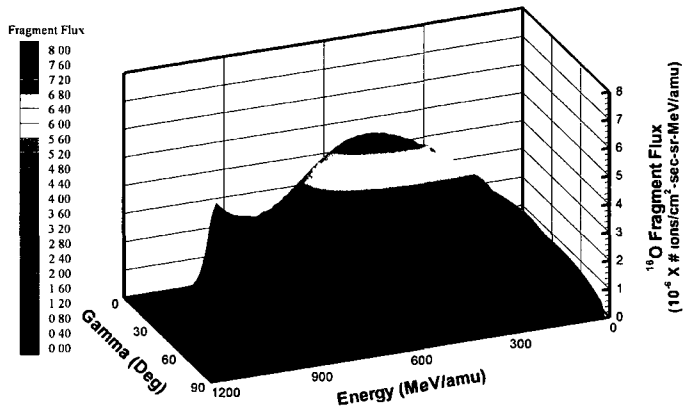

FIGURE 91: The second generation ^{16}O fragment flux at depth $z = 5$ g/cm^2 with $\alpha = 0$ Deg.

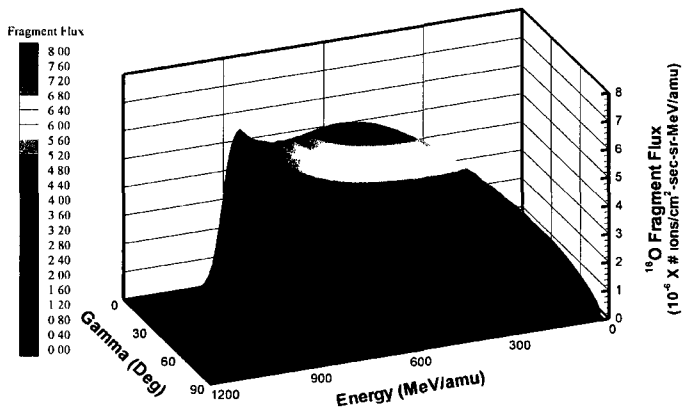

FIGURE 92: The second generation ^{16}O fragment flux at depth $z = 10$ g/cm^2 with $\alpha = 0$ Deg.

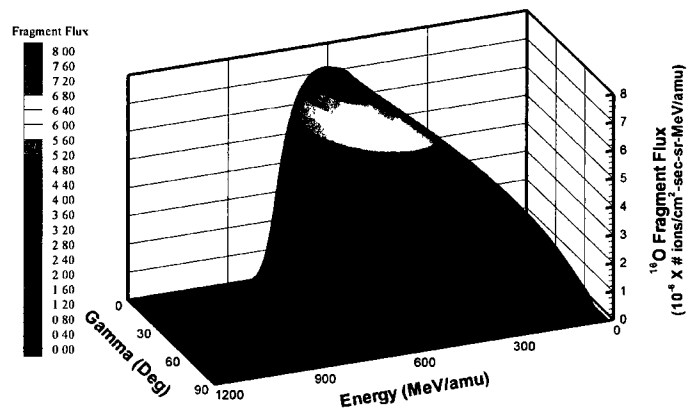

FIGURE 93: The second generation ^{16}O fragment flux at depth $z = 30$ g/cm^2 with $\alpha = 0$ Deg.

Next, the second generation fragment flux will be calculated with a GCR boundary condition.

VI.2 GCR BOUNDARY CONDITION

Since the GCR is uniform, isotropic, and is a broad function of energy, the corresponding second generation fragment flux can be obtained from the Green's function

formalism in the usual way (107). It is therefore given by

$$\begin{aligned}
\phi_\jmath^2(\mathbf{x},\mathbf{\Omega},E) &= [\mathbf{G}^2\cdot\mathbf{F}]_\jmath(\mathbf{x},\mathbf{\Omega},E) \\
&= \sum_{m\geq\jmath}^{N}\int_{\partial V}d\mathbf{x}_0\int_{4\pi}d\mathbf{\Omega}_0\int_E^\infty dE_0 G_{\jmath m}^2(\mathbf{x},\mathbf{x}_0,\mathbf{\Omega},\mathbf{\Omega}_0,E,E_0)F_m(E_0) \\
&\approx \sum_{m\geq\jmath}^{N}\sum_{k=\jmath+1}^{m-1}\int_{\partial V}d\mathbf{x}_0\int_{4\pi}d\mathbf{\Omega}_0\int_E^\infty dE_0\frac{P_\jmath(E_2^*)\tilde{S}_\jmath(E_2^*)}{P_\jmath(E)\tilde{S}_\jmath(E)}\frac{\sigma_{\jmath k}(\tilde{E}_{\jmath k}^*)}{\sqrt{2\pi}K_{\mathbf{\Omega}}s_{\mathbf{\Omega}}} \\
&\quad\cdot\exp\left(-\frac{(1-\mathbf{\Omega}\cdot\mathbf{\Omega}_0)^2}{2s_{\mathbf{\Omega}}^2}\right)\exp\left(-\frac{(u'-u_0)^2+(v'-v_0)^2}{2s_x^2}\right) \\
&\quad\cdot\frac{C_{km}(\rho^*)}{2g'_{km}(\rho^*)}\left[W_{km}^{(1)}(\rho,\rho')-W_{km}^{(2)}(\rho,\rho')\right]F_m(E_0) \\
&\approx \sum_{m\geq\jmath}^{N}\sum_{k=\jmath+1}^{m-1}\int_E^\infty dE_0\frac{P_\jmath(E_2^*)\tilde{S}_\jmath(E_2^*)}{P_\jmath(E)\tilde{S}_\jmath(E)}\frac{\sigma_{\jmath k}(\tilde{E}_{\jmath k}^*)C_{km}(\rho^*)}{2g'_{km}(\rho^*)} \\
&\quad\cdot\left[W_{km}^{(1)}(\rho,\rho')-W_{km}^{(2)}(\rho,\rho')\right]F_m(E_0). \qquad (256)
\end{aligned}$$

VI.2.1 Second Generation Flux in a Half-space with a GCR Boundary Condition

Let V be the half-space $z \geq 0$, whose boundary ∂V is the xy-plane. In this case, the measured GCR particle flux associated with the 1977 solar minimum [11] will be taken as an incoming flux. Thus, the boundary condition will take the form of equation (183).

Following our previous analysis, the second generation fragment flux $\phi_\jmath^2(\mathbf{x},\mathbf{\Omega},E)$ is represented by equation (256).

Figures 94-96 show the oxygen (^{16}O) second generation fragment flux associated with the (^{56}Fe) component of the GCR as a function of γ (Deg) and energy E (MeV/amu), at depths $z = 5, 10$, and 20 g/cm^2 of aluminum (^{27}Al) respectively. In this case, there is axial symmetry about the z-direction and therefore, the results are presented only for the case in which $\alpha = 0$ (Deg). As seen in the following figures, the number of fragments are increasing with depth until approximately 80 degrees where a large decrease with depth occurs as the stopping range of the ion is approached. Close to the boundary, there are no second generation fragments produced, which is why there is still an increase in fragments at a relatively shallow depth.

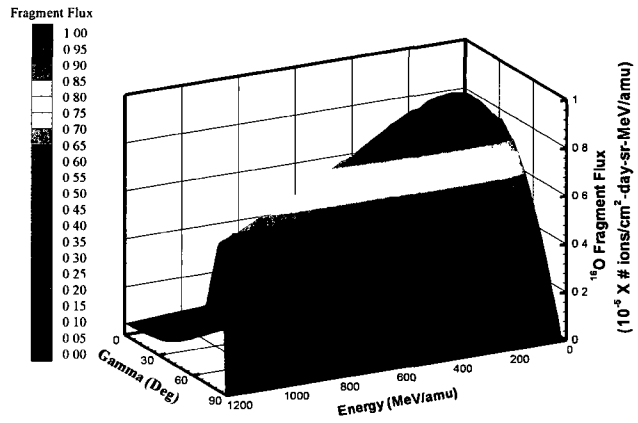

FIGURE 94: The ^{16}O second generation fragment flux at depth $z = 5$ g/cm^2 with $\alpha = 0$ Deg. associated with the ^{56}Fe component of the GCR.

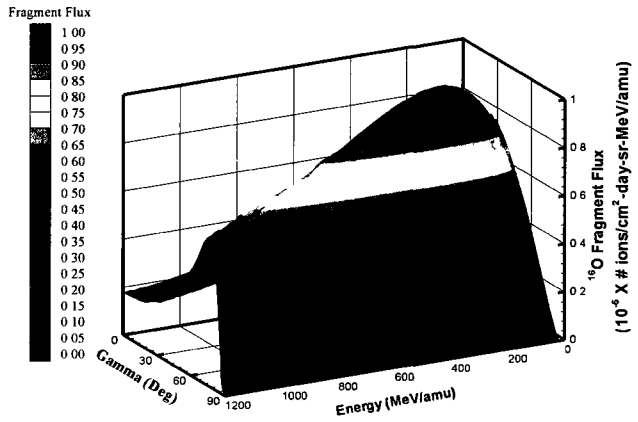

FIGURE 95: The ^{16}O second generation fragment flux at depth $z = 10$ g/cm^2 with $\alpha = 0$ Deg. associated with the ^{56}Fe component of the GCR.

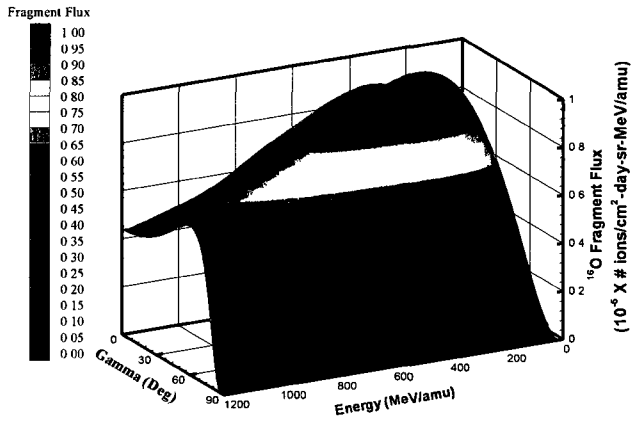

FIGURE 96: The ^{16}O second generation fragment flux at depth $z = 20$ g/cm^2 with $\alpha = 0$ Deg. associated with the ^{56}Fe component of the GCR.

CHAPTER VII

THE NONPERTURBATIVE NEUMANN SERIES REMAINDER

For $n > 2$, the recurrence formula, $\mathbf{G}^n = (\mathbf{Q} \cdot \mathbf{L} \cdot \Xi) \cdot \mathbf{G}^{n-1}$, continues to become more complicated with each subsequent term. The numerical integration that would be involved in each term is computationally expensive and therefore a non-perturbative technique is used to estimate the remaining terms in the Neumann series.

To formulate this approximation, the Boltzmann equation with a unit boundary condition is reintroduced,

$$\begin{aligned} &[\mathbf{\Omega} \cdot \nabla - \frac{\partial}{\partial E}\tilde{S}_j(E) + \sigma_j(E)]G_{jm}[\mathbf{x}, \mathbf{x}_0, \mathbf{\Omega}, \mathbf{\Omega}_0, E, E_0] \\ = &\sum_{m>j}^{N} \int_E^\infty \int_{4\pi} \sigma_{jk}(\mathbf{\Omega}, \mathbf{\Omega}', E, E')G_{km}[\mathbf{x}, \mathbf{x}_0, \mathbf{\Omega}', \mathbf{\Omega}_0, E', E_0]d\mathbf{\Omega}'dE', \end{aligned} \tag{257}$$

with the boundary condition

$$G_{jm}[\mathbf{x}_b, \mathbf{x}_0, \mathbf{\Omega}, \mathbf{\Omega}_0, E, E_0] = \delta_{jm}\delta(\mathbf{\Omega} - \mathbf{\Omega}_0)\delta(E - E_0)\overline{\delta}(\mathbf{x}_b - \mathbf{x}_0). \tag{258}$$

At sufficiently high energies, the nuclear cross sections are sharply peaked in both angle and energy. To take advantage of this fact, the integral flux will be denoted by

$$\bar{g}_{jm}(\rho - \rho') = \int_{\Re}\int_{4\pi} G_{jm}(\mathbf{x}, \mathbf{x}', \mathbf{\Omega}, \mathbf{\Omega}', E, E')d\mathbf{\Omega}'dE, \tag{259}$$

where $\rho' < \rho < \rho + R_m(E')$.

Using these assumptions, the three dimensional Boltzmann equation reduces to the one dimensional linear Boltzmann equation with the straight-ahead approximation. Thus, the initial value problem is given by

$$\partial_\rho \phi_j(\rho, E) = \sum_{m>j}^{N} \int \sigma_{jk}(E, E')\phi_k(\rho, E')dE' - \sigma_j(E)\phi_j(\rho, E), \tag{260}$$

with the boundary condition of

$$\phi_j(\rho', E) = \delta_{jm}\delta(E - E'). \tag{261}$$

With the integral flux described in equation (259) applied to equation (260), the Boltzmann equation becomes

$$[\frac{d}{d\rho} + \sigma_j]\bar{g}_{jm}(\rho - \rho') = \sum_{m>j}^{N} \sigma_{jk}\bar{g}_{km}(\rho - \rho'), \tag{262}$$

where $\rho' < \rho < \rho + R_m(E')$, and $\bar{g}_{km}(0) = \delta_{jm}$.

This has been investigated by Wilson et. al. [13] and it has been shown to have the solution of

$$\begin{aligned} \bar{g}_{jm}(\rho - \rho') &= \sum_{n=0}^{\infty} \bar{g}^n_{jm}(\rho - \rho') \\ &= \delta_{jm}g(m) + \sigma_{jm}g(j,m) + \sum_k \sigma_{jk}\sigma_{km}g(j,k,m) + \ldots, \end{aligned} \tag{263}$$

where the g-functions are given by

$$g(j) = \exp\{-\sigma_j(\rho - \rho')\}, \tag{264}$$

and

$$g(j_1, j_2, j_3, \ldots, j_n, j_{n+1}) = \frac{g(j_1, j_2, j_3, \ldots, j_{n-1}, j_n) - g(j_1, j_2, j_3, \ldots, j_{n-1}, j_{n+1})}{\sigma_{j_{n+1}} - \sigma_{j_n}}. \tag{265}$$

It has since been shown in [14, 31] that

$$\bar{g}_{jm}(\rho - \rho') = \sum \bar{g}_{jk}(\rho - \rho'')\bar{g}_{km}(\rho'' - \rho'), \tag{266}$$

where $\rho' < \rho'' < \rho$.

At small depths, $\bar{g}_{jm}(\rho - \rho')$ is accurately evaluated by the first few terms in equation (263). It can then be evaluated at arbitrary depths by making use of the above convolution formula.

For $n \geq 2$, there is little variation in the spectral shapes and therefore the following assumption can be made,

$$\frac{G^n_{jm}(\mathbf{x}, \mathbf{x}', \mathbf{\Omega}, \mathbf{\Omega}', E, E')}{\bar{g}^n_{jm}(\rho - \rho')} \approx \frac{G^2_{jm}(\mathbf{x}, \mathbf{x}', \mathbf{\Omega}, \mathbf{\Omega}', E, E')}{\bar{g}^2_{jm}(\rho - \rho')}. \tag{267}$$

It then follows that the Neumann series remainder can be approximated by

$$
\begin{aligned}
G^{NP}_{jm}(\mathbf{x},\mathbf{x}',\mathbf{\Omega},\mathbf{\Omega}',E,E') &= \sum_{n=3}^{\infty} G^{n}_{jm}(\mathbf{x},\mathbf{x}',\mathbf{\Omega},\mathbf{\Omega}',E,E') \\
&= \sum_{n=3}^{\infty} \frac{G^{n}_{jm}(\mathbf{x},\mathbf{x}',\mathbf{\Omega},\mathbf{\Omega}',E,E')}{\bar{g}^{n}_{jm}(\rho-\rho')} \cdot \bar{g}^{n}_{jm}(\rho-\rho') \\
&\approx \frac{G^{2}_{jm}(\mathbf{x},\mathbf{x}',\mathbf{\Omega},\mathbf{\Omega}',E,E')}{\bar{g}^{2}_{jm}(\rho-\rho')} \sum_{n=3}^{\infty} \bar{g}^{n}_{jm}(\rho-\rho') \\
&\approx \frac{G^{2}_{jm}(\mathbf{x},\mathbf{x}',\mathbf{\Omega},\mathbf{\Omega}',E,E')}{\bar{g}^{2}_{jm}(\rho-\rho')} [\bar{g}_{jm}(\rho-\rho') \\
&- \bar{g}^{0}_{jm}(\rho-\rho') - \bar{g}^{1}_{jm}(\rho-\rho') - \bar{g}^{2}_{jm}(\rho-\rho')]. \quad (268)
\end{aligned}
$$

VII.1 ION BEAM SPECTRUM

To calculate the contribution of the Neumann series remainder, the second order Green's function given by equation (247) will be used in equation (268).

For illustrative purposes, an aluminum (^{27}Al) half-space is considered as the target material of interest. In the following figure shown below, figure 97, the nonperturbative remainder for an oxygen (^{16}O) fragment as a function of inclination angle, γ (Deg), and energy (MeV/amu) at depths $z = 5, 10$, and 30 g/cm^2 of aluminum (^{27}Al) with an 1000 MeV/amu iron (^{56}Fe) projectile are illustrated. Further, $s_E = 30$ (MeV/amu), $s_{\Omega} = 45$ (Deg), $s_x = 1$, and $\mathbf{\Omega}_0 = (\frac{1}{\sqrt{2}}, 0, \frac{1}{\sqrt{2}})$. From this figure, it is seen that the magnitude of the nonperturbative remainder increases with depth. Further, the flux becomes more spread out with energy, but becomes sharply peaked around the mean initial direction of the projectile.

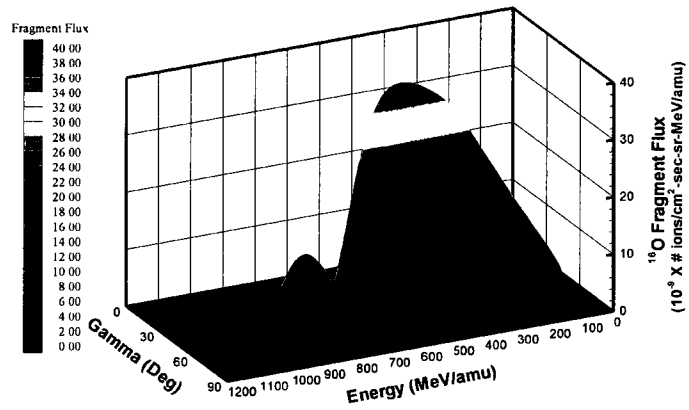

FIGURE 97: The nonperturbative remainder at depths (from left to right) $z = 5, 10,$ and 30 g/cm^2 with $\alpha = 0$ Deg.

The increase of flux with depth is expected since the contribution is coming from the higher order fragment ions.

For consideration of other target geometries, such as a sphere or cylinder, the surface Jacobian, $|\partial_u \mathbf{x}' \times \partial_v \mathbf{x}'|$, needs to be calculated and the singular points need to be considered as was done for the zero order Green's function.

VII.2 UNIFORM ISOTROPIC BOUNDARY CONDITIONS

For the special case in which the boundary flux is uniform, isotropic, and has a Gaussian energy profile, the remainder is obtained by making use of the previously derived representation for the second order Green's function given by equation (247). In this situation, the flux given by the remainder of the series is represented as

$$\phi^{NP}(\mathbf{x},\mathbf{\Omega},E) = \sum_{k=j+1}^{m-1} \frac{P_j(E_2^*)\tilde{S}_j(E_2^*)}{P_j(E)\tilde{S}_j(E)}\sigma_{jk}(\tilde{E}_{jk}^*)\frac{C_{km}(\rho^*)}{2g'_{km}(\rho^*)}$$
$$\cdot\left\{\frac{\sqrt{2}s_{km}^{1*}}{w_1'(\hat{\rho}_2)}\left[\frac{w_1(\rho)}{\sqrt{2}s_{km}^{1*}}\,\mathrm{erf}\left(\frac{w_1(\rho)}{\sqrt{2}s_{km}^{1*}}\right)\right.\right.$$
$$-\frac{w_1(\rho')}{\sqrt{2}s_{km}^{1*}}\,\mathrm{erf}\left(\frac{w_1(\rho')}{\sqrt{2}s_{km}^{1*}}\right)+\frac{1}{\sqrt{\pi}}\exp\left(-\frac{w_1(\rho)^2}{2(s_{km}^{1*})^2}\right)$$
$$\left.-\frac{1}{\sqrt{\pi}}\exp\left(-\frac{w_1(\rho')^2}{2(s_{km}^{1*})^2}\right)\right]$$
$$-\frac{\sqrt{2}s_{km}^{1*}}{w_2'(\hat{\rho}_2)}\left[\frac{w_2(\rho)}{\sqrt{2}s_{km}^{1*}}\,\mathrm{erf}\left(\frac{w_2(\rho)}{\sqrt{2}s_{km}^{1*}}\right)-\frac{w_2(\rho')}{\sqrt{2}s_{km}^{1*}}\,\mathrm{erf}\left(\frac{w_2(\rho')}{\sqrt{2}s_{km}^{1*}}\right)\right.$$
$$\left.\left.+\frac{1}{\sqrt{\pi}}\exp\left(-\frac{w_2(\rho)^2}{2(s_{km}^{1*})^2}\right)-\frac{1}{\sqrt{\pi}}\exp\left(-\frac{w_2(\rho')^2}{2(s_{km}^{1*})^2}\right)\right]\right\}[\bar{g}_{jm}(x-x')$$
$$-\bar{g}_{jm}^0(x-x')-\bar{g}_{jm}^1(x-x')-\bar{g}_{jm}^2(x-x')]/\bar{g}_{jm}^2(x-x'). \qquad (269)$$

VII.2.1 Remainder Flux in a Half-space with a Uniform Isotropic Boundary Condition

For illustrative purposes, an aluminum half-space is considered as the target material of interest. Figures 98-100 demonstrate the nonperturbative remainder for an oxygen (^{16}O) fragment as a function of inclination angle, γ (Deg), and energy (MeV/amu) at depths $z = 5, 10$, and 30 g/cm^2 of aluminum (^{27}Al) with an 1000 MeV/amu iron (^{56}Fe) projectile. In these figures, at the smaller depths, the contribution for the remainder is small and grows rapidly at approximately 60 degrees when the depth into the material has reached the point where the ions are starting to be produced. Close to the boundary, there are no remainder fragments produced, which is why there is an increase in fragments at a relatively shallow depths.

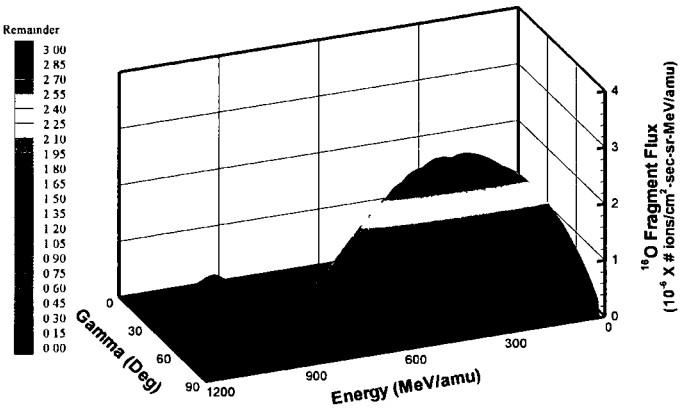

FIGURE 98: The nonperturbative remainder at depth $z = 5$ g/cm^2 with $\alpha = 0$ Deg.

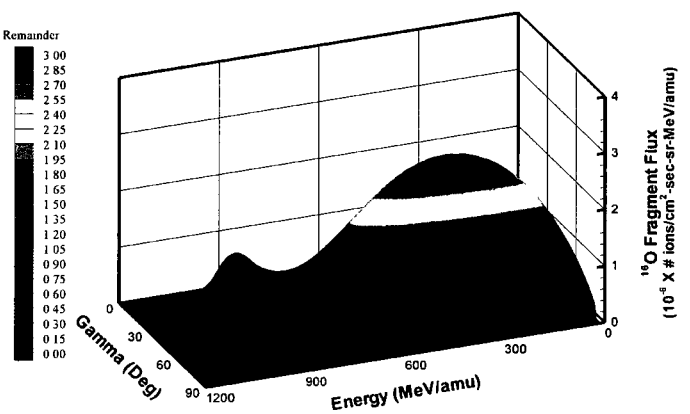

FIGURE 99: The nonperturbative remainder at depth $z = 10$ g/cm^2 with $\alpha = 0$ Deg.

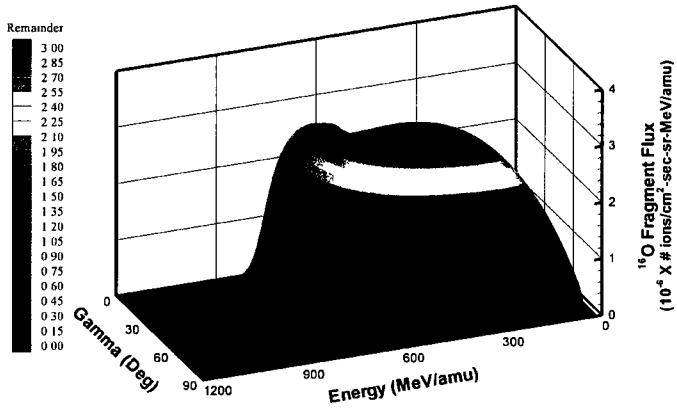

FIGURE 100: The nonperturbative remainder at depth $z = 30$ g/cm^2 with $\alpha = 0$ Deg.

VII.3 GCR BOUNDARY CONDITION

The remainder contribution for the case of a GCR boundary condition can be found by calculating

$$\begin{aligned}\phi^{NP}(\mathbf{x},\mathbf{\Omega},E) &= \sum_{m\geq j}^{N}\sum_{k=j+1}^{m-1}\int_{E}^{\infty} dE_0 \frac{P_j(E_2^*)\tilde{S}_j(E_2^*)}{P_j(E)\tilde{S}_j(E)}\sigma_{jk}(\tilde{E}_{jk}^*) \\ &\quad \cdot\frac{C_{km}(\rho^*)}{2g'_{km}(\rho^*)}\left[W_{km}^{(1)}-W_{km}^{(2)}\right]F_m(E_0)[\bar{g}_{jm}(x-x')-\bar{g}_{jm}^0(x-x') \\ &\quad - \bar{g}_{jm}^1(x-x')-\bar{g}_{jm}^2(x-x')]/\bar{g}_{jm}^2(x-x'). \qquad (270)\end{aligned}$$

Figures 101-103 show the nonperturbative remainder for an oxygen (^{16}O) fragment associated with the iron (^{56}Fe) component of the GCR as a function of inclination angle γ (Deg) and energy E (MeV/amu), at depths $z = 5, 10$, and 30 g/cm^2 of aluminum (^{27}Al) respectively. In this case, there is axial symmetry about the z-direction and therefore, the results are presented only for the case in which $\alpha = 0$ (Deg). As seen in the figures to follow, at the smaller depths, the contribution for the remainder is small and grows rapidly at approximately 60 degrees when the depth into the material has reached the point where the ions are starting to be produced. Close to the boundary, there are no fragments produced, which is why there is an increase in fragments at a relatively shallow depth.

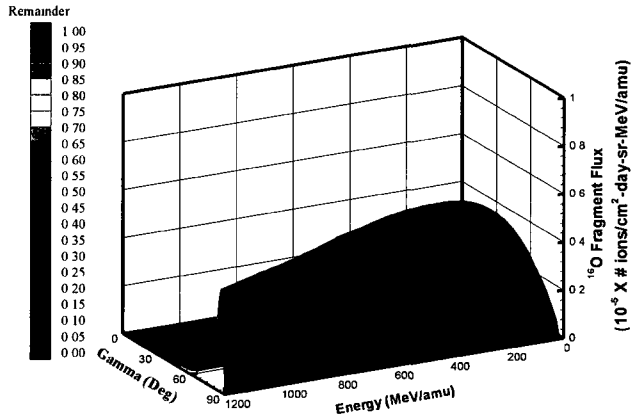

FIGURE 101: The nonperturbative remainder at depth $z = 5$ g/cm^2 with $\alpha = 0$ Deg.

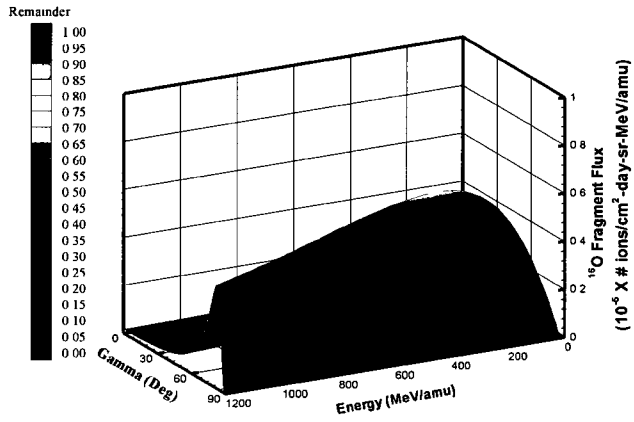

FIGURE 102: The nonperturbative remainder at depth $z = 10$ g/cm^2 with $\alpha = 0$ Deg.

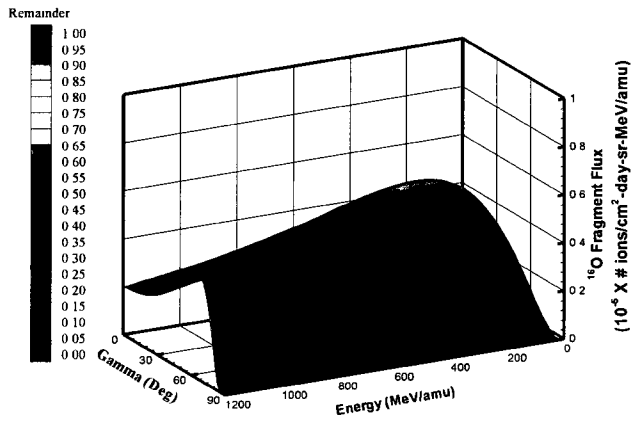

FIGURE 103: The nonperturbative remainder at depth $z = 30$ g/cm^2 with $\alpha = 0$ Deg.

VII.4 TOTAL FLUX

Now that the terms of the Neumann series have been approximated, the overall flux obtained from this formalism can now be compared with previous data. Before making these comparisons, the overall flux will be demonstrated for the ion beam spectra boundary conditions. For illustrative purposes, an aluminum (^{27}Al) half-space is considered as the target material of interest.

In the figure shown below, figure 104, the total flux given by an 1000 MeV/amu iron (^{56}Fe) projectile and an oxygen (^{16}O) fragment is illustrated as a function of inclination angle, γ (Deg), and energy (MeV/amu) at depths $z = 2, 5, 10$ and 15 g/cm^2 of aluminum (^{27}Al). Further, $s_E = 30$ (MeV/amu), $s_{\mathbf{\Omega}} = 45$ (Deg), $s_x = 1$, and $\mathbf{\Omega}_0 = (\frac{1}{\sqrt{2}}, 0, \frac{1}{\sqrt{2}})$.

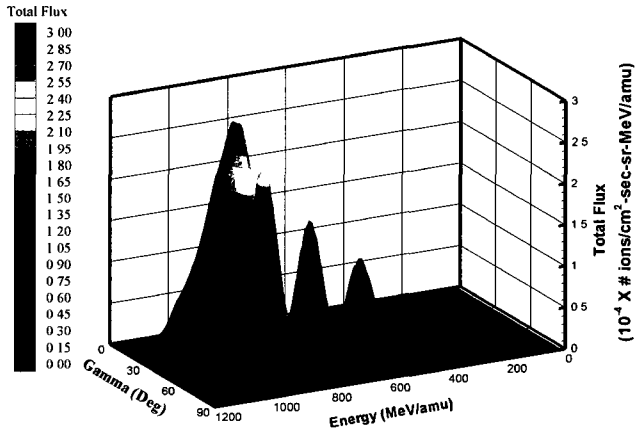

FIGURE 104: The total flux at depths (from left to right) $z = 2, 5, 10$, and 15 g/cm^2 from left to right with $\alpha = 0$ Deg.

The same general trend that was demonstrated in the previous chapters is again seen here. In addition, a similar illustration can be presented for the Galactic Cosmic Ray boundary condition.

In the next chapter, the Neumann series solution obtained in this dissertation will be compared with the results presented in [20], in which a one dimensional Green's function solution was obtained. In order to do this, the solution obtained here will have to be reduced to one dimension. This is done by finding the angle

independent integral Green's functions. The purpose of this comparison is to show that the solution reduces properly to its one dimensional equivalent by eliminating the angular dependance. Recall that the zero order angle independent integral Green's function was already derived and was given by (144). In the next chapter, the first and second order angle independent integral Green's functions will be derived.

CHAPTER VIII

RESULTS

In this chapter, the angle independent first and second order Green's functions will be discussed. This is done in an effort to compare and analyze the differences between the previously defined one dimensional Neumann series solution [20] and the Neumann series solution derived in this dissertation. In addition to the comparisons between the two solutions, comparisons will also be made between HZETRN and the derived results.

VIII.1 INTEGRAL FLUX

First, consideration is given to the angular independent first order Green's function

$$\begin{aligned}\tilde{G}^1_{jm}(\mathbf{x},\mathbf{x}_0,\mathbf{\Omega}_0,E,E_0) &= \int_{4\pi} G^1_{jm}(\mathbf{x},\mathbf{x}_0,\mathbf{\Omega},\mathbf{\Omega}_0,E,E_0)d\mathbf{\Omega} \\ &\approx \frac{H[-\mathbf{\Omega}_0\cdot\mathbf{n}(\mathbf{x}')]}{2\pi s_x^2 K_x|\partial_u\mathbf{x}'\times\partial_v\mathbf{x}'|}\exp\left\{-\frac{(u'-u_0)^2+(v'-v_0)^2}{2s_x^2}\right\} \\ &\quad\cdot G^1_{jm}(\rho,\rho',E,E_0), \end{aligned} \tag{271}$$

where $G^1_{jm}(\rho,\rho',E,E_0)$ is the one dimensional first order Green's function [20].

Similarly, the angular dependent second order Green's function is given by

$$\begin{aligned}\tilde{G}^2_{jm}(\mathbf{x},\mathbf{x}_0,\mathbf{\Omega}_0,E,E_0) &= \int_{4\pi} G^2_{jm}(\mathbf{x},\mathbf{x}_0,\mathbf{\Omega},\mathbf{\Omega}_0,E,E_0)d\mathbf{\Omega} \\ &\approx \sum_{k=j+1}^{m-1}\frac{\tilde{B}_{jk}(\rho_2^*)C_{km}(\rho^*)}{2g'_{km}(\rho^*)}\left[W^{(1)}_{km}(\rho,\rho')\right. \\ &\quad \left.-W^{(2)}_{km}(\rho,\rho')\right] \end{aligned} \tag{272}$$

where

$$\tilde{B}_{jk}(\rho_2^*) = \frac{P_j(E_2^*)\tilde{S}_j(E_2^*)}{P_j(E)\tilde{S}_j(E)} \frac{H[-\mathbf{\Omega}\cdot\mathbf{n}(\mathbf{x}')]}{2\pi s_x^2 K_x |\partial_u \mathbf{x}' \times \partial_v \mathbf{x}'|} \cdot\sigma_{jk}(\tilde{E}_{jk}) \exp\left\{-\frac{(u'-u_0)^2+(v'-v_0)^2}{2s_x^2}\right\}. \quad (273)$$

Notice that for equation (272), the reference to the one dimensional Green's function given in [20] was not made. This is because in this dissertation, when approximating the $W_{km}^{(p)}(\rho,\rho')$ functions, a different choice was made for $\hat{\rho}_p$ (see equation (251)) than was made in [20].

VIII.2 VERIFICATION VERSUS 1D GRNTRN

First, the ion beam spectra boundary condition will be used to verify that the fluxes given by the angular independent Green's functions (equations (144), (271), and (272)) match up with that of the one dimensional Green's functions [20]. For illustrative purposes, a one layer slab of aluminum (^{27}Al) will be considered as the target and the projectile will be a 1000 MeV/amu iron (^{56}Fe) ion beam. The following figures will compare the flux obtained from the primary ion as well as the flux obtained by the fragment oxygen (^{16}O). Furthermore, the energy spread is $s_E = 30$ MeV/amu, and the flux will be calculated at various depths.

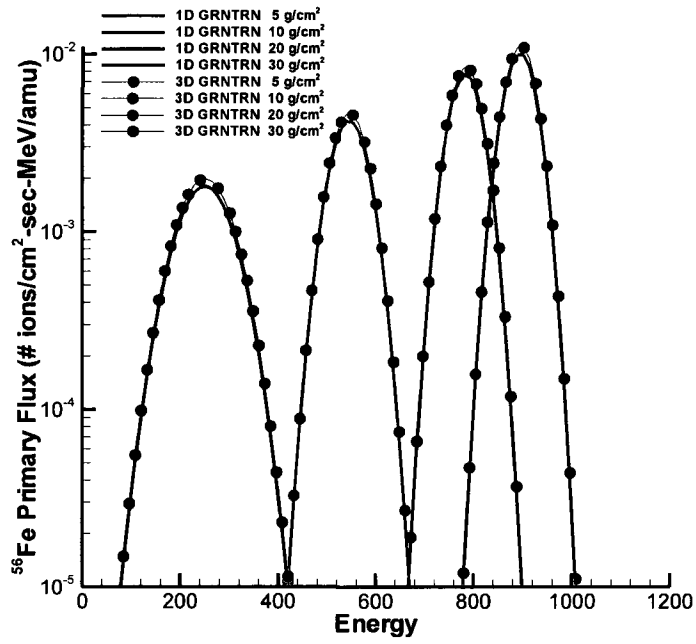

FIGURE 105: A comparison of the ^{56}Fe primary flux at various depths.

Figure 105 shows that there is good agreement between the two solutions for the primary flux calculation. Notice that the flux is shown in a logarithmic scale. To demonstrate a quantitative comparison between the two solutions, the l^2-norm will be used to calculate the differences in the data. Table 3 demonstrates just how close these two solutions are.

TABLE 3: l^2-norm comparing 1D GRNTRN vs 3D GRNTRN for primary flux.

	5 g/cm^2	10 g/cm^2	20 g/cm^2	30 g/cm^2
iron	1.6489007×10^{-4}	2.2277041×10^{-5}	2.194533×10^{-6}	1.5961247×10^{-7}

Next, a comparison will be made for the fragment flux calculations at several depths.

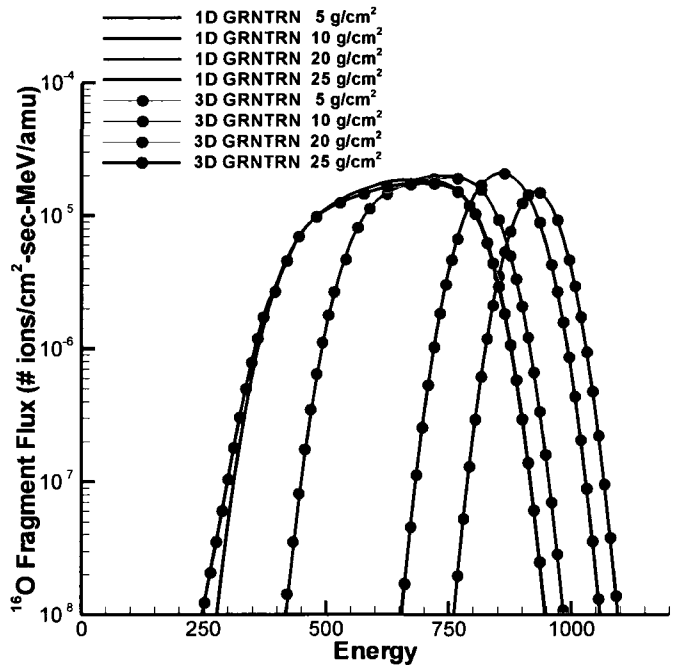

FIGURE 106: A comparison of the ^{16}O fragment flux at various depths.

Figure 106 demonstrates the qualitative agreement between the two solutions for the fragment flux calculations. Again, the flux is shown in a logarithmic scale.

In the table below, the l^2-norm was used to calculate the quantitative difference between the fragment flux calculations for lithium, oxygen, and calcium. The table shows that the models are in agreement.

TABLE 4: l^2-norm comparing 1D GRNTRN vs 3D GRNTRN for fragment flux.

	5 g/cm^2	10 g/cm^2	20 g/cm^2	30 g/cm^2
lithium	1.0629901×10^{-8}	1.4877704×10^{-9}	1.5662893×10^{-9}	5.4232649×10^{-9}
oxygen	1.065787×10^{-9}	3.7752908×10^{-12}	6.4175311×10^{-11}	1.4720335×10^{-10}
calcium	2.0247795×10^{-11}	1.3034324×10^{-11}	3.9358183×10^{-12}	7.5967184×10^{-12}

These figures indicate that for heavy ions, there is no significant difference between

the two solutions when the angular dispersion is taken out. Where the solutions will differ is for light ions and lower energies, where there is a broader angular distribution.

VIII.3 VERIFICATION VERSUS HZETRN

In addition to demonstrating the agreement between the results for an ion beam spectra, the Galactic Cosmic Ray boundary condition can also be explored. For this, the comparison will be made between the NASA Langley developed deterministic code HZETRN and the Neumann series solution derived in this dissertation. Recall that one approach that can be used to calculate the flux for an arbitrary boundary condition once the Green's functions are derived is given by equation (107). Also, recall that the terms in the Neumann series with a GCR boundary condition are given by equations (158), (230), (256), and (270). Notice that these equations can be written in terms of the one dimensional Green's functions as follows:

$$\phi_j^0(\mathbf{x},\mathbf{\Omega},E) \approx H[-\mathbf{\Omega}\cdot\mathbf{n}(\mathbf{x}')]\phi_j^0(\rho-\rho',E), \tag{274}$$

where

$$\phi_j^0(\rho-\rho',E) = \delta_{jm}\frac{P_m(\bar{E}_m)}{P_m(E)}\frac{\tilde{S}_m(\bar{E}_m)}{\tilde{S}_m(E)}F_m(\bar{E}_m), \tag{275}$$

$$\phi_j^1(\mathbf{x},\mathbf{\Omega},E) = \int_E^\infty dE' G_{jk}^1(\rho,\rho',E,E')F_k(E'), \tag{276}$$

$$\phi_j^2(\mathbf{x},\mathbf{\Omega},E) = \int_E^\infty dE' G_{jk}^2(\rho,\rho',E,E')F_k(E'), \tag{277}$$

and

$$\phi_j^{NP}(\mathbf{x},\mathbf{\Omega},E) = \int_E^\infty dE' G_{jk}^{NP}(\rho,\rho',E,E')F_k(E'). \tag{278}$$

Using these representations, the iron (^{56}Fe) primary flux as well as the total fragment flux generated by lithium (^{7}Li), oxygen (^{16}O), and calcium (^{40}Ca) associated with the (^{56}Fe) component of the GCR for the 1977 GCR solar minimum will be calculated and compared with the results obtained from HZETRN 2005. These comparisons are shown in figures 107-110. **Note that the magnitudes of the flux calculations are not the same in the figures to follow.**

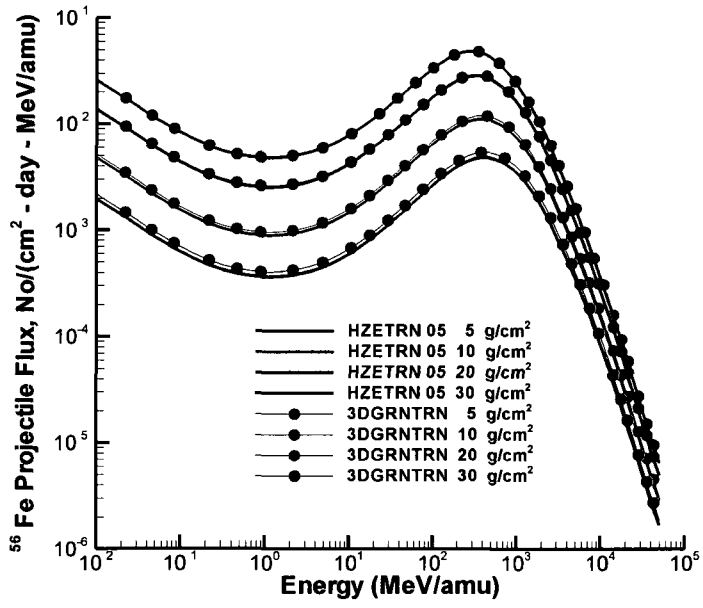

FIGURE 107: A comparison of the ^{56}Fe projectile flux at various depths for the 1977 GCR solar minimum.

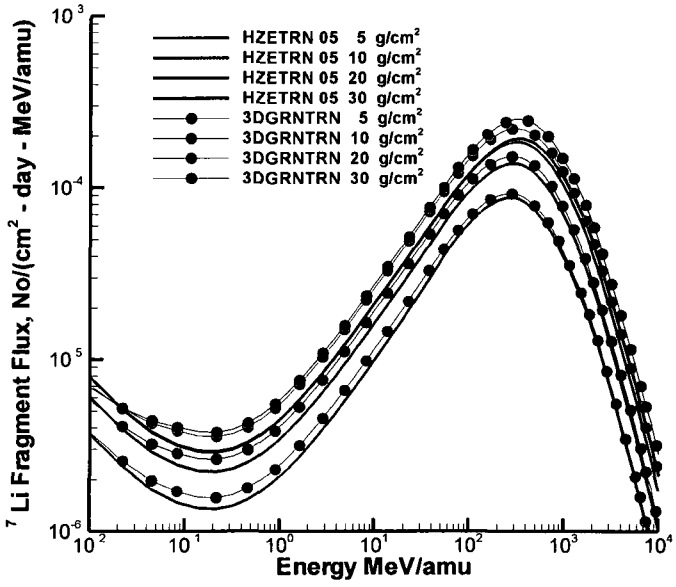

FIGURE 108: A comparison of the ^{7}Li fragment flux at various depths for the 1977 GCR solar minimum.

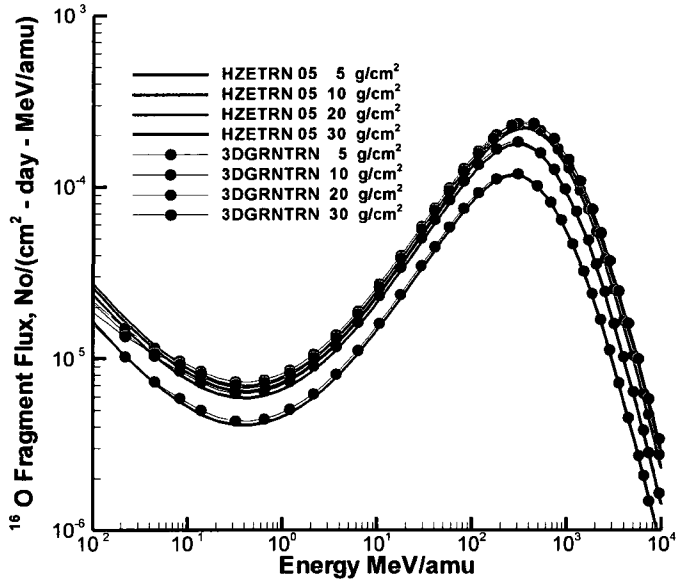

FIGURE 109: A comparison of the ^{16}O fragment flux at various depths for the 1977 GCR solar minimum.

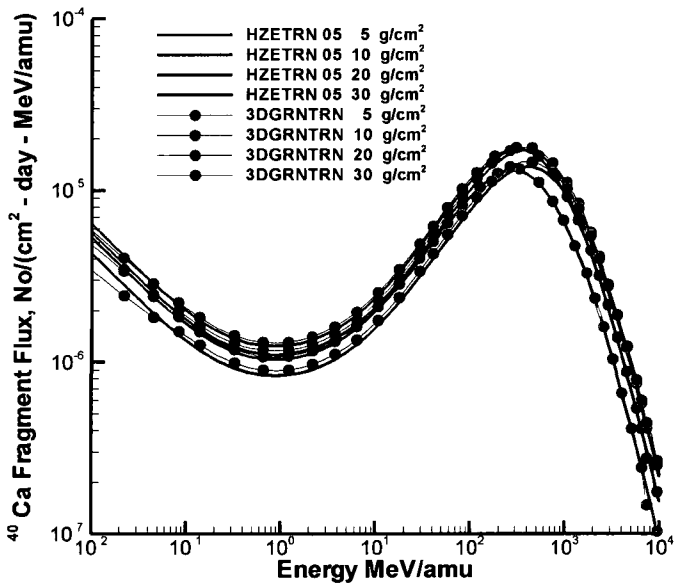

FIGURE 110: A comparison of the ^{40}Ca fragment flux at various depths for the 1977 GCR solar minimum.

These figures qualitatively demonstrate that the three dimensional Green's function solution agrees with the results obtained by the deterministic code HZETRN. A quantitative comparison will now be done for the results that were illustrated above.

TABLE 5: l^2-norm comparing HZETRN and 3D GRNTRN for the iron primary flux.

	5 g/cm^2	10 g/cm^2	20 g/cm^2	30 g/cm^2
iron	4.4981702×10^{-3}	5.3995536×10^{-3}	4.4955090×10^{-3}	3.0280869×10^{-3}

TABLE 6: l^2-norm comparing HZETRN vs 3D GRNTRN for fragment flux.

	5 g/cm^2	10 g/cm^2	20 g/cm^2	30 g/cm^2
lithium	3.3279117×10^{-5}	8.4324929×10^{-5}	1.9480115×10^{-4}	2.9998765×10^{-4}
oxygen	1.9825919×10^{-5}	3.7266134×10^{-5}	6.7649664×10^{-5}	9.4014074×10^{-5}
calcium	1.4093768×10^{-6}	3.0820522×10^{-6}	4.8339239×10^{-6}	5.6265931×10^{-6}

The figures show, and the tables confirm, that the two models are in agreement. Therefore, it has been demonstrated that the 3D GRNTRN model presented in this dissertation matches with previously tested models for both laboratory as well as space boundary conditions.

However, since the data available for a three dimensional ion beam is not readily available, the best verification analysis that can be done at this point is the comparison that was made between the solution derived in this dissertation and that of the one dimensional equivalent. Also, in terms of the GCR boundary condition, the three dimensional calculations that are given by other transport codes were unavailable at the time of the development of this dissertation. Therefore, the one dimensional data that was used in the comparison with HZETRN is all that can be done at this time.

Overall, what has been demonstrated is that the three dimensional Green's function solution derived in this dissertation when collapsed to one dimension agrees with the one dimensional Green's function solution [20]. Therefore, according to [32], the solution derived is validated with one dimensional laboratory beam data.

CHAPTER IX

CONCLUSIONS

Meeting the challenge of future space programs will require an accurate and efficient method for performing radiation transport calculations to determine and verify shielding requirements. This dissertation presented the formulation of one such code by using a Green's function technique.

First, this dissertation began with the discussion of the model that would be used for the cross section input parameter. In analyzing the energy and angular distributions, which make up the cross section representation, it was found that the approximations were more accurate for heavy ions and for high energies, which was expected.

Following this, the formulation of the problem was presented, in which the Green's function technique was used to solve the Boltzmann equation for the transport of heavy ions. The solution of the Boltzmann equation ultimately led to a Neumann series expansion. This expansion was then approximated term-by-term for the first three terms with the remainder being calculated using a non-perturbative technique. The terms were defined recursively and were given by the Green's functions derived in this dissertation. Each Green's function approximation was determined to be accurate by comparing the corresponding approximation with the result obtained by quadrature.

Throughout the formulation of the series, several environments and simple geometries were introduced to demonstrate the influence of both factors on the magnitude of the incoming radiation. Two environments that were of particular interest were the laboratory and space boundary conditions. Using these environments, the capability of the derived solution to model the transport of both broad and narrow spectra boundary conditions was demonstrated.

The terms were then combined with the non-perturbative remainder to demonstrate the overall flux that was approximated by the Green's function solution. Once the series was completely approximated, comparisons were made between the one dimensional Green's function solution using the straight-ahead approximation and the Green's function solution derived in this dissertation by collapsing the solution to one dimension by computing the integral flux. Once collapsed, the three dimensional Green's function essentially becomes the straight-ahead approximation and thus the

two solutions yielded similar results for the laboratory beam boundary condition. Since the solution was verified with the one dimensional Green's function solution, it was then concluded that the three dimensional solution can also be validated with laboratory beam data as was done with the one dimensional solution in [32].

The comparison was also made for the GCR boundary condition in which the 1977 solar minimum data was used as the incoming broad energy spectra. This data set was chosen because during this time, the GCR fluxes that were measured were higher than the previous solar minimum period in 1965 and subsequently higher than most which followed and represented a broad range of energies. It was also chosen because this data set is often used as a reference for comparisons. Using this boundary condition, the three dimensional Green's function solution was compared with the deterministic HZETRN code developed at NASA Langley. This comparison was also used as another verification to determine the accuracy of the three dimensional Green's function solution.

The work that can be done on this problem is far from over. One thing that can be improved is accuracy of the light ion cross sections that are being used. Before this is accomplished, a simple step to improve the accuracy would be to evaluate the cross section numerically for these few light ions. However, since there is interest in computational efficiency, this is not the optimal solution.

Also, just as was done with the one dimensional Green's function solution, the model should be extended to handle more complicated geometries. Then, more useful biological and engineering calculations can be evaluated, such as dose and dose equivalent. This will then allow this code to aid in the determination and verification of shielding requirements.

In conclusion, the formulation of the three dimensional Green's function technique for the transport of heavy ions in laboratory and space was presented. This accurate and efficient method was used to perform radiation calculations for both laboratory and space measurements and has been indirectly validated with accelerator results.

BIBLIOGRAPHY

[1] D. MacKinnon, J. Baldanze, Footprints: The 12 Men Who Walked on the Moon Reflect on their Flights, their Lives, and the Future, Acropolis Books, Washington, DC, 1989.

[2] J.E. Stevens, A Bumpy Road to Mars, Smithsonian Institution, 2004.

[3] Committee on the Evaluation of Radiation Shielding for Space Exploration, Managing Space Radiation Risk in the New Era of Space Exploration, The National Academies Press, Washington, D.C., 2008.

[4] W.R. Corliss, Space Radiation, US Atomic Energy Commission, Oak Ridge, TN, 1968.

[5] T. Stanev, High Energy Cosmic Rays, Springer, New York, NY, 2004.

[6] L.I. Miroshnichenko, Radiation Hazard in Space, Kluwer Academic Publishers, Boston, MA, 2003.

[7] Aurora Research Institute, The Northern Lights of Our Sky, available: http://wiki.nwtresearch.com/scirep7.ashx, December 2010.

[8] The Wilcox Solar Observatory, Heliospheric Current Sheet, available: http://wso.stanford.edu/gifs/HCS.html, December 2010.

[9] R.H. Thomas, Radiation Transport and Shielding. In Alexander Wu Chao and Maury Tigner (Ed.), Handbook of Accelerator Physics and Engineering (pp. 662-673), World Scientific Publishing Co. Pte. Ltd., NJ, 1999.

[10] N. Mokhov, MARS Home Page, Fermi National Accelerator Laboratory, available: http://www-ap.fnal.gov/MARS/, October 2010.

[11] J.W. Wilson, F.F. Badavi, F.A. Cucinotta, J.L. Shinn, G.D. Badhwar, R. Silberberg, C.H. Tsao, L.W. Townsend, R.K. Tripathi, HZETRN: Description of a Free-Space Ion and Nucleon Transport and Shielding Computer Program, NASA TP-3495, 1995.

[12] J.W. Wilson, L.W. Townsend, S.L. Lamkin, B.D. Ganapol, A Closed Form Solution to HZE Propagation, Radiation Research 122 (1990) 223-228.

[13] J.W. Wilson, S.L. Lamkin, H. Farhat, B.D. Ganapol, L.W. Townsend, A Hierarchy of Transport Approximations for High Energy Heavy (HZE) Ions, NASA TM-4118, 1989.

[14] J.W. Wilson, F.F. Badavi, R.C. Costen, J.L. Shinn, Nonperturbative Methods in HZE Transport, NASA TP-3363, 1993.

[15] J.W. Wilson, L.W. Townsend, W. Schimmerling, G.S. Khandelwal, F. Khan, J.E. Nealy, F.A. Cucinotta, L.C. Simonsen, J.L. Shinn, J.W. Norbury, Transport Methods and Interactions for Space Radiations, NASA RP-1257, 1991.

[16] J.L. Shinn, J.W. Wilson, F.F. Badavi, E.V. Benton, I. Csige, A.L. Frank, E.R. Benton, HZE Beam Transport in Multilayered Materials, Radiation Measurements 23 (1994) 57-64.

[17] J.L. Shinn, J.W. Wilson, W. Schimmerling, M.R. Shavers, J. Miller, E.V. Benton, A.L. Frank, F.F. Badavi, A Green's function method for heavy ion beam transport, Radiat. Environ. Biophys 34 (1995) 155-159.

[18] J.L. Shinn, J.W. Wilson, E.V. Benton, F.F. Badavi, Multilayer Analyses of an Iron Radiation Beam Experiment, NASA TM-4753, 1997.

[19] S.A. Walker, J. Tweed, J.W. Wilson, F.A. Cucinotta, R.K. Tripathi, S. Blattnig, C. Zeitlin, L. Heilbtonn, J. Miller, Validation of the HZETRN code for laboratory exposures with 1 A GeV iron ions in several targets, Adv. Space Res. 35 (2005) 202-207.

[20] J. Tweed, J.W. Wilson, R.K. Tripathi, An improved Green's function for ion beam transport, Advances in Space Research 34 (2004) 1311-1318.

[21] C. Mertens, J.W. Wilson, S.A. Walker, J. Tweed, Coupling of Multiple Coulomb Scattering with Energy Loss and Straggling in HZETRN, Advances in Space Research 40 (2007) 1357-1367.

[22] J. Tweed, S.A. Walker, F.F. Badavi, R.K. Tripathi, J.W. Wilson, C.J. Zeitlin, J. Miller, L.H. Heilbronn, Validation Studies of the GRNTRN Code for Radiation Transport, ICES 2007-01-3118, SAE 37th International Conference on Environmental Systems, Chicago, 2007.

[23] J. Tweed, S.A. Walker, J.W. Wilson, R.K. Tripathi, Recent Progress in the Development of a Multi-Layer Green's Fucntion Code for Ion Beam Transport, STAIF-2008 (Space Technology and Applications Forum), Albuquerque, NM, February 10-14, 2008. AIP Conf. Proc. 969, 993-1000, 2008.

[24] L.W. Townsend,F. Khan, R.K. Tripathi, Optical model analyses of 1.65A GeV argon fragmentation: Cross sections and momentum distributions, Phys. Rev. C 48 (1993) 2912-2919.

[25] R.K. Tripathi, L.W. Townsend, F. Khan, Role of intrinsic width in fragment momentum distributions in heavy ion collisions, Phys. Rev. C 48 (1994) R1775-R1777.

[26] J.W. Wilson, Analysis of the theory of high-energy ion transport, NASA TN D-8381, 1977.

[27] D.S. Anikonov, A.E. Kovtanyuk, I.V. Prokhorov, Transport Equation and Tomography, VSP, Boston, MA, 2002.

[28] J.W. Wilson, R.C. Costen, J.L. Shinn, F.F. Badavi, Green's Function Methods in Heavy Ion Shielding, NASA TP 3311, 1993.

[29] M. G. Payne, Energy Straggling of Heavy Charged Particles in Thick Absorbers, Phys. Rev. 185 (1969) 611-623.

[30] J.W. Wilson, J. Tweed, H. Tai, R.K. Tripathi, A simple model for straggling evaluation, Nucl. Instr. and Meth. in Phys. Res. B 194 (2002) 389-392.

[31] J.W. Wilson, M.R. Shavers,F.F. Badavi, J. Miller, J.L. Shinn, R.C. Costen, Nonperturbative methods in HZE propagation, Raidat. Res 140 (2) (1994) 241-248.

[32] S.A. Walker, The Straggling Green's Function Method for Ion Transport, Ph.D. dissertation, Old Dominion University, 2005.

APPENDIX A

SOME USEFUL IDENTITIES

The function

$$\bar{E}_j = \bar{E}_j(\rho - \rho', E) = R_j^{-1}[R_j(E) + \rho - \rho'] \tag{279}$$

introduced above may be interpreted as the energy on entry, of a j-particle that has residual energy E MeV/amu after penetrating the transport material to a depth of $(\rho - \rho')$ g/cm^2. The corresponding inverse function is clearly given by

$$\hat{E}_j = \hat{E}_j(\rho - \rho', E) = R_j^{-1}[R_j(E) - (\rho - \rho')] \tag{280}$$

and represents the mean energy at depth $(\rho - \rho')$ g/cm^2 of a j-particle that entered the transport material with energy E MeV/amu.

Since $R_j(E) = \int_0^E \frac{dH}{\tilde{S}_j(H)}$ and $R_j(\hat{E}_j) = R_j(E) - (\rho - \rho')$ we see that

$$\partial_E R_j(\hat{E}_j) = \partial_E[R_j(E) - (\rho - \rho')] \rightarrow [S_j(\hat{E}_j)]^{-1}\partial_E \hat{E}_j = [S_j(E_j)]^{-1} \tag{281}$$

that is

$$\partial_E \hat{E}_j(\rho - \rho', E) = \frac{S_j(\hat{E}_j)}{S_j(E_j)} \tag{282}$$

and

$$\partial_E \bar{E}_j(\rho - \rho', E) = \frac{S_j(\bar{E}_j)}{S_j(E_j)} \tag{283}$$

Now recall that, for a monotone differentiable function $f(x)$, we have

$$\delta[f(x) - f(x_0)]|f'(x)| = \delta(x - x_0) \tag{284}$$

then

$$\begin{aligned} \frac{\tilde{S}_j(E_0)}{\tilde{S}_j(E)}\delta(\bar{E}_j - E_0) &= \frac{\tilde{S}_j(\bar{E}_j)}{\tilde{S}_j(E)}\delta(\bar{E}_j - E_0) \\ &= [\frac{\partial}{\partial E}\bar{E}_j(\rho - \rho', E)]\delta[\bar{E}_j(\rho - \rho', E) \\ &\quad -\bar{E}_j\{\rho - \rho', \hat{E}_j(\rho - \rho', E_0)\}] \end{aligned} \tag{285}$$

showing that

$$\frac{\tilde{S}_j(E_0)}{\tilde{S}_j(E)}\delta[(\rho-\rho',E)-E_0]=\delta[E-\hat{E}_j(\rho-\rho',E_0)] \tag{286}$$

APPENDIX B

DERIVATION OF NORMALIZATION CONSTANTS

The normalization constants K_x and $K_{\mathbf{\Omega}}$ are chosen such that

$$\int_{\partial V} d\mathbf{x}_1 \int_{4\pi} d\mathbf{\Omega}_0 \int_E^\infty dE_0 F_j(\mathbf{x}_b, \mathbf{\Omega}, E) = 1, \tag{287}$$

in which case

$$\begin{aligned} 1 &= \int_{\partial V} d\mathbf{x}_1 \int_{4\pi} d\mathbf{\Omega}_0 \int_E^\infty dE_0 \frac{\delta_{jm} H[-\mathbf{\Omega}\cdot\mathbf{n}(\mathbf{x}_b)]}{4\pi s_x^2 s_{\mathbf{\Omega}} s_E K_x K_{\mathbf{\Omega}} |\partial_u \mathbf{x}_b \times \partial_v \mathbf{x}_b|} \\ &\quad \cdot \exp\left\{-\frac{(u_b-u_0)^2+(v_b-v_0)^2}{2s_x^2}\right\} \\ &\quad \cdot \exp\left\{-\frac{(1-\mathbf{\Omega}\cdot\mathbf{\Omega}_0)^2}{2s_{\mathbf{\Omega}}^2}\right\} \exp\left\{-\frac{(E-E_0)^2}{2s_E^2}\right\} \\ &= \int_{\partial V} \frac{\delta_{jm}}{2\pi s_x^2 K_x |\partial_u \mathbf{x}_b \times \partial_v \mathbf{x}_b|} \exp\left\{-\frac{(u_b-u_0)^2+(v_b-v_0)^2}{2s_x^2}\right\} \\ &\quad \cdot \int_{4\pi} d\mathbf{\Omega}_0 \frac{H[-\mathbf{\Omega}\cdot\mathbf{n}(\mathbf{x}_b)]}{\sqrt{2\pi} s_{\mathbf{\Omega}} K_{\mathbf{\Omega}}} \exp\left\{-\frac{(1-\mathbf{\Omega}\cdot\mathbf{\Omega}_0)^2}{2s_{\mathbf{\Omega}}^2}\right\} \\ &\quad \cdot \int_E^\infty dE_0 \frac{1}{\sqrt{2\pi} s_E} \exp\left\{-\frac{(E-E_0)^2}{2s_E^2}\right\}. \end{aligned} \tag{288}$$

It can be seen that the energy integral is equal to 1 and that the directional integral can be written as the integral over the spherical polar coordinates θ and ϕ,

$$\begin{aligned} 1 &= \frac{1}{K_x} \int_{u_s}^{u_f} du_b \frac{1}{\sqrt{2\pi} s_x} \exp\left\{-\frac{(u_b-u_0)^2}{2s_x^2}\right\} \int_{v_s}^{v_f} dv_b \frac{1}{\sqrt{2\pi} s_x} \exp\left\{-\frac{(v_b-v_0)^2}{2s_x^2}\right\} \\ &\quad \cdot \frac{1}{K_{\mathbf{\Omega}}} \int_0^{2\pi} \int_0^{\pi} \frac{1}{\sqrt{2\pi} s_{\mathbf{\Omega}'}} \exp\left\{-\frac{(1-\cos\theta)^2}{2s_{\mathbf{\Omega}}^2}\right\} \sin\theta d\theta d\phi. \end{aligned} \tag{289}$$

Using $u = \frac{1-\cos\theta}{\sqrt{2} s_{\mathbf{\Omega}}}$, the θ integral can be evaluated as $\frac{1}{2}\operatorname{erf}\left(\frac{\sqrt{2}}{s_{\mathbf{\Omega}}}\right)$. Also, the integral over ϕ will yield 2π, so

$$
\begin{aligned}
1 &= \frac{1}{K_x}\left[\int_0^{u_f} du_b \frac{1}{\sqrt{2\pi}s_x}\exp\left\{-\frac{(u_b-u_0)^2}{2s_x^2}\right\}\right. \\
&\quad \left. -\int_0^{u_s} du_b \frac{1}{\sqrt{2\pi}s_x}\exp\left\{-\frac{(u_b-u_0)^2}{2s_x^2}\right\}\right] \\
&\quad \cdot\left[\int_0^{v_f} dv_b \frac{1}{\sqrt{2\pi}s_x}\exp\left\{-\frac{(v_b-v_0)^2}{2s_x^2}\right\}\right. \\
&\quad \left. -\int_0^{v_s} dv_b \frac{1}{\sqrt{2\pi}s_x}\exp\left\{-\frac{(v_b-v_0)^2}{2s_x^2}\right\}\right] \\
&\quad \cdot\frac{1}{K_{\boldsymbol{\Omega}}}\pi\,\mathrm{erf}\left(\frac{\sqrt{2}}{s_{\boldsymbol{\Omega}}}\right).
\end{aligned} \tag{290}
$$

Also, using $t = \dfrac{u_b - u_0}{\sqrt{2}s_x}$,

$$
\begin{aligned}
\int_0^{u_f} du_b \frac{1}{\sqrt{2\pi}s_x}\exp\left\{-\frac{(u_b-u_0)^2}{2s_x^2}\right\} &= \int_0^{t(u_f)} \frac{1}{\sqrt{\pi}}\exp\left\{-t^2\right\} dt \\
&= \frac{1}{2}\,\mathrm{erf}\left(\frac{u_f-u_0}{\sqrt{2}s_x}\right)
\end{aligned} \tag{291}
$$

This same result is used for all four remaining integrals, which gives

$$
\begin{aligned}
1 &= \frac{1}{K_x}\left\{\frac{1}{2}\,\mathrm{erf}\left(\frac{u_f-u_0}{\sqrt{2}s_x}\right) - \frac{1}{2}\,\mathrm{erf}\left(\frac{u_s-u_0}{\sqrt{2}s_x}\right)\right\} \\
&\quad \cdot\left\{\frac{1}{2}\,\mathrm{erf}\left(\frac{v_f-v_0}{\sqrt{2}s_x}\right) - \frac{1}{2}\,\mathrm{erf}\left(\frac{v_s-v_0}{\sqrt{2}s_x}\right)\right\} \\
&\quad \cdot\frac{1}{K_{\boldsymbol{\Omega}}}\pi\,\mathrm{erf}\left(\frac{\sqrt{2}}{s_{\boldsymbol{\Omega}}}\right).
\end{aligned} \tag{292}
$$

Therefore, the normalization constants are given by

$$
\begin{aligned}
K_x &= \frac{1}{4}\left[\mathrm{erf}\left(\frac{u_f-u_0}{\sqrt{2}s_x}\right) - \mathrm{erf}\left(\frac{u_s-u_0}{\sqrt{2}s_x}\right)\right] \\
&\quad \cdot\left[\mathrm{erf}\left(\frac{v_f-v_0}{\sqrt{2}s_x}\right) - \mathrm{erf}\left(\frac{v_s-v_0}{\sqrt{2}s_x}\right)\right],
\end{aligned} \tag{293}
$$

$$
K_{\boldsymbol{\Omega}} = \pi\cdot\mathrm{erf}\left(\frac{\sqrt{2}}{s_{\boldsymbol{\Omega}}}\right). \tag{294}
$$

VITA

Candice Rockell Gerstner
Department of Computational and Applied Mathematics
Old Dominion University
Norfolk, VA 23529

Education

Ph.D. Computational and Applied Mathematics, May 2011
Old Dominion University, Norfolk, VA.
M.S. Computational and Applied Mathematics, December 2008
Old Dominion University, Norfolk, VA.
B.S. Mathematics, May 2006
St. John Fisher College, Rochester, NY.

Publications in Referred Journals

Rockell, C., Tweed, J., Blattnig, S.R. and Mertens, C.J., "Recent Developments in Three Dimensional Radiation Transport using the Green's Function Technique", Nuclear Science and Engineering, Submitted (2010)

Conference Papers

Rockell, C., Tweed, J. "On the Development of a Deterministic Three-Dimensional Radiation Transport Code", NASA Conference Publication: MODSIM World, October 2010.

Rockell, C., Tweed, J., Blattnig, S.R. and Mertens, C.J., "An Introduction to Three Dimensional Radiation Transport using the Green's Function Technique", VSGC Conference Proceedings, April 2010.

Rockell, C., Tweed, J., "A Green's Function Technique for Radiation Transport in 3D", VSGC Conference Proceedings, April 2009.

Typeset using LaTeX.